Structural Investigation of Quaternary Copper Oxides with Low Dimensional Magnetic Properties

Von der Fakultät für Bergbau, Hüttenwesen und Geowissenschaften
der Rheinisch-Westfälischen Technischen Hochschule Aachen

zur Erlangung des akademischen Grades eines
Doktors der Naturwissenschaften

genehmigte Dissertation
vorgelegt von Dipl.-Phys.

Karine Sparta
aus Grasse (Frankreich)

Berichter:
Univ.-Prof. Dr. rer. nat. G. Roth
Univ.-Prof. Dr. rer. nat. G. Heger
Univ.-Prof. C. Lecomte

Tag der mündliche Prüfung: 11. Juli 2003

Contents

Abstract

The aim of this work is the study of ternary and quaternary copper oxides with low-dimensional magnetic properties, mainly by means of powder and single crystal X-ray diffraction and single crystal neutron diffraction experiments, at low and high temperatures.
Two of these compounds, $SrCu_2(BO_3)_2$ and $BaCuSi_2O_6$, are two-dimensional spin gap systems, in which the Cu^{2+} ions ($S = \frac{1}{2}$) are antiferromagnetically coupled to each other, but they don't exhibit a three-dimensional long range ordered magnetic structure. The magnetic properties in such compounds are very often extremely sensitive to even small structural distortions. An accurate knowledge of the Cu - Cu and Cu - O bond lengths and Cu - O - Cu angles is therefore important to get a better understanding of their magnetic properties.

The structure of $SrCu_2(BO_3)_2$ ($I\bar{4}2m$) consists of corrugated $Cu_2(BO_3)_2$ - layers, magnetically separated along the c axis by Sr - layers. Within the $Cu_2(BO_3)_2$ - layers, the Cu^{2+} ions form a triangular array, topologically equivalent to the Shastry-Sutherland model. This configuration leads to spin frustration and the formation of a spin gap at low temperatures. $SrCu_2(BO_3)_2$ is the first known compound that realizes an exact dimer ground state.
The temperature evolution of the structure of $SrCu_2(BO_3)_2$ has been determined between 9 K and 590 K. We have found a second order structural phase transition at $T_s = 395$ K, from the low temperature space group $I\bar{4}2m$ to the high temperature space group $I4/mmm$. The main structural change upon the phase transition concerns the $Cu_2(BO_3)_2$ - layers: The Cu, B and O atoms are distributed above and below the plane $z = \frac{1}{4}$ in the low temperature phase; they all lie in the same plane above T_s, and the Cu - Cu interlayer distances become equivalent. A change in the behaviour of the magnetic susceptibility was also observed around T_s, thus pointing to the existence of weak but significant magnetic interactions between the $Cu_2(BO_3)_2$ - layers, which had previously been neglected in the literature.
We observed that the thermal ellipsoids of the atoms within the $Cu_2(BO_3)_2$ - layers are very elongated in the c direction at room temperature, and the anisotropy of the thermal ellipsoids increases strongly with the temperature until T_s. We thus performed single crystal neutron diffraction experiments in order to search for anharmonicities in

the material.
Since $SrCu_2(BO_3)_2$ lies close to the critical point between the dimer and Néel states in the magnetic phase diagram of the Shastry-Sutherland model, studies of doping effects on the magnetic properties of this compound were performed, in order to change the values of the magnetic Cu - Cu interactions and to possibly come close to the critical point. We studied $(Sr,M)Cu_2(BO_3)_2$, with $M = Ca, Ba$. However, the substitution of Sr by Ca or Ba seems to have very few impacts on the structure and properties of the material, so that a qualitative change of the magnetic ground state does not occur.

$BaCuSi_2O_6$ is one of the very few silicates containing isolated Si_4O_{12} - rings. It contains $Cu_2Si_4O_{12}$ - layers, magnetically separated along the c axis by Ba - layers. Within the $Cu_2Si_4O_{12}$ - layers, the Cu^{2+} ions build dimers parallel to c, separated from each other by SiO_4 tetrahedra. Like $SrCu_2(BO_3)_2$, $BaCuSi_2O_6$ shows at low temperatures no sign of magnetic ordering and possesses a spin gap. The structure has been studied at low as well as high temperatures, by means of single crystal X-ray diffraction methods.
We discovered at room temperature the presence of superstructure reflections, and therefore redetermined more accurately the structure of $BaCuSi_2O_6$ in the space group $I4_1/acd$. The Raman spectroscopy results published earlier, aimed at a better understanding of the structure of amorphous SiO_2, need to be reinterpreted taking into account this superstructure.
A structural phase transition occurs in this material at 610 K, from the room temperature space group $I4_1/acd$ to the high temperature space group $I4/mmm$. This phase transition leads to a high temperature unit cell volume four times smaller than the room temperature one, but its order is not clear yet.

During the synthesis of $(Sr,Ba)Cu_2(BO_3)_2$ under $LiBO_3$ - flux, we discovered the first quaternary compound in the Li - Cu - B - O system: $Li_6CuB_4O_{10}$. It crystallizes in the space group $P\bar{1}$. Its structure consists of CuO_4 distorted squares, surrounded by two B_2O_5 groups and two LiO_4 tetrahedra.
Because of the large nearest neighbour distance between the Cu^{2+} ions, $Li_6CuB_4O_{10}$ is expected to present very weak magnetic interactions.
Between room temperature and the melting point, $Li_6CuB_4O_{10}$ undergoes three structural phase transitions which are still to be investigated by means of single crystal X-ray diffraction.

Chapter 1

Introduction

1.1 Motivation

Electronically low dimensional compounds show a wide diversity of collective quantum states, like magnetic and superconducting phases, that are not yet well understood. In particular, the relevant interactions in a system are often not clear: which phenomena are specific to the material and which ones have a more general nature?
The study of systems with a strong electronic correlation, like spin gap phases, can deliver important informations to describe the involved mechanisms in order to get a better understanding of superconductivity: Spin gap phases as well as superconducting materials undergo a magnetic phase transition, from a high temperature paramagnetic phase to a low temperature diamagnetic phase.
Collective quantum states result in many physical properties, and different techniques of investigation are needed to get an understanding of these states. A good knowledge of the crystallographic structure is one of the prerequisites to achieve that goal.
In this section are presented some examples taken from the literature; sections 1.2 and 1.3 describe briefly some systems which have been investigated within this study, as they were known before the beginning of this work – chapters 3 and 4 will be dedicated to these compounds.

1.1.1 $SrCu_2O_3$ and $Sr_2Cu_3O_5$

These two compounds belong to the homologous series of the high pressure orthorhombic phases $Sr_{n-1}Cu_{n+1}O_{2n}$ ($n = 3, 5, 7\ldots$), in which the $Cu_{n+1}O_{2n}$- and Sr-layers alternate along the c axis [1].
$SrCu_2O_3$ (i.e. $Sr_2Cu_4O_6$, $n = 3$) has an orthorhombic unit cell of space group $Cmmm$ (No. 65 in the International Tables for Crystallography [2]), with the cell parameters $a = 3.934\,\text{Å}$, $b = 11.573\,\text{Å}$ and $c = 3.495\,\text{Å}$. $Sr_2Cu_3O_5$ (i.e. $Sr_4Cu_6O_{10}$, $n = 5$) crystallizes in the same space group, with $a = 3.931\,\text{Å}$, $b = 19.408\,\text{Å}$ and $c = 3.460\,\text{Å}$. In this

compound series, the lattice parameter b is roughly $n \times a$.
$SrCuO_2$ (space group No. 63 $Cmcm$, $a = 3.565\,\text{Å}$, $b = 16.326\,\text{Å}$, $c = 3.921\,\text{Å}$ [3]) corresponds to the limit case $n = \infty$. Pressure induces in $SrCuO_2$ a structural phase transition, to a tetragonal infinite-layer structure ($P4/mmm$ (No. 123), $a = 3.926\,\text{Å}$, $c = 3.432\,\text{Å}$).
$SrCu_2O_3$ and $Sr_2Cu_3O_5$ are both one-dimensional compounds, respectively containing two-leg and three-leg $S = \frac{1}{2}$ ladders with antiferromagnetic Cu - O - Cu bonds (Fig. 1.1). The magnetic interactions between Cu^{2+} ions arise from superexchange via the oxygen atoms of the ladders.

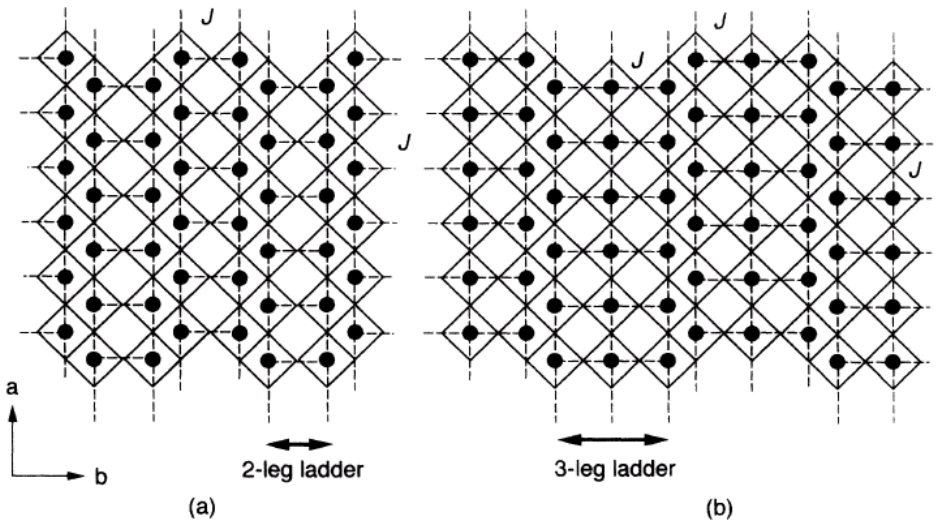

Figure 1.1: Schematic drawings of the Cu_2O_3 - sheet of $SrCu_2O_3$ (a) and the Cu_3O_5 - sheet of $Sr_2Cu_3O_5$ (b). The filled circles are the Cu^{2+} ions, and the O^{2-} ions at the corners of the squares are not represented (Fig. 1 from [4]). In [4], the magnetic interactions J between the Cu^{2+} ions are considered as having the same magnitude along a and b, although the Cu - Cu distances are not the same in both directions [5].

As can be seen in figure 1.2, $SrCu_2O_3$ presents a large spin gap ($\Delta = 420\,\text{K}$) whereas $Sr_2Cu_3O_5$ is gapless [4], according to Rice's prediction that the spin gap in $Sr_{n-1}Cu_{n+1}O_{2n}$ is $\Delta = 0$ for n odd [6].

It is very surprising to see that inspite of the big interest arised around these compounds, no reliable and accurate structural data are available. To our knowledge, the only structural investigations were performed by means of electron diffraction [1].
We have performed single crystal X-ray diffraction experiments on $SrCu_2O_3$ in the temperature range from 100 K up to room temperature. The results won't be discussed here but in [5].

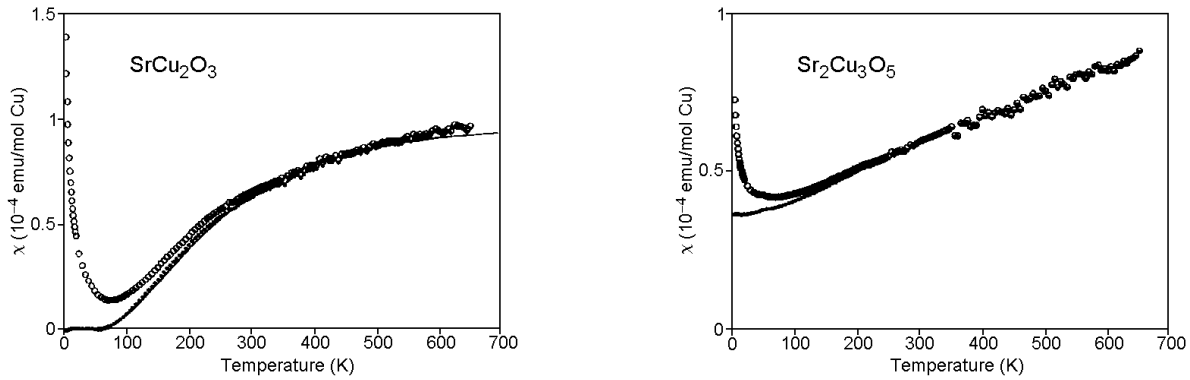

Figure 1.2: Left: Magnetic susceptibility χ of $SrCu_2O_3$ (Fig. 2 from [4]). Right: Magnetic susceptibility of $Sr_2Cu_3O_5$ (Fig. 3 from [4]). The open circles are experimental raw data. The smaller closed circles represent the data after substraction of the Curie component.

1.1.2 $CuGeO_3$

The copper germanate $CuGeO_3$ crystallizes in the orthorhombic space group *Pbmm* (No. 51) at room temperature, with $a = 4.801\,(1)$ Å, $b = 8.469\,(2)$ Å, $c = 2.9431\,(4)$ Å. It contains Heisenberg antiferromagnetic Cu - O - Cu ribbons parallel to the c axis, with copper in a square-planar coordination of oxygen atoms. The Cu^{2+} ions in the chains are coupled by superexchange via the O^{2-} anions. The chains are magnetically isolated from each other by GeO_4 tetrahedra (Fig. 1.3). All the Cu^{2+} ions in the structure occupy equivalent positions.

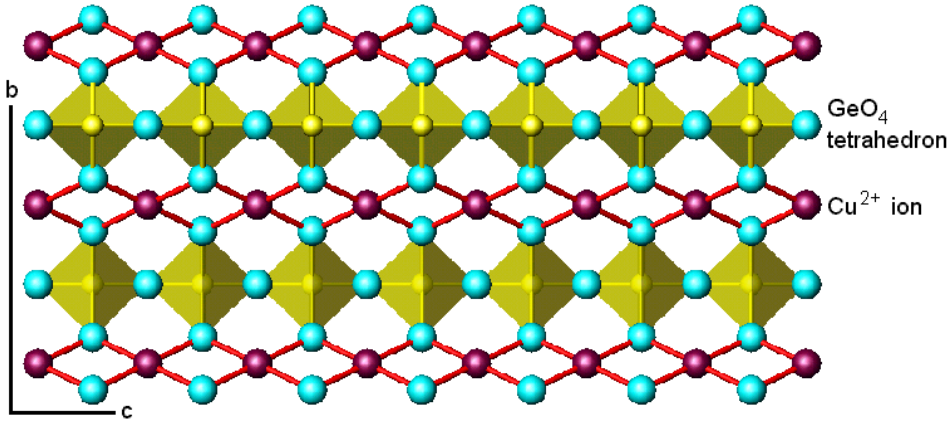

Figure 1.3: The Cu - O - Cu chains in $CuGeO_3$ parallel to the c axis.

Figure 1.4 shows the magnetic susceptibility of $CuGeO_3$ under the magnetic field $H = 1\,T$, pointing to the existence of a magnetic phase transition at $T_{sp} = 14\,K$ [7].

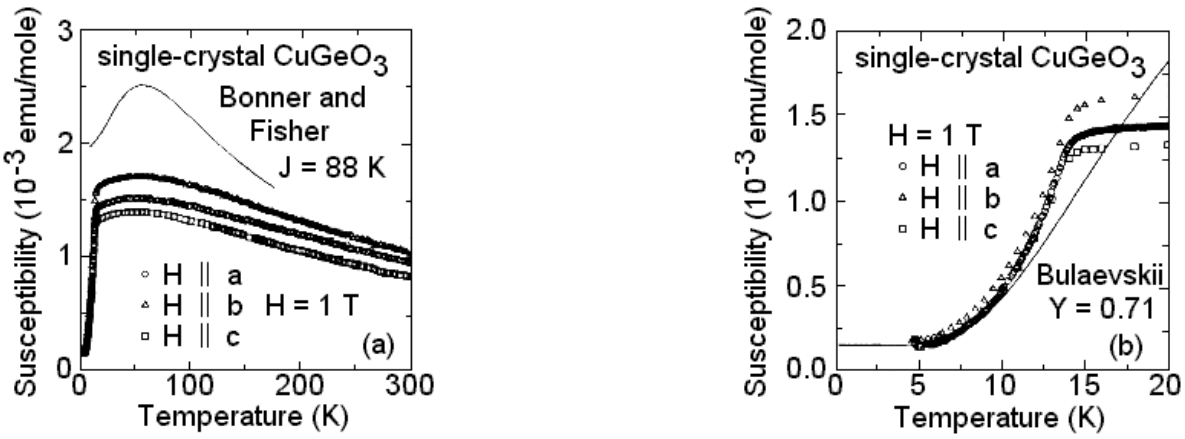

Figure 1.4: Magnetic susceptibility χ of a $CuGeO_3$ single-crystal, measured under $H = 1\,T$ (Fig. 1 from [7]).

In the case where this para-dia magnetic phase transition is driven by antiferromagnetic interactions leading to a pairing of spins with opposite directions, the material exhibits a spin-Peierls transition. A spin-Peierls compound can be defined as a spin system that undergoes structural distortions due to magnetic quantum fluctuations.

In the past, only a few organic one-dimensional compounds, such as $TTFCuS_4C_4(CF_3)_4$ and [MEM-$(TCNQ)_2$], were known to present a spin-Peierls phase transition [8, 9]. It was found in organic spin-Peierls systems that the phase boundaries follow a universal phase diagram [10].

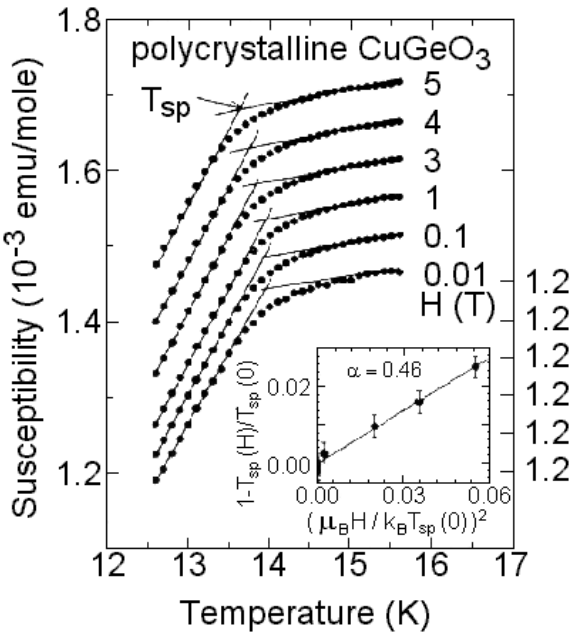

Figure 1.5: Magnetic susceptibility of polycrystalline $CuGeO_3$ close to T_{sp}, measured for $0.01 < H < 5\,T$ (Fig. 2 from [7]).

Magnetic susceptibility measurements were performed on polycrystalline $CuGeO_3$ close to the phase transition for magnetic fields between 0.01 T and 5 T (Fig. 1.5) [7]. The fit of the field dependence of the temperature of the phase transition, $T_{sp}(H)$, shows that the phase boundary between the uniform and the spin-Peierls states in $CuGeO_3$ agrees well with the phase diagram in [10], confirming the fact that $CuGeO_3$ is indeed a spin-Peierls material [7].

$CuGeO_3$ was the first inorganic spin-Peierls compound to be discovered [7]. At 14 K, the crystal undergoes a second order structural phase transition [11], from the room temperature space group *Pbmm* to the space group *Bbcm* (No. 64): the chains dimerize, with two different positions for the Cu^{2+} ions, and a spin gap appears.

1.1.3 α'-NaV_2O_5

The sodium vanadate α'-NaV_2O_5 belongs to the vanadium sodium oxybronzes family $Na_xV_2O_5$ [12]. It crystallizes at room temperature in the orthorhombic space group *Pmmn* (No. 59, $a = 11.316\,(4)$ Å, $b = 3.611\,(1)$ Å, $c = 4.797\,(2)$ Å) [13].
The vanadium and oxygen atoms form distorted tetragonal pyramids, leading to double chains of VO_5 edge-sharing pyramids, parallel to the b axis. These chains are arranged in sheets orthogonal to the c axis, separated by layers of Na atoms (Fig. 1.6). The room temperature structure contains only one symmetry inequivalent position for the $V^{4.5+}$ ions.

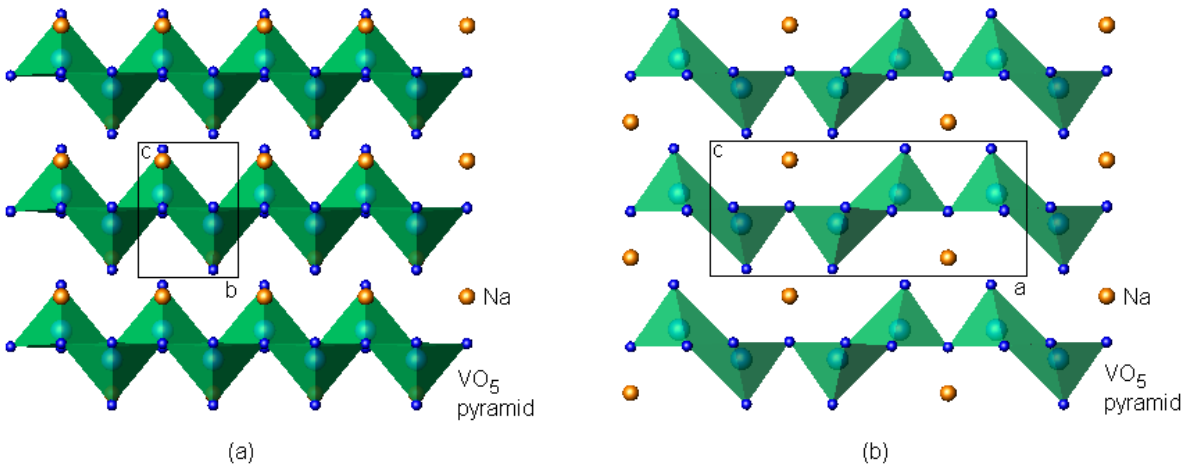

Figure 1.6: Structure of α'-NaV_2O_5 at room temperature. (a): V_2O_5 chains along the b axis; (b): The layer structure of V_2O_5 double chains.

This one-dimensional material was first thought to present an ordinary spin-Peierls phase transition at the critical temperature $T_c = 34\,K$ [14]. Figure 1.7 shows the magnetic susceptibility of α'-NaV_2O_5 as a function of temperature.

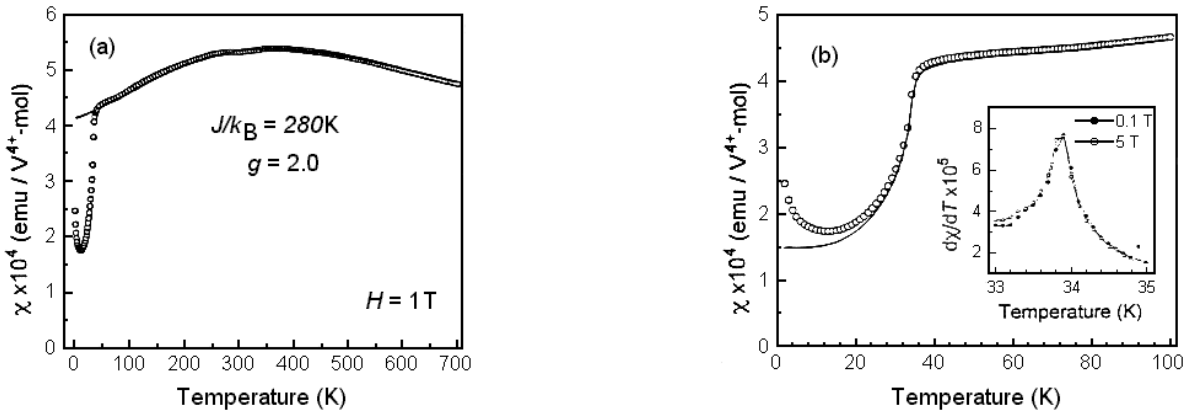

Figure 1.7: Magnetic susceptibility χ of α'-NaV_2O_5 (Fig. 2 from [14]). (a) At 1 T, from 2 K up to 700 K. (b) Between 2 K and 100 K, the insert shows $\frac{d\chi}{dT}$.

It was found by means of X-ray and neutron scattering experiments that, with decreasing temperature, superlattice reflections at $\mathbf{q} = (\frac{1}{2}, \frac{1}{2}, \frac{1}{4})$ appear in α'-NaV_2O_5 at 34 K [15], while a spin gap $\Delta \simeq 100\,K$ opens [16].
Below T_c, the $S = \frac{1}{2}$ antiferromagnetic Heisenberg chains are dimerized, just as in the case of the spin-Peierls transition in $CuGeO_3$. However, specific heat and thermal expansion measurements have shown that the dimerized state results from a two-step phase transition [17], so that the spin-Peierls transition in α'-NaV_2O_5 is not a conventional one.

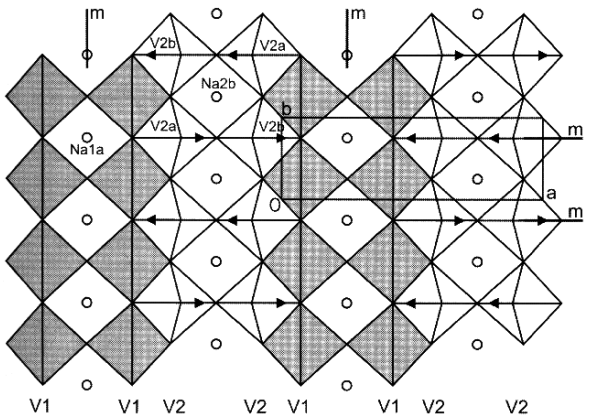

Figure 1.8: Structure of α'-NaV_2O_5 at 15 K along the c axis (Fig. 1 from [18]). The gray (V1) and white (V2) polyedra represent the two independent VO_5 pyramid chains in the $Pmm2$ average structure.

At T= 15 K, the lattice parameters for the average structure are $a = 11.294\,(3)$ Å, $b = 3.604\,(1)$ Å, and $c = 4.755\,(2)$ Å [18]. The analysis of the superstructure reflections

at $(\frac{1}{2}, \frac{1}{2}, \frac{1}{4})$ led to an acentric modulated structure $Fmm2$ with a $(2a \times 2b \times 4c)$ supercell. The superspace approach was used to determine the commensurate modulations, giving the superspace group $Pmm2\,(\frac{1}{2}, \frac{1}{2}, q_3)\,0ss$, with $q_3 = \frac{1}{4}$.
Below T_c, there are thus two independent V_2O_5 chains (Fig. 1.8, 1.9), one being modulated (V2 atoms, zigzag arrangement of V^{4+} and V^{5+} ions) and the other one not (V1 atoms, mixed valence state $V^{4.5+}$).

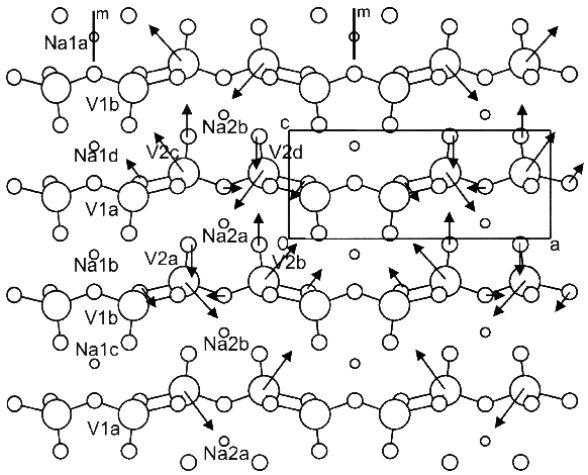

Figure 1.9: Structure of α'-NaV_2O_5 at 15 K with the b axis horizontal (Fig. 2 from [18]). V atoms are represented by large circles, Na atoms by small circles, and O atoms by intermediate circles.

1.2 $SrCu_2(BO_3)_2$

At room temperature, the strontium copper orthoborate crystallizes in the tetragonal space group $I\bar{4}2m$ (No. 121), with $a = 8.995\,(1)$ Å and $c = 6.649\,(1)$ Å [19]. It contains $Cu_2(BO_3)_2{}^{2-}$ - layers orthogonal to the c axis, separated by Sr^{2+} - layers (Fig. 1.10).

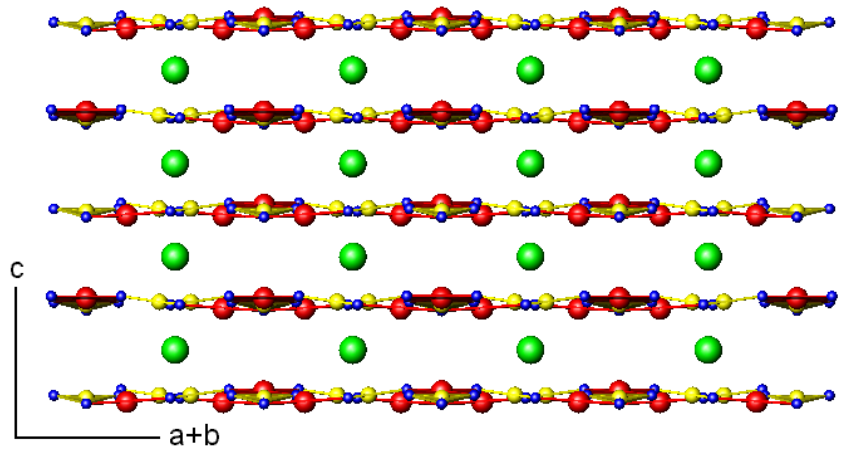

Figure 1.10: Room temperature structure of $SrCu_2(BO_3)_2$ [19].

$SrCu_2(BO_3)_2$ is a two-dimensional spin dimer system realizing the exact dimer ground state [20]. Within the $Cu_2(BO_3)_2$-layers, the Cu^{2+} ions ($S = \frac{1}{2}$) form a net of dimers that are orthogonally coupled to each other.
The intradimer coupling is J and the interdimer coupling J' (Fig. 1.11), they are both antiferromagnetic. This configuration leads to spin frustration and to the formation of a spin gap $\Delta = 30\,\mathrm{K}$ at low temperatures.
A more detailled description of the magnetic properties of $SrCu_2(BO_3)_2$ will be given in section 3.2, page 32.

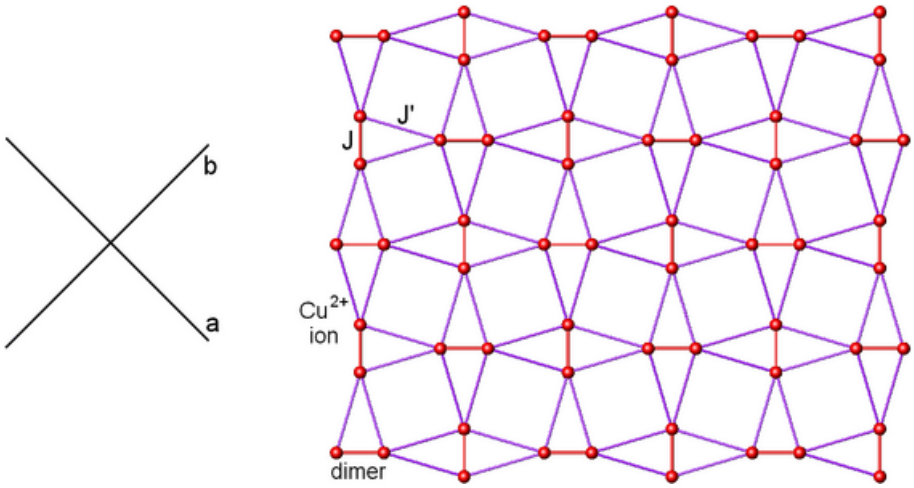

Figure 1.11: Magnetic interactions between the Cu^{2+} ions in the $Cu_2(BO_3)_2$-sheets.

1.3 $BaCuSi_2O_6$

$BaCuSi_2O_6$ crystallizes (in first approximation) in the space group $I\bar{4}m2$ (No. 119), with cell parameters $a = 7.042\,(3)$ Å and $c = 11.133\,(3)$ Å [21]. Its structure consists of $Cu_2Si_4O_{12}{}^{4-}$-layers orthogonal to the c axis, separated by $Ba_2{}^{4+}$-layers (Fig. 1.12).

Just as in the case of $Cu_2(BO_3)_2$, $BaCuSi_2O_6$ is a two-dimensional spin dimer compound with a singlet ground state [22]. The Cu^{2+} ions in the $Cu_2Si_4O_{12}$-layers form quasi-isolated dimers parallel to the c axis. These dimers are arranged in a square lattice within the layers (Fig. 1.13).
The interlayer magnetic coupling along c is very weak. At low temperatures, a spin gap $\Delta \simeq 32\,\mathrm{K}$ opens.
The magnetic properties of $BaCuSi_2O_6$ will be discussed in section 4.3, page 75.

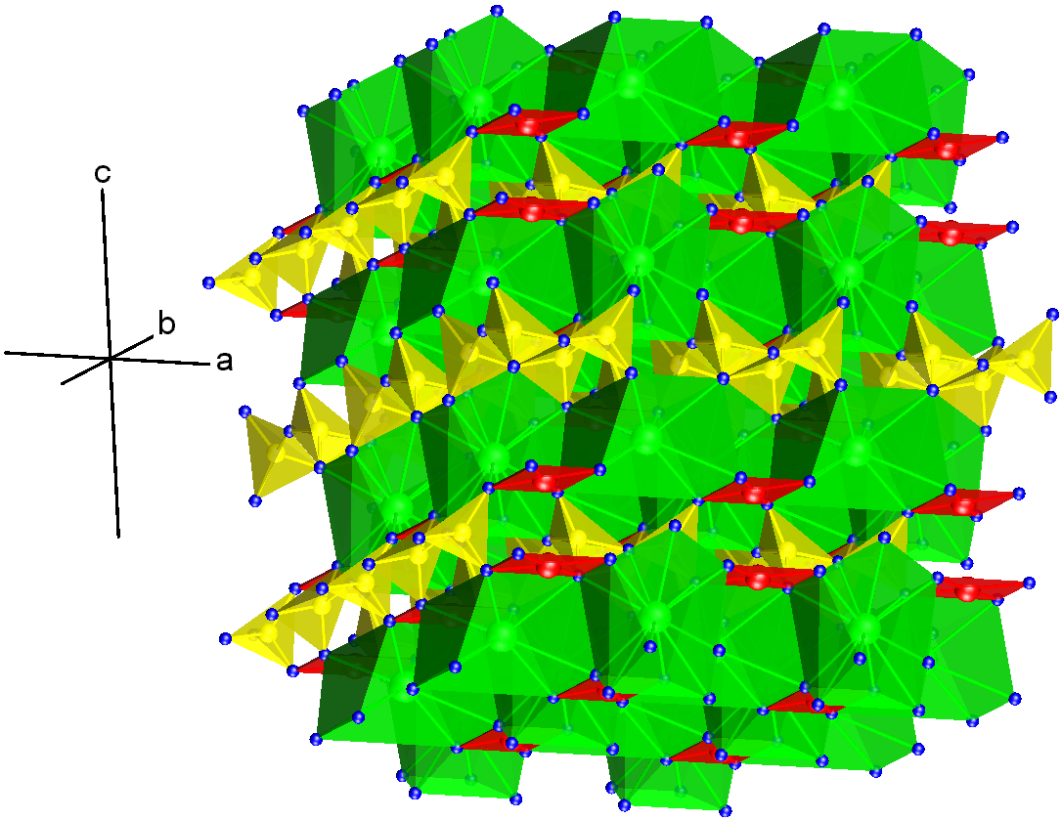

Figure 1.12: Room temperature structure of $BaCuSi_2O_6$ [21], composed of SiO_4 tetrahedra, CuO_4 squares, and Ba atoms represented in the other polyedra.

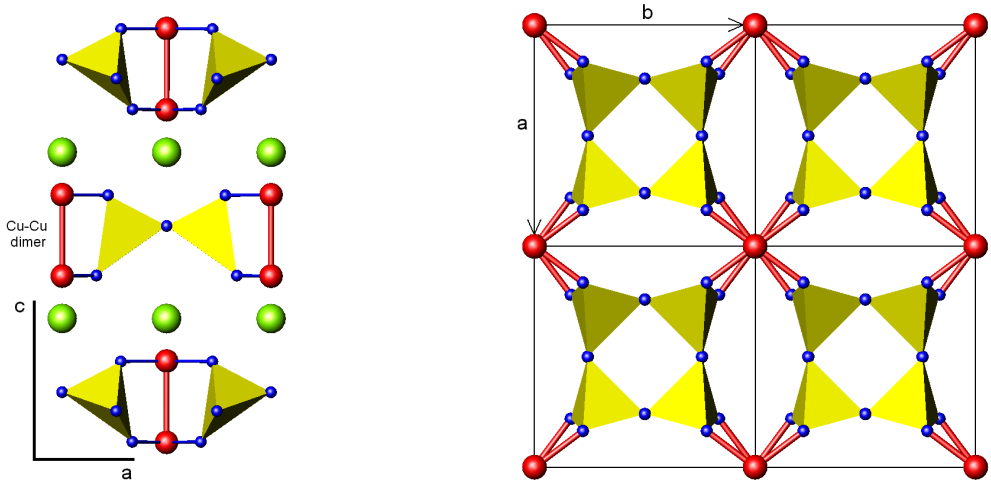

Figure 1.13: Left: The Cu - Cu dimers along the c axis. Right: The arrangement of the dimers within the (**a**, **b**) layers.

Chapter 2

Crystal growth

2.1 $SrCu_2(BO_3)_2$

2.1.1 Synthesis of powder samples

All the powder samples of $SrCu_2(BO_3)_2$ were prepared by a solid state reaction at 900 °C. At the peritectic melting point 970 °C, $SrCu_2(BO_3)_2$ melts incongruently in air.

In [23], $SrCO_3$, CuO and B_2O_3 were mixed and used as starting materials. The mixture was heated under oxygen flow during one week at 900 °C, with some intermediate grindings. This resulted in the formation of a dark blue powder, which was then isostatically pressed in the form of rods and sintered at 850 °C for one day in flowing oxygen.

For the synthesis of our powder samples, we used $SrCO_3$, CuO and B_2O_3 as starting materials, in the necessary amounts to obtain the right stoichiometry. They were mixed homogeneously and put into a platinum crucible, which was placed in a Heraeus KM170 furnace. The samples were heated in air at 900 °C for four weeks, with several intermediate grindings. However, the resulting powder contained some CuO and small amounts of other impurity phases.

Separately, Dr. G. Redhammer prepared a series of pure $SrCu_2(BO_3)_2$ powder samples, from a mixture of $SrCO_3$, CuO_2 and B_2O_3 in the desired stoichiometry by applying a standard high temperature ceramic sintering technique. We used them for the study of the cell parameters temperature dependence.
The mixture of the reagents (2 g) was carefully ground under acetone to a fine homogenous black powder, pressed to discs, put into an open platinum crucible and heated to 800 °C at a rate of about 100 ° per hour. The temperature was held for 24 hours at 800 °C, then the samples, which turned to dark blue, was removed from the furnace and the sample was reground. After this, it was again pressed to discs, loaded to the furnace and heated to 900 °C for a total of 27 days with 5 interrupts to grind the sample. The

final sample was deep blue and except for a minor amount of CuO (tenorite; about 3 % of weight as determined from Rietveld refinements), the X-ray powder pattern indicated a single phase product.

2.1.2 $(Sr,M)Cu_2(BO_3)_2$, M = Ca, Ba

The synthesis of powder samples of Ba- and Ca-substituted strontium copper borate, namely $Sr_xBa_{1-x}Cu_2(BO_3)_2$ and $Sr_xCa_{1-x}Cu_2(BO_3)_2$, was carried out in the same way as for the pure compound.
$SrCO_3$, $BaCO_3$ or $CaCO_3$, CuO and B_2O_3 were used as starting materials. The mixtures in platin crucibles stayed during four weeks at 900 °C in air. We observed that for $x < 0.7$, the melting temperature of $Sr_xM_{1-x}Cu_2(BO_3)_2$ was lower than 900 °C.
The resulting powders were not single-phase, but we could determine the stoichiometry of the interesting phases by comparing the cell parameters with those of single crystals of doped strontium copper borate. The compositions of the powders thus determined were very close to the ones we intended to obtain, at least for the samples with $x > 0.7$. They are summarized in table 2.1.

$Sr_xBa_{1-x}Cu_2(BO_3)_2$	x	0.95	0.90	0.85	0.80	0.65	0.55
$Sr_xCa_{1-x}Cu_2(BO_3)_2$	x	0.90	0.80	0.70			

Table 2.1: Compositions of the $Sr_xA_{1-x}Cu_2(BO_3)_2$ powder samples.

2.1.3 Single crystal growth of $SrCu_2(BO_3)_2$

Most of the single crystals of $SrCu_2(BO_3)_2$ used in this study were grown from a $LiBO_3$ - flux method, by the team of Prof. Yukata Ueda [1] in Tokyo. The following is a summary of [23].
A solvent disk composed of a powder mixture of $LiBO_3$ and $SrCu_2(BO_3)_2$ in a weight ratio of 1 : 3 was prepared and placed between two vertical rods of $SrCu_2(BO_3)_2$ in a mirror furnace, with four halogen lamps used as heating sources. The solvent disk was molten by increasing the power of the lamps. A floating zone between the upper and the lower rods was then immediately created, by moving downwards the upper rod. Under oxygen atmosphere, both rods were rotated in opposite directions, in order to assure the homogeneity of the liquid zone.
Figure 2.1 shows the single crystals of $SrCu_2(BO_3)_2$, grown by Prof. Y. Ueda, that were studied by means of neutron diffraction, at the Laboratoire Léon Brillouin [2] (LLB) in Saclay, France.

[1] Institute for Solid State Physics, Tokyo, Japan
[2] Laboratoire commun CEA - CNRS

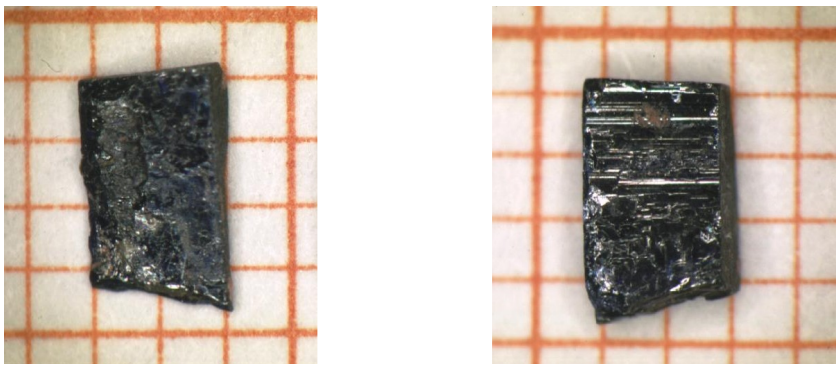

Figure 2.1: Single crystals for the neutron diffraction studies.

2.2 $BaCuSi_2O_6$

$BaCuSi_2O_6$ (or $Ba_2Cu_2[Si_4O_{12}]$) was first synthesized as a by-product during an attempt to grow superconductors in the Tl - Ba - Ca - Cu - O system [21]. The authors of the paper have later grown the material with a mirror furnace, but they didn't publish the growth procedure.
$BaCuSi_2O_6$ was also accidentaly produced by another, independent team during the synthesis of $YBa_2Cu_3O_{7-x}$ with PbO and Na_2O_2 in the molar proportion 1:2:1 [24]. The mixture was pressed and sealed under vacuum in a quartz tube. The sample was heated during one day at 600 °C, then for four hours at 900 °C and quenched in air. At 900 °, the sample reacted with the walls of the quartz tube and violet $BaCuSi_2O_6$ was mainly grown.
The crystals we used for single crystal X-ray diffraction experiments were grown by the team of Prof. K. Uchinokura[3].

2.3 $Li_6CuB_4O_{10}$

The lithium copper borate $Li_6CuB_4O_{10}$ was incidentally produced by Dr. Günther Redhammer while attempting to synthesise Ba - doped $SrCu_2(BO_3)_2$ under $LiBO_3$ - flux. This is a light blue material, showing a strong pleochroism when observed with polarized light. We have found no reference to this material in the crystallographic data file. $Li_6CuB_4O_{10}$ is hence the first known quaternary compound in the Li - Cu - B - O system. Among the compounds produced while trying to synthetize Ba - doped $SrCu_2(BO_3)_2$, we also found a light blue material, looking very much like $Li_6CuB_4O_{10}$ although it showed no anisotropy under polarized light, but it turned out to be a glass phase.

[3]Department of Advanced Materials Science, Tokyo, Japan

$Li_6CuB_4O_{10}$ powder and single crystal samples were grown from a solid state reaction. It was synthesised from reagent grade chemicals Li_2CO_3, CuO_2 and B_2O_3, mixed in the exact stoichiometry. About 1 g of the finely powdered starting material was pressed into a pellet, put into an open platinum crucible, slowly heated to 680 °C in a resistance furnace and kept there for 290 hours. A temperature of 680 °C is close to the eutectic temperature for $2\,Li_2O \cdot B_2O_3$ in the system Li_2O - B_2O_3 (Fig. 2.2). During reaction, the dark grey starting material turned into a deep blue reaction product, consisting of large and partly idiomorphic crystals of the title compound at the outer rims of the pellet and somewhat smaller crystals of the same material within the inner parts of the pellet. No significant additional phases where found in the reaction product.
DSC measurements showed that the material melts incongruently in air at 780 °C.

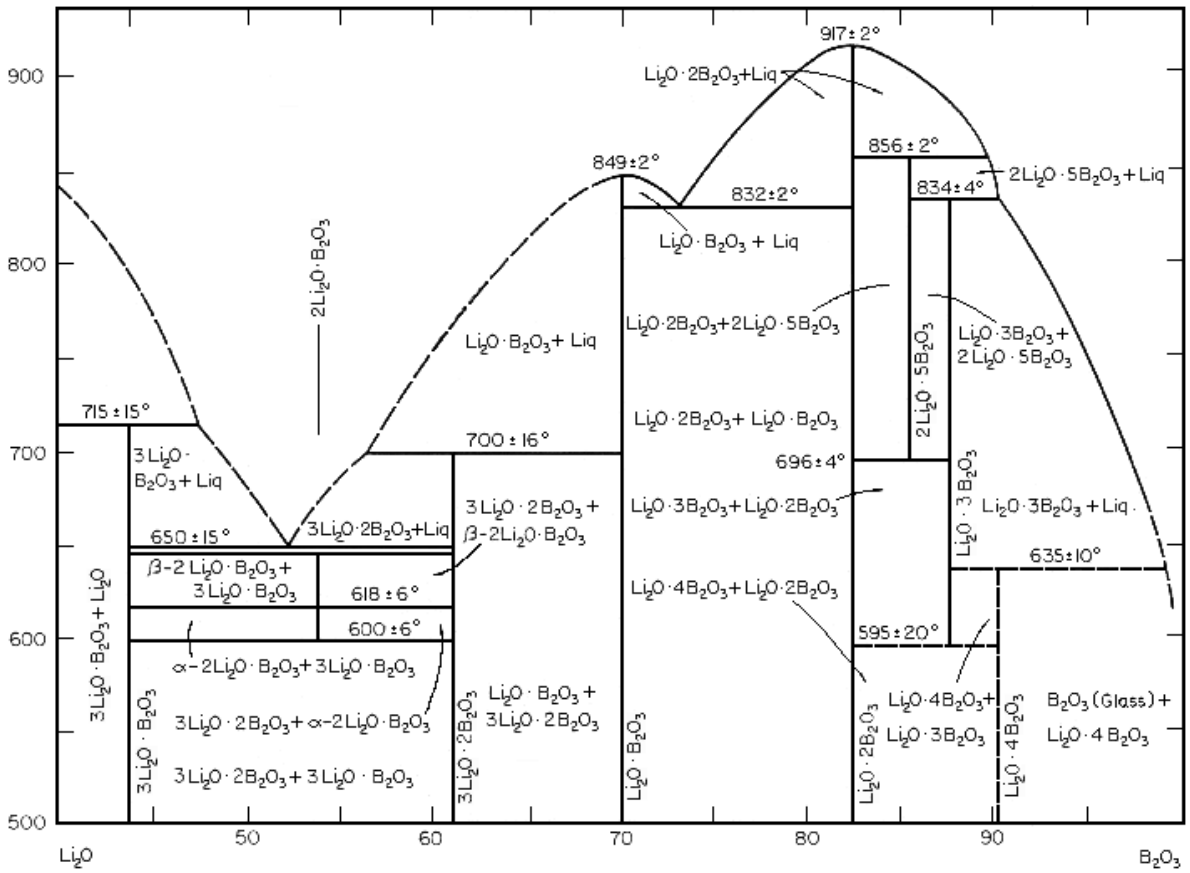

Figure 2.2: Phase diagram for the Li_2O - B_2O_3 system (Fig. 180 from [25]).

Chapter 3

$SrCu_2(BO_3)_2$

3.1 Room temperature structure

3.1.1 $SrCu_2(BO_3)_2$ from the literature

The first determination of the room temperature structure of $SrCu_2(BO_3)_2$ was reported by R. W. Smith and D. A. Kezler in 1991 [19]. The compound crystallizes in the non-centrosymmetric tetragonal space group $I\bar{4}2m$ (No. 121, $Z = 4$, $a = 8.995\,(1)$ Å, $c = 6.649\,(1)$ Å). Tables 3.1 and 3.2 show the structural parameters published in [19].

Atom	Multiplicity	x	y	z	Site symmetry
Sr	4	0	$\frac{1}{2}$	0	222
Cu	8	0.11412 (1)	0.11412 (1)	0.2783 (2)	..m
B	8	0.2953 (4)	0.2953 (4)	0.243 (1)	..m
O1	8	0.4004 (4)	0.4004 (4)	0.212 (1)	..m
O2	16	0.3276 (3)	0.1456 (3)	0.254 (1)	1

Table 3.1: Room temperature structure of $SrCu_2(BO_3)_2$: atomic coordinates [19]. The numbers in brackets indicate the error bars on the last digits.

Atom	U_{11} (Å^2)	U_{22} (Å^2)	U_{33} (Å^2)	U_{12} (Å^2)	U_{13} (Å^2)	U_{23} (Å^2)
Sr	0.0108 (3)	0.0107 (3)	0.0054 (2)	0	0	0
Cu	0.0081 (2)	0.0081 (2)	0.0191 (4)	-0.0001 (2)	0.0004 (2)	0.0004 (2)
B	0.008 (1)	0.008 (1)	0.012 (2)	-0.000 (1)	-0.001 (1)	-0.001 (1)
O1	0.009 (1)	0.009 (1)	0.040 (4)	-0.000 (1)	-0.007 (1)	-0.007 (1)
O2	0.009 (1)	0.008 (1)	0.018 (1)	0.001 (1)	0.001 (1)	0.002 (1)

Table 3.2: Room temperature structure of $SrCu_2(BO_3)_2$: thermal displacement parameters (from [19]).

The stucture is formed by Sr^{2+} - and $Cu_2(BO_3)_2{}^{2-}$ -layers alternating along the c axis. The environment of the strontium atom is a distorted cube of O2 atoms (Fig. 3.1). The Sr - O2a distance is 2.607 (7) Å and the Sr - O2b distance 2.640 (8) Å. They are slightly different because of the absence of an inversion center.

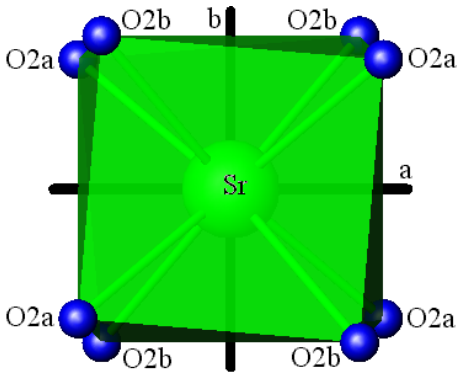

Figure 3.1: Coordination of the Sr atoms: projection onto the (**a**, **b**) plane. The O2a and O2b atoms are symmetry equivalent.

In the $Cu_2(BO_3)_2$ - layers, the copper atoms are surrounded by four oxygen atoms, forming dimers of distorted planar CuO_4 squares. These dimers are orthogonally linked to each other by rigid triangular planar (BO_3) groups to build $Cu_2(BO_3)_2$ plaquettes (Fig. 3.2, 3.3). A closer look shows that the plaquettes are bent, so that the $Cu_2(BO_3)_2$ - layers are corrugated.

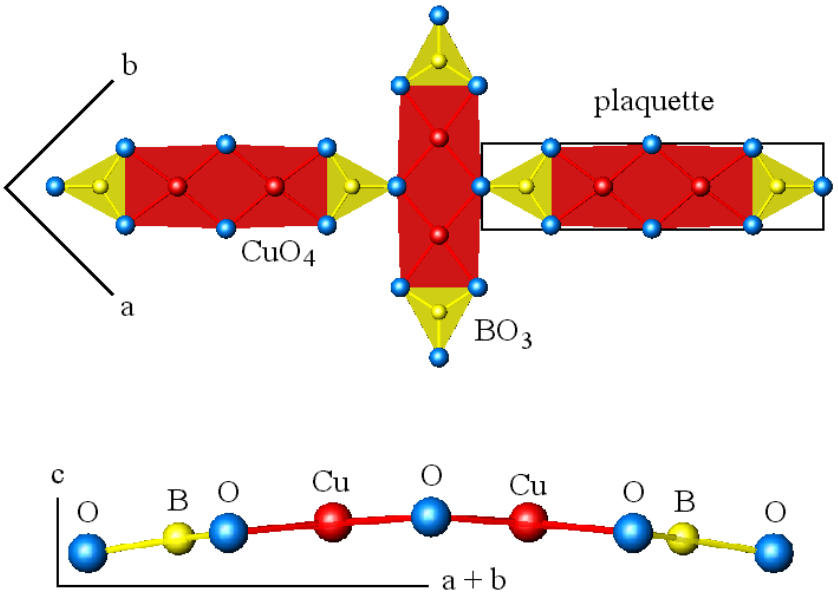

Figure 3.2: Top: $Cu_2(BO_3)_2$ plaquettes linked along the [110] direction. Bottom: One plaquette, seen with the c axis vertical.

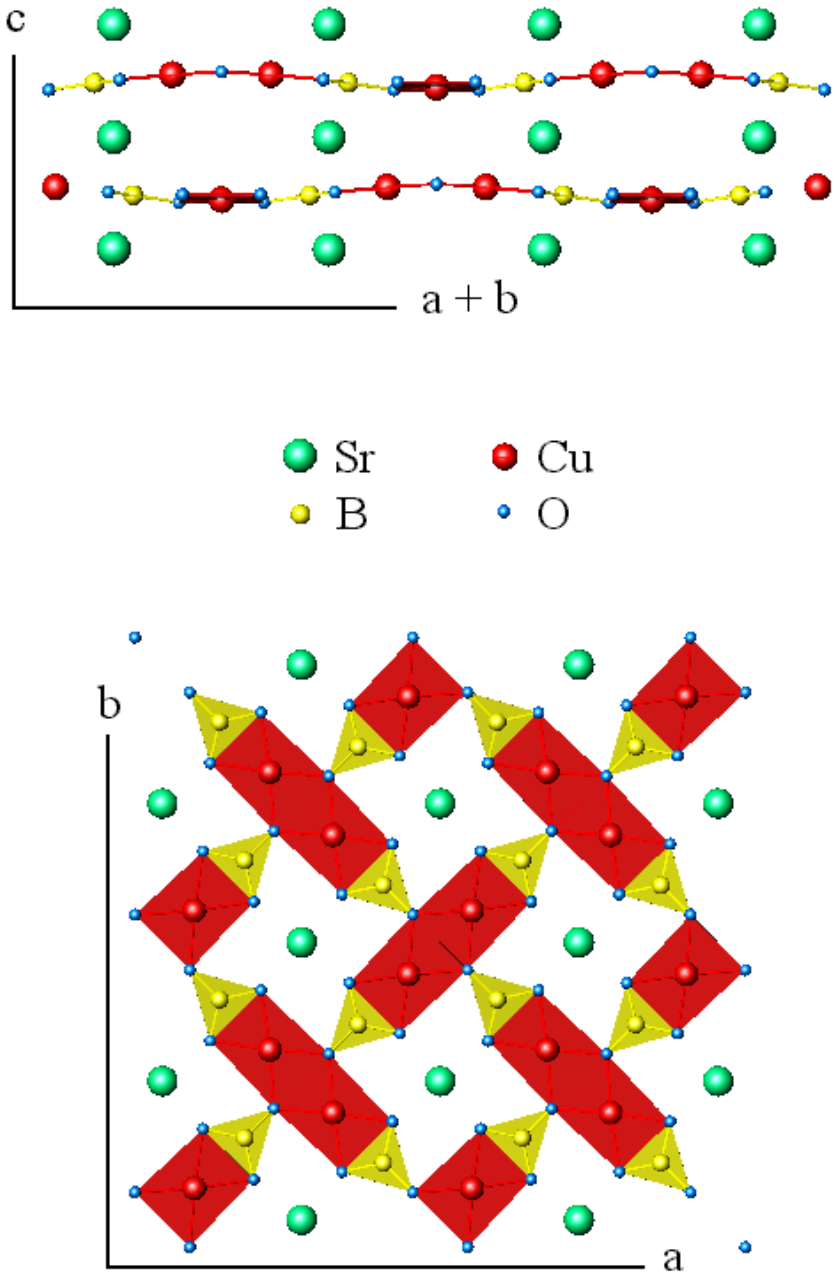

Figure 3.3: Top: projection of the $Cu_2(BO_3)_2$ plaquettes in the $(\mathbf{a}+\mathbf{b}, \mathbf{c})$ plane. Bottom: Projection of a $Cu_2(BO_3)_2$ - layer in the $(\mathbf{a}, \mathbf{b})$ plane; the Sr atoms are out of the plane.

At first sight, the strong deformation of the planar CuO_4 squares is surprising (Fig. 3.4). This deformation is not primarily due to the Cu - O bond lengths: the Cu - O1 distance is 1.928 (4) Å and the Cu - O2 distance 1.948 (4) Å. More predicative are the O - Cu - O angles, and the O - O distances giving the lengths of the distorted square. They are listed in table 3.3. In particular, the O2a - O2b distance, 2.32 (1) Å, is very short compared to the usual O - O distances in CuO_4 groups for other compounds (2.6 - 3.2 Å). This is due to the fact that the CuO_4 group shares the O2a - O2b edge with a strongly rigid (BO_3) planar group, that imposes strain to the CuO_4 group. Typical values of O - O distances in (BO_3) groups are 2.2 - 2.5 Å.

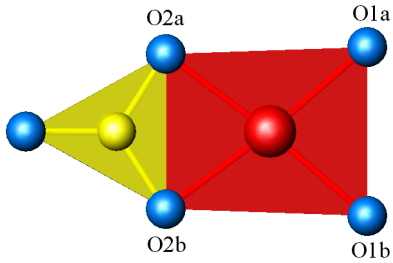

Figure 3.4: Distorted CuO_4 group. The atoms O1a and O1b are equivalent, like the atoms O2a and O2b.

Distances (Å)		Angles (°)	
O2a - O1a	3.02 (1)	O2a - Cu - O1a	102.4 (4)
O1a - O1b	2.53 (1)	O1a - Cu - O1b	82.2 (3)
O2b - O2a	2.32 (1)	O2b - Cu - O2a	72.9 (4)
		O2a - Cu - O1b	175 (6)

Table 3.3: Distances and angles in the CuO_4 group, calculated from [19].

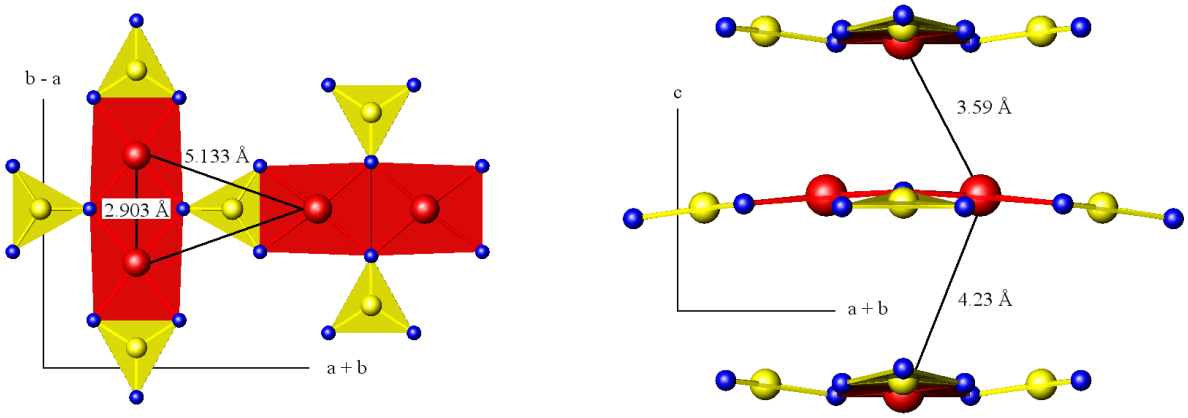

Figure 3.5: Left: Shortest intralayer Cu - Cu distances. Right: Shortest interlayer Cu - Cu distances.

The Cu - Cu distances in the structure deserve additional considerations because of their influence on the magnetic properties of $SrCu_2(BO_3)_2$. Within the $Cu_2(BO_3)_2$ - layers, the shortest Cu - Cu distance is 2.903 (1) Å, and the distance between next nearest neighbors is 5.133 (1) Å. Due to the corrugation of the layers, there are two different shortest interlayer Cu - Cu distances, 3.593 (3) Å and 4.232 (3) Å (Fig. 3.5).

3.1.2 X-ray diffraction studies

• The Stoe - Imaging Plate Diffraction System (IPDS-I) diffractometer was mostly used in this work, since its two-dimensional detector allows fast collections of complete single crystal data sets. It is also particularly useful to detect superstructures or incommensurate phases.
The crystal-detector distance is adjustable by moving the detector forward or backwards (4 - 20 cm). The detector has a diameter of 18 cm. Thus, the maximal 2θ value accessible in a measurement is 66 °, leading to minimal accessible d - values of 0.65 Å for $\lambda(\mathrm{Mo\,K}\alpha)$, if the unit cell of the crystal is small enough to avoid overlap of reflections. The crystal is only rotated around the φ - axis.
In the following, the conditions of a measurement with the Stoe-IPDS-I diffractometer will always be summarized as in table 3.4. For further details about the Stoe-IPDS-I diffractometer and softwares see [26] and [27].

U (kV)	I (mA)	φ - range (°)	$\Delta\varphi$ (°)	d (mm)	2θ - range (°)	t (mn)
X-ray tube voltage	X-ray tube intensity	Range of the φ - scan	Intervall in φ for one frame	Crystal - detector distance	Minimum - maximum 2θ available	Irradiation time per frame

Table 3.4: Conditions of a measurement with the Stoe-IPDS-I diffractometer.

Our first experiment on $SrCu_2(BO_3)_2$ was performed on the Stoe-IPDS-I diffractometer (Mo Kα), with a $0.19 \times 0.16 \times 0.15$ mm^3 single crystal. The conditions of the data collection are given in table 3.5. The linear absorption coefficient of $SrCu_2(BO_3)_2$ for this radiation is $\mu = 177.17\,\mathrm{cm}^{-1}$, and the internal R - values of the data set, for the space group $I\bar{4}2m$, before and after numerical absorption correction (programs X-RED and X-SHAPE, [28]) are 11.73 % and 3.66 %, respectively.
The lattice parameters (Tab. 3.6) were obtained more accurately by a profile matching refinement, with the program FULLPROF [29], of a powder X-ray data set at room temperature (Siemens D500 diffractometer, $\lambda(\mathrm{Cu\,K}\alpha_1) = 1.5406$ Å). Silicon was used as an internal standard in the ratio 1 : 1 to improve the accuracy. The cell parameters thus obtained compare well with the ones from the single crystal diffraction experiments.

U (kV)	I (mA)	φ - range (°)	$\Delta\varphi$ (°)	d (mm)	2θ - range (°)	t (mn)
50	20	70 - 300	2	80	2.9 - 48.4	2.5

Table 3.5: Conditions of the measurement with the Stoe-IPDS-I diffractometer.

The refinement on F^2_{obs} was stable (program SHELXL [30]), and except for the B atom, anisotropic thermal displacement parameters were used. The R - values at the end of

the refinement, for 26 parameters[1], are R1 = 1.77 % for all the 243 data, wR2 = 3.87 %, and the goodness of fit GooF = 3.41. Tables 3.6 and 3.7 contain the structural parameters from the results of the refinements, which are consistent with [19].

Space group		a (Å)	c (Å)	V (Å^3)	Z
$I\bar{4}2m$		8.9920 (4) *	6.6477 (4) *	536.7 (3) *	4
Atom	Multiplicity	x	y	z	Site symmetry
Sr	4	0	$\frac{1}{2}$	0	222
Cu	8	0.11419 (5)	0.11419 (5)	0.2781 (1)	..m
B	8	0.2942 (5)	0.2942 (5)	0.242 (1)	..m
O1	8	0.4016 (3)	0.4016 (3)	0.212 (1)	..m
O2	16	0.3276 (3)	0.1458 (3)	0.2565 (8)	1

Table 3.6: Room temperature structure of $SrCu_2(BO_3)_2$: atomic coordinates.
* Lattice parameters and volume from X-ray powder diffraction experiment.

Atom	U_{11} (Å^2)	U_{22} (Å^2)	U_{33} (Å^2)	U_{12} (Å^2)	U_{13} (Å^2)	U_{23} (Å^2)
Sr	0.0090 (5)	0.0092 (5)	0.0096 (5)	0	0	0
Cu	0.0057 (3)	0.0057 (3)	0.0246 (6)	-0.0003 (2)	0 (n.s.)	0 (n.s.)
B	0.009 (1)	non positive definite if anisotropic				
O1	0.008 (1)	0.008 (1)	0.050 (5)	0 (n.s.)	0.003 (2)	0.003 (2)
O2	0.010 (1)	0.007 (1)	0.021 (2)	0 (n.s.)	0 (n.s.)	0.004 (2)

Table 3.7: Room temperature structure of $SrCu_2(BO_3)_2$: thermal displacement parameters.

With this refinement, the thermal ellipsoid of the Sr atom is isotropic. This result is more satisfactory than in [19], since there is no structural reason for the Sr atom to have an anisotropic thermal ellipsoid.
We also discovered inversion twins at room temperature (about 50 % in volume for both orientations), which is an indication for an eventual phase transition at higher temperatures. We found a structural phase transition at 395 K, towards a centrosymmetric space group of higher symmetry, which will be discussed in section 3.4, page 39.

• We performed another single crystal diffraction study of the same crystal on a four-circle diffractometer (Mo Kα). This four-circle diffractometer is a special prototype, developed in collaboration between the Philips company and the Institut für Kristallographie. Its properties and applications are discussed in [31].
The measured 2θ - range is $2.0\,^\circ - 129.3\,^\circ$, the internal R-values before and after numerical absorption correction are 20.15% and 4.3 %, respectively. The anisotropic thermal

[1] Scale factor, atomic coordinates, thermal parameters, extinction and inversion twin domain volume, minus the non significant values (n.s., $\leqslant \sigma$) that are set to 0.

displacement parameters could be refined for all atoms. The R - values for the 30 parameters[2] are R1 = 4.05 % for 1158 unique reflections with F_{obs} ¿ $4\,\sigma_{F_{obs}}$, R1 = 6.94 % for all 1552 data, wR2 = 4.81 %, and the goodness of fit GooF = 1.65. There was no significant change between the refinements using scattering factors of atoms or ions. The structural parameters are summarized in tables 3.8 and 3.9.
From tables 3.7 and 3.9, we see that while the thermal ellipsoid for the Sr atom is isotropic, the ones for the atoms in the plaquette show a pronounced elongation in the direction of the c axis (Fig. 3.6). This is clearly not an artefact of the absorption effects.

Atom	Multiplicity	x	y	z	Site symmetry
Sr	4	0	$\frac{1}{2}$	0	222
Cu	8	0.11417 (3)	0.11417 (3)	0.27854 (8)	..m
B	8	0.2952 (2)	0.2952 (2)	0.2411 (8)	..m
O1	8	0.4012 (1)	0.4012 (1)	0.2099 (6)	..m
O2	16	0.3271 (1)	0.1462 (1)	0.2555 (5)	1

Table 3.8: Room temperature structure of $SrCu_2(BO_3)_2$: atomic coordinates.

Atom	U_{11} (Å^2)	U_{22} (Å^2)	U_{33} (Å^2)	U_{12} (Å^2)	U_{13} (Å^2)	U_{23} (Å^2)
Sr	0.0090 (2)	0.0091 (2)	0.0098 (1)	0	0	0
Cu	0.00611 (7)	0.00611 (7)	0.0235 (2)	-0.0008 (1)	0.0004 (1)	0.0004 (1)
B	0.0076 (6)	0.0076 (6)	0.015 (2)	0 (n.s.)	0 (n.s.)	0 (n.s.)
O1	0.0073 (4)	0.0073 (4)	0.044 (2)	0 (n.s.)	0.0020 (8)	0.0020 (8)
O2	0.0054 (4)	0.0077 (5)	0.0220 (8)	0.0006 (4)	0.0011 (8)	0.0026 (8)

Table 3.9: Room temperature structure of $SrCu_2(BO_3)_2$: thermal displacement parameters.

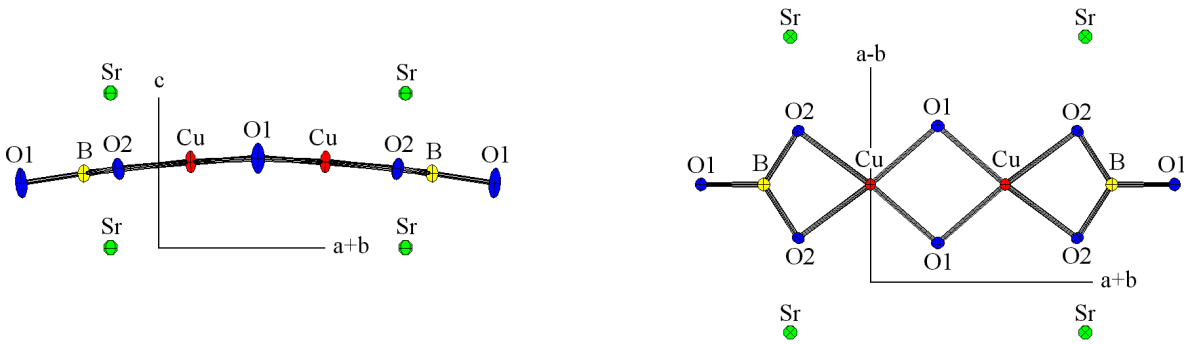

Figure 3.6: $Cu_2(BO_3)_2$ plaquette. Left: with the c axis vertical. Right: in the $(\mathbf{a}, \mathbf{b})$ plane.

[2]The same 30 parameters as in tables 3.6 and 3.7, minus U_{eq}(B), plus 4 independent parameters for the anisotropic thermal parameters of the B atom, minus the non significant (n.s.) thermal parameters.

This large elongation of the thermal ellipsoids of the Cu, O and B atoms may point out an anharmonicity or a double-well characteristic of the potential in this part of the structure. However, in spite of the absorption correction, the strong decrease of the intensities at high 2θ doesn't allow us to refine anharmonic tensors with this data set.

3.1.3 Single crystal neutron diffraction

The $SrCu_2(BO_3)_2$ single crystal we used for the neutron diffraction experiments ($1.3 \times 2.0 \times 3.1$ mm^3, containing only the isotope ^{11}B) was grown by the team of Prof. Yukata Ueda [3]. The aim of this measurement was to determine, at room temperature, the importance of anharmonicity in the structure, in order to explain the large elongation of the thermal ellipsoids (Fig. 3.6).

The experiment was performed on the 5C2 four-circle diffractometer at the LLB [4]. The wavelength of the neutrons was set to 0.8305 Å. We measured the intensities of reflections in the range $2° < 2\theta < 102°$. The reflections with $2\theta < 90°$ were measured with an usual 2θ scan, while the ones with $2\theta > 90°$ were measured with a 2θ-ω scan.

The internal R-value of the data set is 2.44 %: The absorption of neutrons by the crystal is very weak. However, the effects of extinction were not to be neglected. An isotropic type II distribution was used for the secondary extinction, and the structure was refined using the program JANA2000 [32]. The R-values for the 32 parameters [5] are R1 = 4.82 % for all 1251 unique reflections, wR2 = 8.70 %, and the goodness of fit GooF = 3.42. It makes no sense to refine the volume percentage of each twin component, since there is no anomalous dispersion for neutrons and they are therefore not sensitive to inversion twins. Tables 3.10 and 3.11 give the results of the refinement for the harmonic model, in order to compare with the X-ray data.

Atom	Multiplicity	x	y	z	Site symmetry
Sr	4	0	$\frac{1}{2}$	0	222
Cu	8	0.11432 (6)	0.11432 (6)	0.2785 (2)	..m
B	8	0.29505 (6)	0.29505 (6)	0.2416 (2)	..m
O1	8	0.40129 (8)	0.40129 (8)	0.2100 (3)	..m
O2	16	0.32731 (7)	0.14566 (7)	0.2551 (2)	1

Table 3.10: Room temperature structure of $SrCu_2(BO_3)_2$: atomic coordinates.

[3] Institute for Solid State Physics, Tokyo, Japan
[4] Laboratoire commun CEA - CNRS
[5] Atomic positions, anisotropic thermal parameters, scale factor and extinction

Atom	U_{11} (Å^2)	U_{22} (Å^2)	U_{33} (Å^2)	U_{12} (Å^2)	U_{13} (Å^2)	U_{23} (Å^2)
Sr	0.0044 (6)	0.0057 (6)	0.0028 (4)	0	0	0
Cu	0.0015 (2)	0.0015 (2)	0.0183 (5)	-0.0007 (2)	0.0007 (2)	0.0007 (2)
B	0.0018 (2)	0.0018 (2)	0.0091 (4)	-0.0005 (2)	0.0006 (3)	0.0006 (3)
O1	0.0017 (2)	0.0017 (2)	0.039 (1)	-0.0003 (3)	0.0016 (4)	0.0016 (4)
O2	0.0028 (2)	0.0021 (2)	0.0145 (3)	0.0002 (2)	0.0009 (4)	0.0012 (4)

Table 3.11: Room temperature structure of $SrCu_2(BO_3)_2$: thermal displacement parameters.

Figures 3.7 and 3.8 (pages 28 and 29) show difference Fourier maps around all the atoms at the end of the refinement. The difference between two contours for each map is 0.75 barn/Å^3. The plain and dashed lines represent the positive and negative contours, respectively.

The residues in the difference Fourier maps around the Cu, B and oxygen atoms are greater than the ones around the Sr atom. Since the thermal ellipsoid of the Sr atom is almost isotropic, we can consider that there is no need to refine anharmonic displacement parameters for this atom.
On the other hand, the O1 atom has the most anisotropic thermal tensor:

$$\frac{U_{33}}{U_{11}}\,(\mathrm{O1}) \approx 23, \quad \frac{U_{33}}{U_{11}}\,(\mathrm{Cu}) \approx 12, \quad \frac{U_{33}}{U_{11}}\,(\mathrm{O2}) \approx 7, \quad \frac{U_{33}}{U_{11}}\,(\mathrm{B}) \approx 5$$

Moreover, the difference Fourier map around the O1 atom contains very high peaks compared to the other atoms, especially in the c direction, which is the direction of the elongation of the thermal ellipsoid (Fig. 3.8). The structure was thus first refined with an anharmonic tensor of 3^{rd} order for the O1 atom, using the program JANA2000, since it is not possible to refine anharmonic tensors with SHELXL.

The results of the refinement with a 3^{rd} degree anharmonic thermal tensor for the O1 atom are listed in tables 3.12 (page 29), 3.13 and 3.14 (page 30). The R-values for the 37 parameters[6] are R1 = 4.34 % for all the 1251 data, wR2 = 3.51 %, and the goodness of fit GooF = 4.22. The R-values didn't improve a lot by refining anharmonic parameters for the O1 atom, but the residues in the difference Fourier maps, around all the atoms and particularly around the O1 atom, are greatly reduced (Fig. 3.9 and 3.10, pages 31 and 32).

[6]The same parameters as in tables 3.10 and 3.11, plus the anharmonic thermal parameters of the O1 atom.

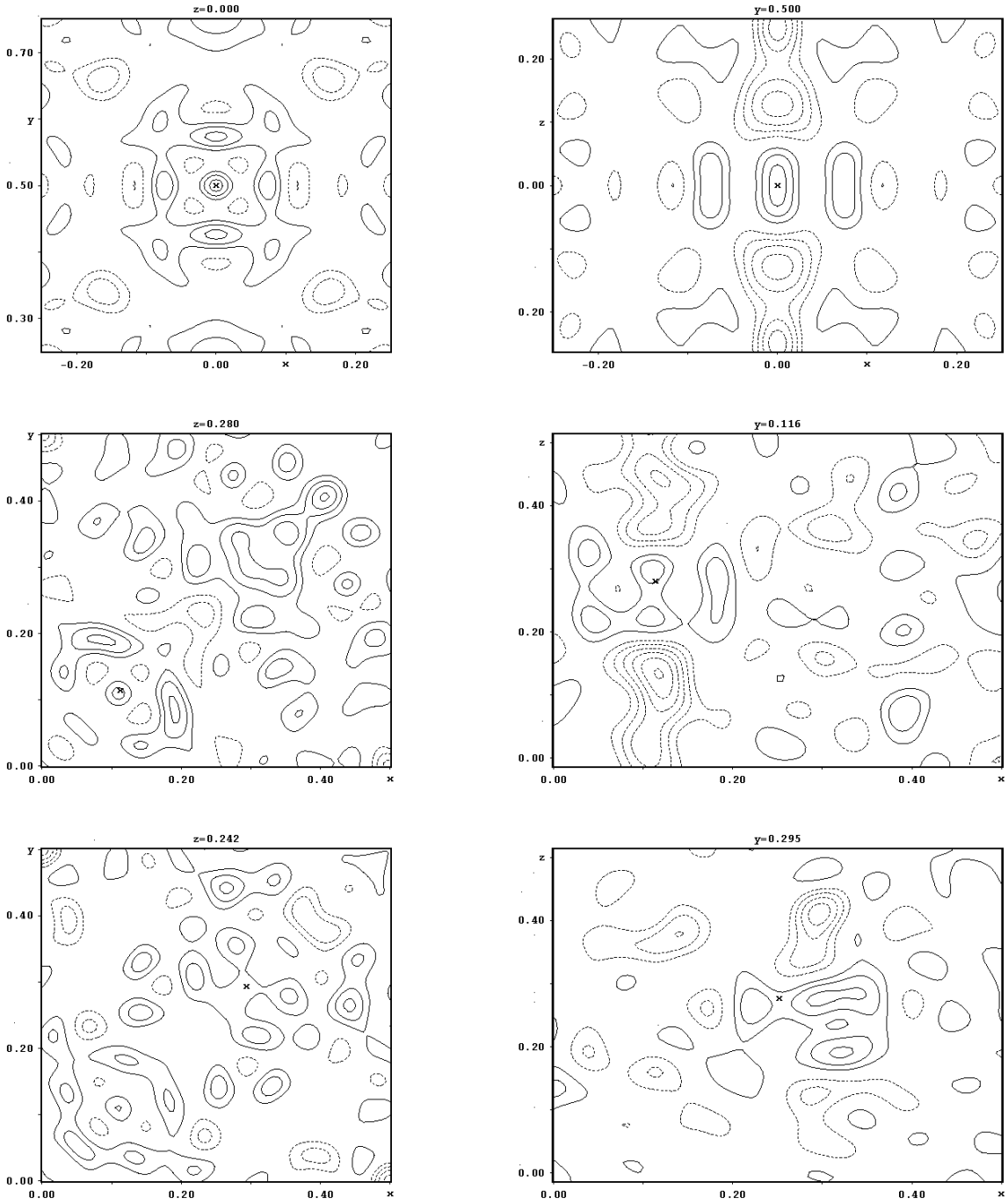

Figure 3.7: Difference Fourier maps at the end of the harmonic refinement for the room temperature structure of $SrCu_2(BO_3)_2$ (neutrons). Top: Sr atom. Middle: Cu atom. Bottom: B atom. Left: Cut in the (**a**, **b**) plane. Right: Cut in the (**a**, **c**) plane. In each map, the cross indicates the position of the atom. The difference between two contours is $0.75\,\mathrm{barn}/\mathrm{\AA}^3$.

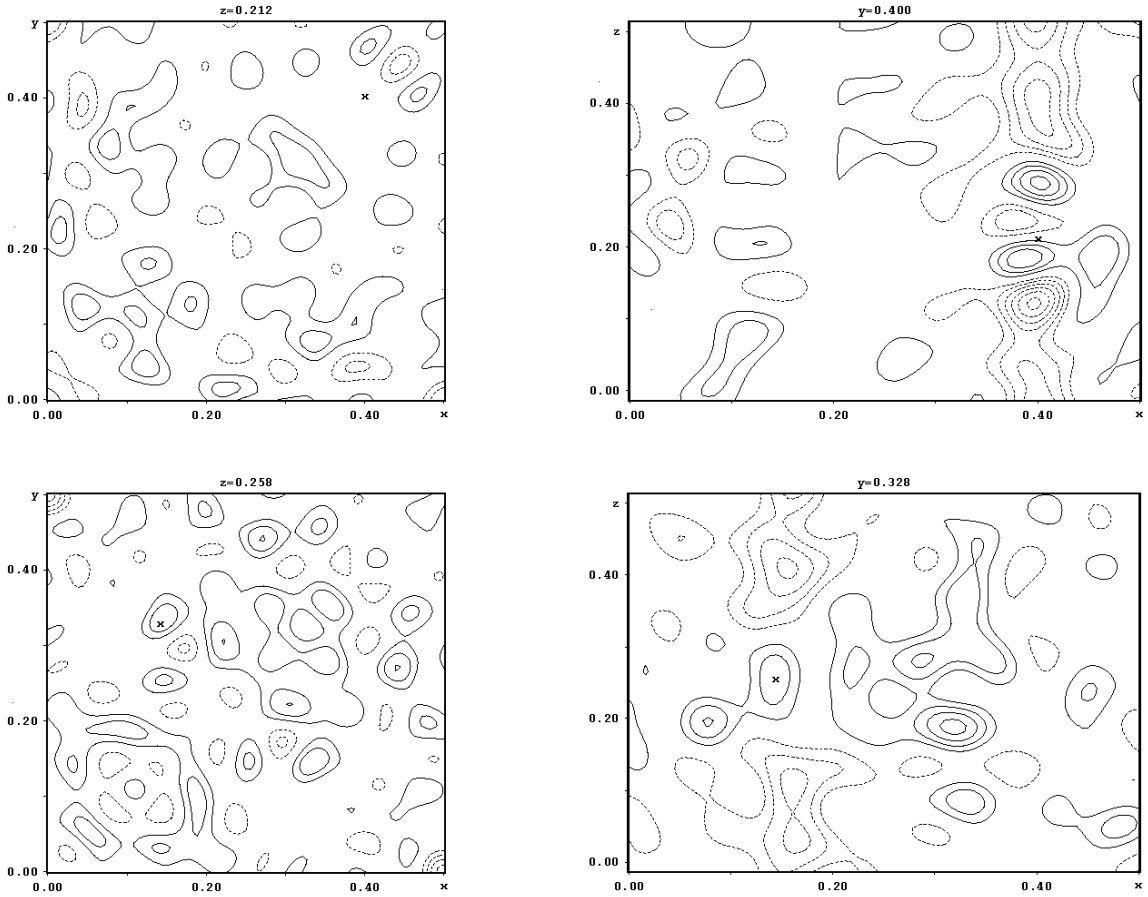

Figure 3.8: Difference Fourier maps at the end of the harmonic refinement for the room temperature structure of $SrCu_2(BO_3)_2$ (neutrons). Top: O1 atom. Bottom: O2 atom. Left: Cut in the (**a**, **b**) plane. Right: Cut in the (**a**, **c**) plane. In each map, the cross indicates the position of the atom. The difference between two contours is 0.75 barn/Å^3.

Atom	Multiplicity	x	y	z	Site symmetry
Sr	4	0	$\frac{1}{2}$	0	222
Cu	8	0.11430 (5)	0.11430 (5)	0.2786 (1)	$..m$
B	8	0.29502 (5)	0.29502 (5)	0.2418 (2)	$..m$
O1	8	0.4014 (1)	0.4014 (1)	0.2115 (5)	$..m$
O2	16	0.32736 (6)	0.14557 (6)	0.2552 (2)	1

Table 3.12: $SrCu_2(BO_3)_2$ at room temperature (anharmonic refinement): atomic coordinates.

Atom	U_{11} (Å^2)	U_{22} (Å^2)	U_{33} (Å^2)	U_{12} (Å^2)	U_{13} (Å^2)	U_{23} (Å^2)
Sr	0.0040 (5)	0.0052 (5)	0.0040 (4)	0	0	0
Cu	0.0011 (1)	0.0011 (1)	0.0181 (4)	-0.0008 (2)	0.0005 (2)	0.0005 (2)
B	0.0013 (2)	0.0013 (2)	0.0103 (4)	-0.0005 (2)	0.0006 (2)	0.0006 (2)
O1	0.0014 (2)	0.0014 (2)	0.043 (1)	-0.0002 (3)	0.0019 (3)	0.0019 (3)
O2	0.0022 (2)	0.0017 (2)	0.0155 (3)	0.0002 (2)	0.0010 (3)	0.0014 (3)

Table 3.13: $SrCu_2(BO_3)_2$ at room temperature (anharmonic refinement): thermal displacement parameters.

C_{111} (Å^3)	0.0004 (2)	C_{133} (Å^3)	0.0003 (5)
C_{112} (Å^3)	-0.0000 (1)	C_{222} (Å^3)	0.0004 (2)
C_{113} (Å^3)	-0.0008 (2)	C_{223} (Å^3)	-0.0008 (2)
C_{122} (Å^3)	-0.0000 (1)	C_{233} (Å^3)	0.0003 (5)
C_{123} (Å^3)	-0.0001 (3)	C_{333} (Å^3)	0.014 (2)

Table 3.14: $SrCu_2(BO_3)_2$ at room temperature (anharmonic refinement): components of the 3^{rd} degree anharmonic tensor for the O1 atom (C_{ijk} multiplied by 10^3). The non significant parameters have been left in the results to show that they are not significant.

The refinement with anharminic thermal parameters for the O1 atom leads to a significantly shifted z(O1) position, compared to the harmonic refinement (Tab. 3.12).

However, the only really significant anharmonic parameter is C_{333}, all the others are almost 0 within three standard deviations (Tab. 3.14). Also, the anisotropy of the thermal ellipsoids for all the atoms is increased:

$$\frac{U_{33}}{U_{11}}\,(\mathrm{O1}) \approx 31, \quad \frac{U_{33}}{U_{11}}\,(\mathrm{Cu}) \approx 16, \quad \frac{U_{33}}{U_{11}}\,(\mathrm{O2}) \approx 8, \quad \frac{U_{33}}{U_{11}}\,(\mathrm{B}) \approx 8$$

Further refinements with anharmonic thermal tensors for other atoms (except Sr) or tensors of higher order for the O1 atom didn't improve the structural data: the R - values decreased only very slightly, the anharmonic parameters were not really significant, and there was almost no effect on the residues in the difference Fourier maps.

As a conclusion, the potential around the atoms of a $Cu_2(BO_3)_2$ - layer can be well considered as harmonic almost everywhere, except in the c direction around the O1 atom. In fact, the strong elongation of the thermal ellipsoids of the atoms in the direction normal to the layers is a frequent feature in two-dimensional systems with weak chemical bonds between the layers.

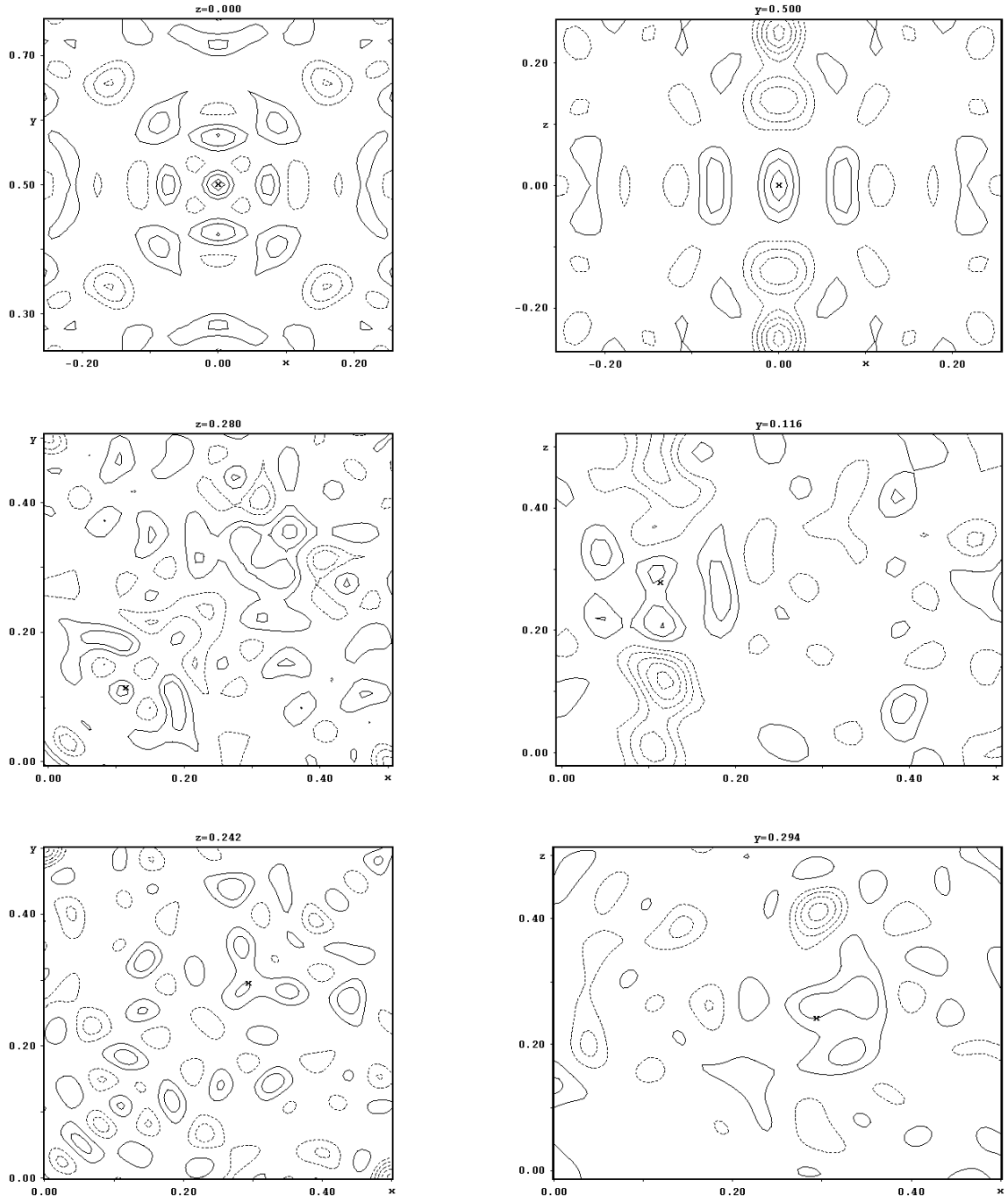

Figure 3.9: Difference Fourier maps at the end of the anharmonic refinement of the O1 atom for the room temperature structure of $SrCu_2(BO_3)_2$ (neutrons). Top: Sr atom. Middle: Cu atom. Bottom: B atom. Left: Cut in the (**a**, **b**) plane. Right: Cut in the (**a**, **c**) plane. In each map, the cross indicates the position of the atom. The difference between two contours is 0.75 barn/Å^3.

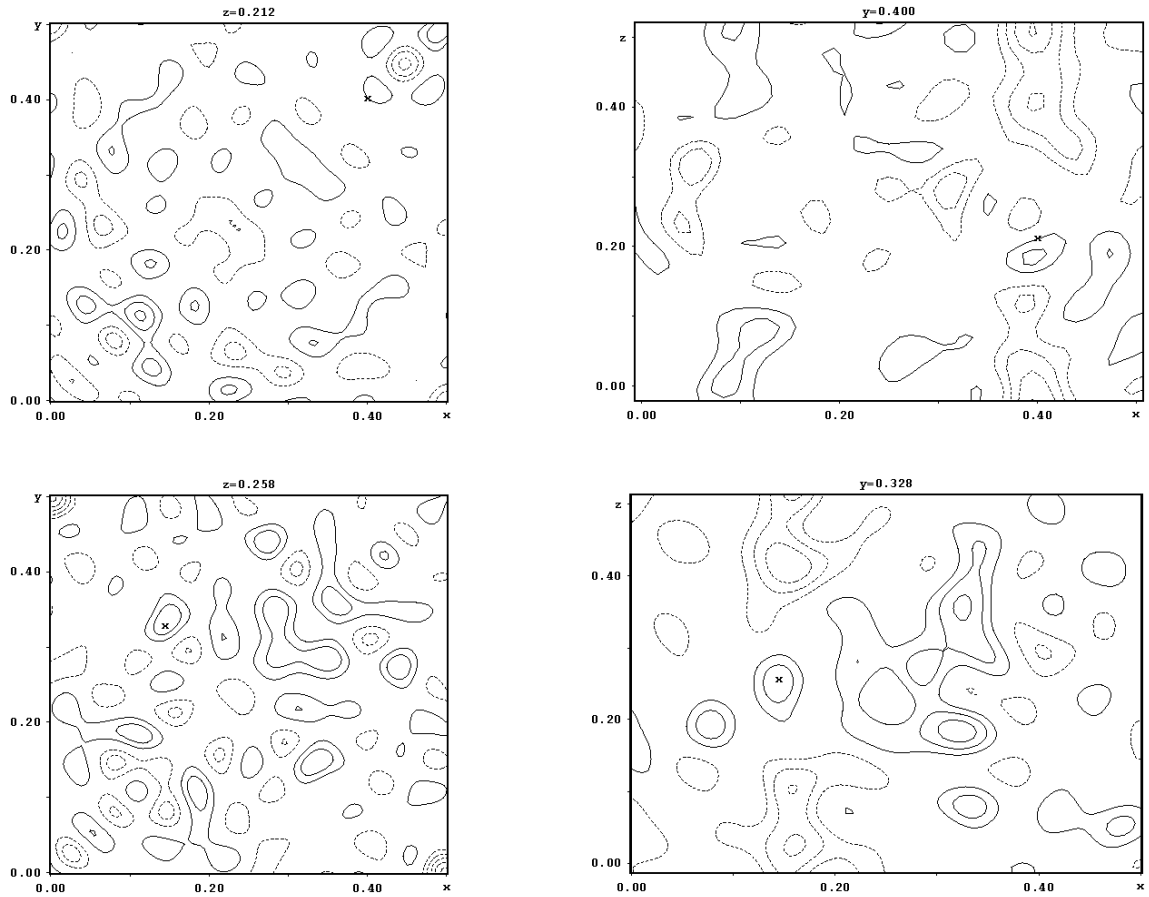

Figure 3.10: Difference Fourier maps at the end of the anharmonic refinement of the O1 atom for the room temperature structure of $SrCu_2(BO_3)_2$ (neutrons). Top: O1 atom. Bottom: O2 atom. Left: Cut in the (**a**, **b**) plane. Right: Cut in the (**a**, **c**) plane. In each map, the cross indicates the position of the atom. The difference between two contours is 0.75 barn/Å^3.

3.2 Magnetic properties

3.2.1 The Shastry-Sutherland model

$SrCu_2(BO_3)_2$ is the only known compound to which the two-dimensional Shastry-Sutherland model [33] can be applied. Figure 3.11 describes the magnetic interactions between spins $\frac{1}{2}$ in this model.

The Hamiltonian for this system is written as

$$\mathscr{H} = J \sum_{\langle i,j \rangle} S_i \, S_j + J' \sum_{\langle i,j \rangle} S_i \, S_j$$

where the first term represents the nearest neighbor coupling J and the second one represents the frustrating second nearest neighbor coupling J'.

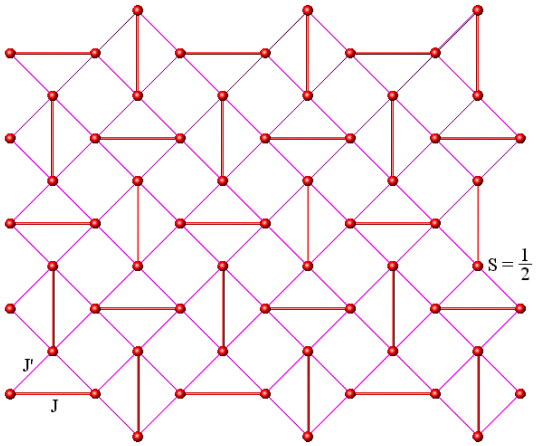

Figure 3.11: The Shastry - Sutherland model. The full circles represent the locations of the spins $\frac{1}{2}$.

For $J' \ll J$, the spins $\frac{1}{2}$ form quasi-isolated dimers, and the ground state of the system is exactly solvable: this is the exact dimer ground state, with a spin gap [33]. In the case $J' \gg J$, the system is equivalent to the two-dimensional square lattice Heisenberg model.

From this two-dimensional model, a phase diagram was calculated [34], showing the different magnetic phases one can obtain by varying the temperature and the ratio $\frac{J'}{J}$ of the coupling constants (Fig. 3.12).

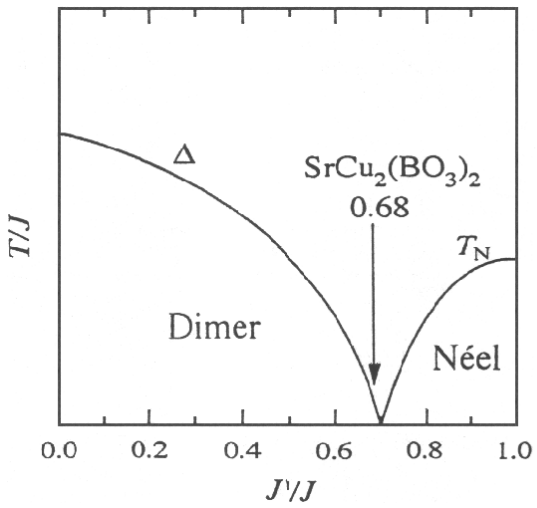

Figure 3.12: Phase diagram for the Shastry - Sutherland model (Fig. 2 from [35]).

At high temperatures, the system is in a paramagnetic state. By lowering the temperature and for small values of $\frac{J'}{J}$, the system undergoes a phase transition into a disordered exact dimer state, where the quasi-isolated dimers are in a triplet ground state of spin zero. At low temperatures, with increasing values of $\frac{J'}{J}$, the magnetic interactions between the dimers become greater and the system undergoes a phase

transition into an ordered Néel state. The critical point between the dimer and Néel states was calculated to be $\left(\frac{J'}{J}\right)_c = 0.7 \pm 0.01$ [34]. In fact, in a small region of the phase diagram between the dimer and Néel states, there exists another disordered phase that was not mentionned in [34], where the spins $\frac{1}{2}$ form plaquettes (see figure 3.41, page 59).

3.2.2 Magnetic properties of $SrCu_2(BO_3)_2$

$SrCu_2(BO_3)_2$ is a quasi-two dimensional spin gap system, with a gap of 30 K [36].
The arrangement of the Cu^{2+} ions ($S = \frac{1}{2}$) in the $Cu_2(BO_3)_2$ - layers (Fig. 3.13) is topologically equivalent to the Shastry-Sutherland model. The Cu^{2+} ions lie on a triangular array and are coupled antiferromagnetically via the oxygen atoms (not represented in the figure). The interactions J and J' are both antiferromagnetic, and the ratio $\frac{J'}{J}$ was estimated to be 0.68 [34], thus very close to the dimer - Néel critical point in the phase diagram of figure 3.12: Even small changes in the structure of $SrCu_2(BO_3)_2$ (induced, for instance, by the substitution of Sr by Ba or Ca) could change the magnetic ground state of the system.
In spite of the large $\frac{J'}{J}$ value, $SrCu_2(BO_3)_2$ is the first compound achieving the exact dimer ground state.

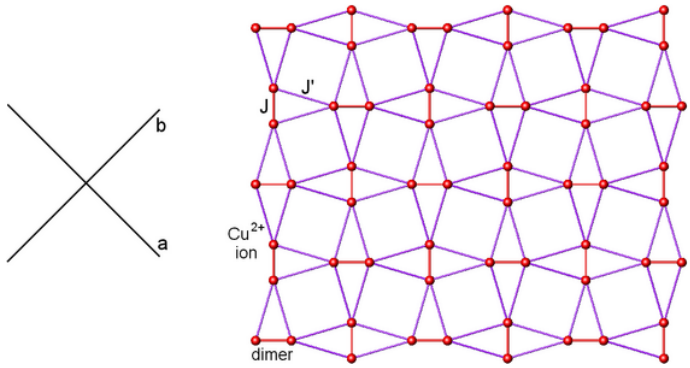

Figure 3.13: Magnetic interactions between the Cu^{2+} ions in the $Cu_2(BO_3)_2$ - sheets.

The magnetic susceptibility of $SrCu_2(BO_3)_2$ was measured between 4.3 K and 450 K by Prof. Heiko Lueken [7] with a SQUID magnetometer (Fig. 3.14, [37]).
The maximum around 15 K in the susceptibility curve is rather broad, which is a typical feature in the case of low dimensional magnetic compounds. From room temperature down to 15 K, the compound is paramagnetic; below 15 K, a spin gap $\Delta = 30$ K opens. $SrCu_2(BO_3)_2$ shows no sign of magnetic ordering down to 4.3 K.

[7] Institut für Anorganische Chemie, RWTH-Aachen

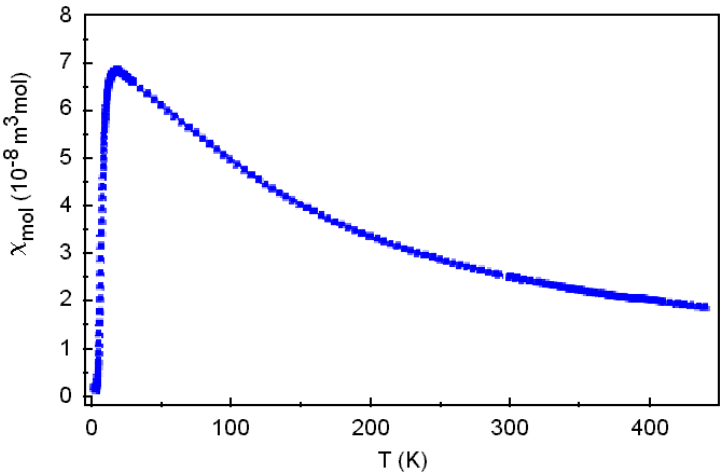

Figure 3.14: Temperature dependence of the magnetic susceptibility of $SrCu_2(BO_3)_2$.

The magnetization curve of $SrCu_2(BO_3)_2$, measured on single crystals at low temperatures (Fig. 3.15), presents plateaux at $\frac{1}{4}$, $\frac{1}{8}$ and $\frac{1}{10}$ of the full Cu^{2+} saturation moment [20, 38], which were theoretically discussed in [39, 40, 41, 42].
This phenomenon was so far only known to exist in one-dimensional quantum spin systems with a ladder geometry [43].

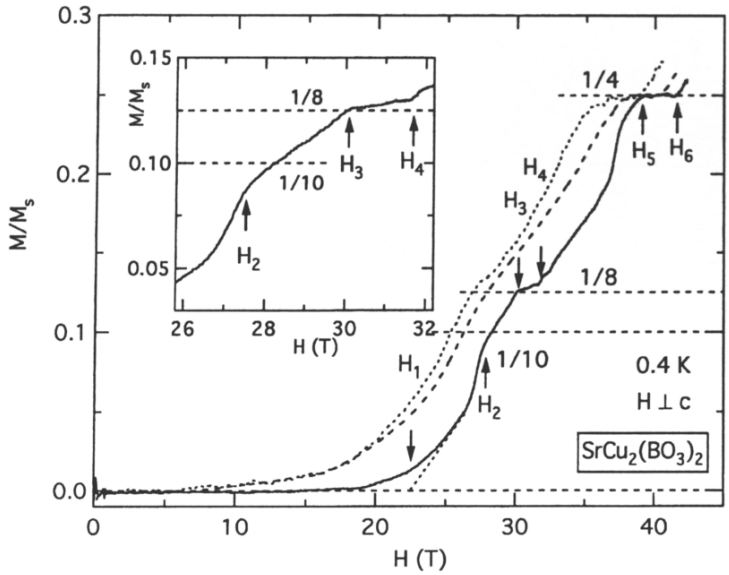

Figure 3.15: Magnetization curve of $SrCu_2(BO_3)_2$ perpendicular to the c direction (solid line), measured at 0.4 K (Fig. 3 from [38]). For comparison, the parallel and perpendicular magnetizations at 0.5 K are shown by the dotted and the broken lines, respectively. Around $H_1 = 22.5\,T$, the spin gap closes. The $\frac{1}{10}$ plateau occurs at about $H_2 = 27.5\,T$. The $\frac{1}{8}$ plateau exists between $H_3 = 30.1\,T$ and $H_4 = 31.7\,T$, and the $\frac{1}{4}$ plateau between $H_5 = 39.1\,T$ and $H_6 = 41.6\,T$.

With increasing magnetic fields, the Cu - Cu dimers are gradually excited into the triplet state $S = 1$. In order to minimize the energy of the system, the excited dimers order themselves in relatively stable superstructures, which explains the observed plateaux in the magnetization curve. The models shown in figure 3.16 were proposed for these magnetic superstructures [38]. Unfortunately, the high necessary magnetic fields for the appearence of the first plateau (at about 27 T) don't allow single crystal neutron diffraction investigations of its superstructure. Recently, K. Kodama et al. reported the observation, by means of nuclear magnetic resonance (NMR), of the magnetic superstructure in the $\frac{1}{8}$ magnetization plateau [44]: the inequivalent Cu sites in the commensurate magnetic superstructure show different NMR lines in the spectrum.

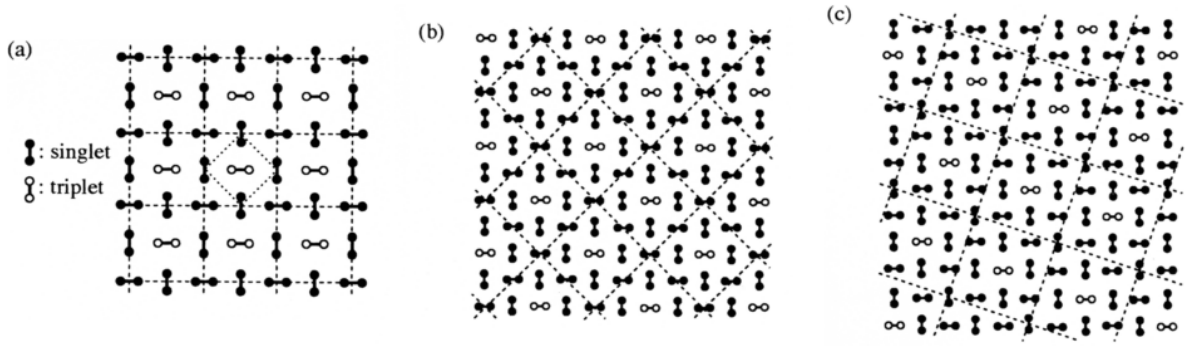

Figure 3.16: Ordered structures between the excited triplets (open) and the remaining singlets (solid), corresponding to the $\frac{1}{4}$ (a), $\frac{1}{8}$ (b) and $\frac{1}{10}$ (c) magnetization plateaux (Fig. 1 from [38]). Magnetic unit cells are denoted by broken lines, the chemical unit cell by dotted lines in (a).

Studies of doping effects on the magnetic properties of $SrCu_2(BO_3)_2$ were performed, in an attempt to change the intralayer magnetic coupling constants J and J' and then study another region of the phase diagram.
In a first attempt, Zn was incorporated into the material in order to insert diamagnetic cations in the structure [45], since the Zn^{2+} ions (S=0) were supposed to sit on the same site as the Cu^{2+} ions. In fact, only a small amount of Zn could be incorporated in the structure of $Sr(Cu_{1-x}Zn_x)_2(BO_3)_2$: $x < 0.1$. This is due to the fact that Zn usually prefers an octahedral coordination of oxygen atoms instead of a planar square one. Doping effects on the magnetic properties are mostly seen at low temperatures. Above 10 K, all the $Sr(Cu_{1-x}Zn_x)_2(BO_3)_2$ samples show the same behaviour of the magnetic susceptibility (Fig. 3.17). Below 10 K, the exact dimer ground state is still present, but the presence of Zn^{2+} ions seems to change the Curie constant. Fits of the Curie constant as a function of the Zn content indicated that the Zn atoms in the structure might arrange themselves in dimers [45].
Ba - and Ca - substitution effects on the spin gap of $SrCu_2(BO_3)_2$ were also studied by several teams [35, 46, 47], this will be developed in section 3.6, page 60.

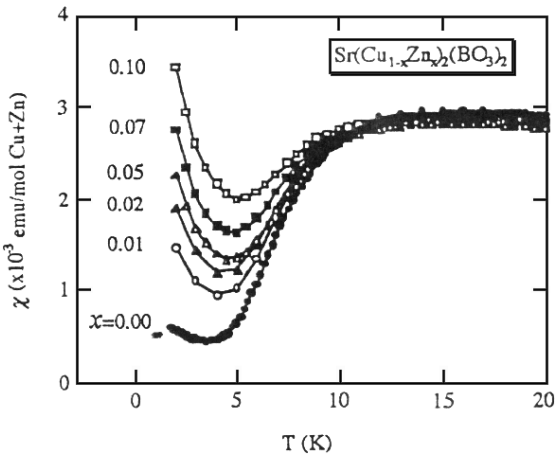

Figure 3.17: Temperature dependence of the magnetic susceptibilities of polycrystalline $Sr(Cu_{1-x}Zn_x)_2(BO_3)_2$ for $x < 0.1$ (Fig. 2 from [45]).

3.3 Evolution of the structure down to 9 K

The structural evolution of $SrCu_2(BO_3)_2$ from room temperature down to 100 K was studied by means of single crystal X-ray diffraction with the IPDS diffractometer. The crystal was cooled with a Cryostream liquid N_2 - cryostat (100 K ... 300 K, accuracy: 1 K, stability: 0.1 K). Five data sets were measured (273 K, 248 K, 198 K, 148 K and 100 K), with the conditions given in table 3.15. The crystal doesn't undergo any structural phase transition in this temperature range, but it was observed that with decreasing temperatures, the $Cu_2(BO_3)_2$ - layers become more and more corrugated.

U (kV)	I (mA)	φ - range (°)	$\Delta\varphi$ (°)	d (mm)	2θ - range (°)	t (mn)
50	20	70 - 300	2	60	3.8 - 56.3	2.5

Table 3.15: Low temperature measurements with the Stoe-IPDS-I diffractometer.

The structure of $SrCu_2(BO_3)_2$ at 9 K was measured by means of single crystal neutron diffraction on the 5C2 diffractometer at the LLB [8], with the same crystal as for the room temperature neutron diffraction experiment ($\lambda = 0.8305$ Å). We performed q - scans at 5 K and couldn't find any superstructure reflections or evidence for diffuse scattering, which indicates that no long range magnetic ordering takes place in $SrCu_2(BO_3)_2$ at low temperatures, at least above 5 K.

- $SrCu_2(BO_3)_2$ at 100 K (X-rays)

[8] Laboratoire commun CEA - CNRS

The cell parameters are $a = 8.982\,(2)$ Å, $c = 6.643\,(2)$ Å. The internal R - values of the data set before and after numerical absorption correction are 11.73 % and 3.72 %, respectively. The structure was refined with the program SHELXL, taking into account the inversion twin, and the results are given in tables 3.16 and 3.17. The R - values for the 26 parameters are R1 = 1.80 % for 359 unique reflections with F_{obs} ¿ 4 $\sigma_{F_{obs}}$, R1 = 1.82 % for all 361 data, wR2 = 3.64 %, and the goodness of fit GooF = 3.18.

Atom	Multiplicity	x	y	z	Site symmetry
Sr	4	0	$\frac{1}{2}$	0	222
Cu	8	0.11453 (4)	0.11453 (4)	0.2884 (1)	..m
B	8	0.2943 (4)	0.2943 (4)	0.2387 (9)	..m
O1	8	0.4006 (2)	0.4006 (2)	0.1990 (5)	..m
O2	16	0.3276 (2)	0.1458 (2)	0.2572 (5)	1

Table 3.16: $SrCu_2(BO_3)_2$ at 100 K: atomic coordinates.

Atom	U_{11} (Å^2)	U_{22} (Å^2)	U_{33} (Å^2)	U_{12} (Å^2)	U_{13} (Å^2)	U_{23} (Å^2)
Sr	0.0024 (3)	0.0023 (3)	0.0026 (3)	0	0	0
Cu	0.0011 (2)	0.0011 (2)	0.0069 (4)	0 (n.s.)	0.0003 (2)	0.0003 (2)
B	0.004 (1)	non positive definite if anisotropic				
O1	0.0028 (8)	0.0028 (8)	0.012 (2)	0 (n.s.)	0.002 (1)	0.002 (1)
O2	0.004 (1)	0.002 (1)	0.009 (1)	0 (n.s.)	0 (n.s.)	0.002 (1)

Table 3.17: $SrCu_2(BO_3)_2$ at 100 K: thermal displacement parameters.

- $SrCu_2(BO_3)_2$ at 9 K (neutrons)

We measured the intensities of reflections up to $2\theta = 70.55\,°$, with an internal R - value of 3.29 %. The cell parameters are $a = 8.96\,(1)$ Å, $c = 6.66\,(1)$ Å. Tables 3.18 and 3.19 give the results of the refinement, performed with the program JANA2000. The R - values at the end of the refinement for the 25 parameters are R1 = 5.47 % for all 981 unique reflections, wR2 = 5.79 %, and the goodness of fit GooF = 4.82.

From these results, we see that the thermal ellipsoids of the atoms are no more elongated along the c axis, except for the O1 atom. The thermal displacement parameters of the Sr atom are almost non significant.
The only structural change is the increase in the corrugation of the $Cu_2(BO_3)_2$ - layers. This is seen in the temperature dependence of the CuO_4 - CuO_4 and CuO_4 - BO_3 angles, defined by the angles between the normals to two adjacent CuO_4 groups and adjacent CuO_4 and BO_3 groups, respectively (Fig. 3.18).

The temperature dependences of some atomic and thermal displacement parameters will be shown together with the ones from high temperature data (Fig. 3.23 ... 3.25).

Atom	Multiplicity	x	y	z	Site symmetry
Sr	4	0	$\frac{1}{2}$	0	222
Cu	8	0.1149 (1)	0.1149 (1)	0.2902 (2)	..m
B	8	0.2952 (1)	0.2952 (1)	0.2385 (3)	..m
O1	8	0.4011 (1)	0.4011 (1)	0.1979 (3)	..m
O2	16	0.3281 (1)	0.1458 (1)	0.2578 (3)	1

Table 3.18: $SrCu_2(BO_3)_2$ at 9 K: atomic coordinates.

Atom	U_{11} (Å^2)	U_{22} (Å^2)	U_{33} (Å^2)	U_{12} (Å^2)	U_{13} (Å^2)	U_{23} (Å^2)
Sr	0.0024 (9)	0.0025 (9)	0.0002 (7)	0	0	0
Cu	0.0020 (3)	0.0020 (3)	0.0011 (7)	0 (n.s.)	0 (n.s.)	0 (n.s.)
B	0.0022 (3)	0.0022 (3)	0.0028 (3)	0 (n.s.)	0.0006 (5)	0.0006 (5)
O1	0.0021 (4)	0.0021 (4)	0.0061 (9)	0 (n.s.)	0 (n.s.)	0 (n.s.)
O2	0.0036 (5)	0.0027 (4)	0.0033 (5)	0 (n.s.)	0 (n.s.)	0.0007 (6)

Table 3.19: $SrCu_2(BO_3)_2$ at 9 K: thermal displacement parameters.

3.4 Structural phase transition at 395 K

3.4.1 Raman spectroscopy measurements

Raman spectroscopy probes the collective vibration modes of molecules in a crystal. Their frequencies lie between 10^{12} Hz and 10^{14} Hz, in the visible and infrared part of the light spectrum. The principle of the experiment is to send a monochromatic laser light of energy E on the sample. Most of the incident photons are elastically scattered (Rayleigh scattering). The others, about 1 ‰, are inelastically scattered in other directions than the incident beam. The inelastic scattering comes from the creation (Stokes process) or annihilation (anti-Stokes process) of vibrations of energy e in the material (Fig. 3.19).

Each peak in the spectrum corresponds to a vibration mode. The number and intensities of the peaks depend on the site symmetries in the crystal structure. Selection rules, for the absorption and emission of photons by the sample, govern the appearance of vibrational modes on a Raman spectrum. They depend essentially on the wave vector and the polarization vector of the incident light, and on the dipole moment vector. A

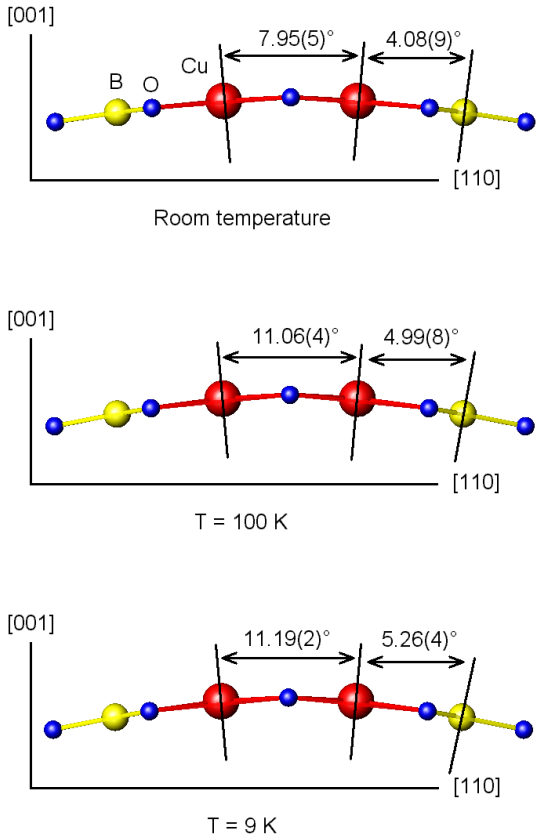

Figure 3.18: Temperature dependence of the structure of $SrCu_2(BO_3)_2$: View of a plaquette with the c axis vertical.

vibration mode appears on a Raman spectrum if its polarizability of the molecules in the crystal changes during the vibration.

The wave and polarization vectors of the incident light are noted in the following way for a Raman experiment: $k_i\,(p_i\,p_s)\,\text{-}\,k_s$, where k_i and k_s are the directions of the incident and scattered wave vectors, and p_i and p_s are the directions of the incident and scattered polarization vectors. For example, if both the incident and scattered wave vectors are parallel to the a axis of the crystal, and both the incident and scattered polarization vectors are along c, then the directions are noted $a\,(c\,c)\,-\,a$.

The Raman scattering experiments on $SrCu_2(BO_3)_2$ were done by Pr. Peter Lemmens[9], with a 448 nm excitation line of an Ar-laser [37]. The intensities of a few Raman modes were followed as a function of temperature (Fig. 3.20).
The measurements at 393 K and 524 K were performed after the discovery of the phase transition at $T_s = 395$ K.

[9]Physikalisches Institut, RWTH-Aachen

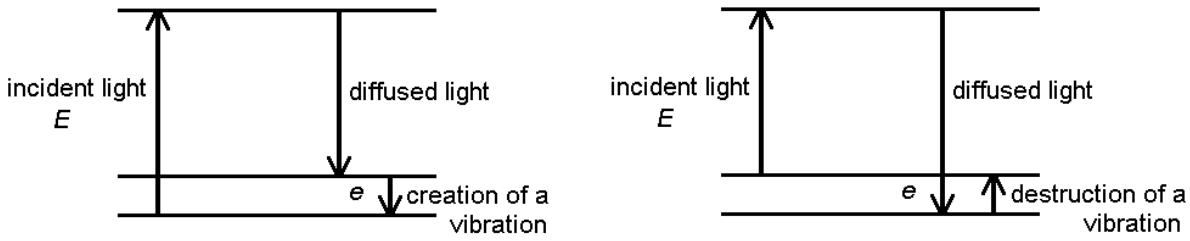

Figure 3.19: Principle of Raman spectroscopy. Left: Stokes process. Right: anti-Stokes process.

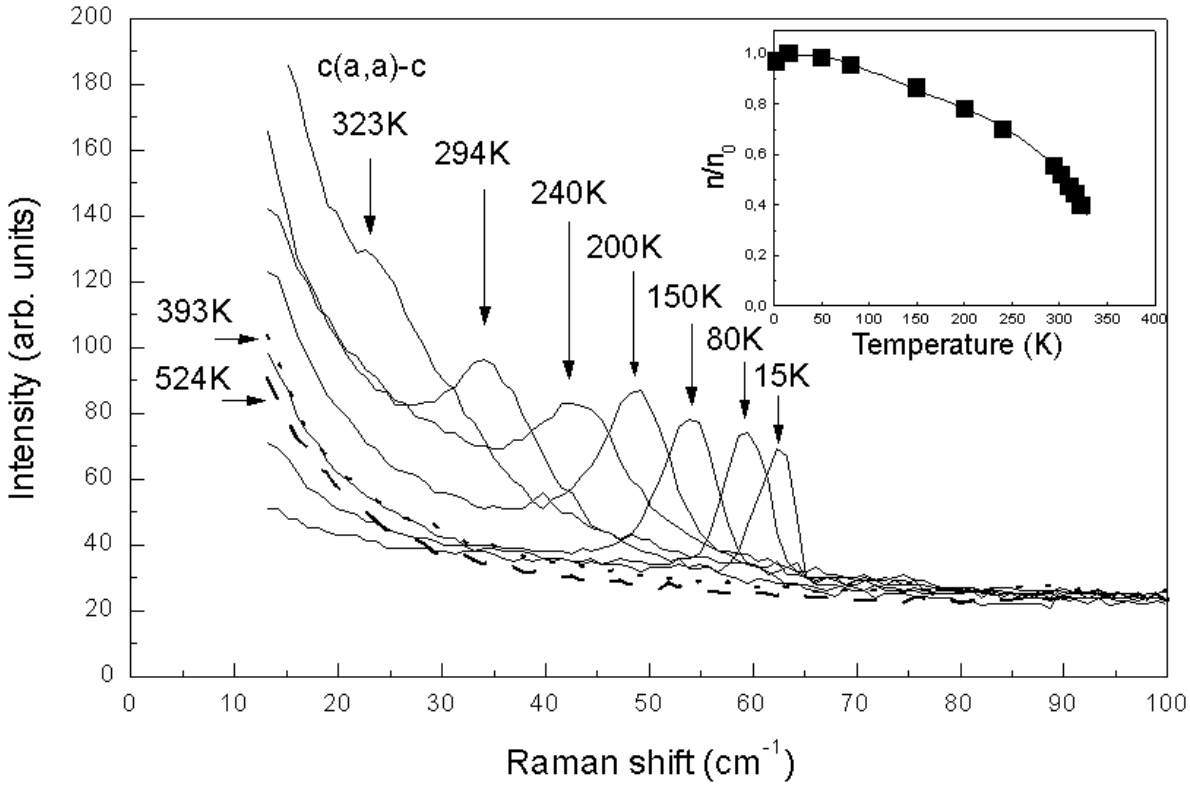

Figure 3.20: Frequency of the low temperature phonon mode with A_1 symmetry between 15 K and 524 K. Inset: Frequency of the mode, normalized to the frequency at T= 15 K [37].

Below T_s, a mode with A_1 symmetry shows a strong softening in frequency, from 62 cm−1 at 15 K down to 32 cm−1 at room temperature. Also, its linewidth becomes broader with increasing temperature. The mode vanishes into a quasi-elastic scattering contribution close to T_s.
This clearly indicates a symmetry change at T_s. Above T_s, both the mode and the quasi-elastic scattering have disappeared.

3.4.2 Study of the phase transition with X-ray diffraction

In order to follow the temperature dependent corrugation of the $Cu_2(BO_3)_2$ - layers, a total of 20 data sets was collected at different temperatures, from 100 K up to 590 K, on the Stoe-IPDS-I diffractometer. From 100 K up to room temperature, the crystal was cooled with a Cryostream liquid N_2 cryostat (100 K . . . 300 K, accuracy 0.1 K). For the high temperature measurements, a home made heating goniometer head was used, surrounded at its basis by a tube blowing hot air on the crystal. The temperature of the blown air, regulated by an Eurotherm temperature controller, was calibrated at the end of the series of measurements, with a thermocouple placed at the sample position.

• We observed that with increasing temperatures, the intensities of the reflections of the type $(h0l)$ with h and l odd decrease continuously and vanish at $T_s = 395$ K, indicating a symmetry change (Fig. 3.21). Above T_s, the crystal is still tetragonal and I - centered. We observed no hysteresis in the intensities of these reflections, and there was no drastic change in the unit cell volume upon the phase transition, which is an indication for a second order phase transition. The evolution of the cell parameters with temperature will be discussed later.

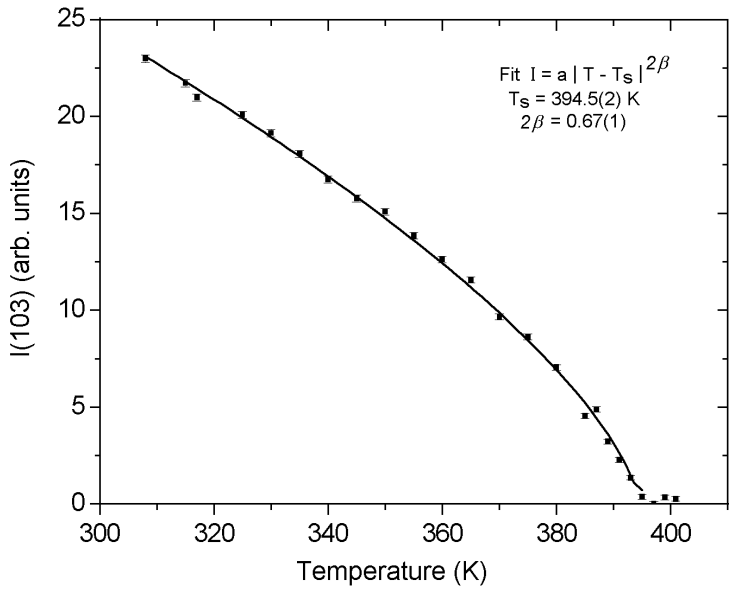

Figure 3.21: Temperature dependence of the intensity of the (103) reflection (measured on the four-circle diffractometer).

Figure 3.21 shows the temperature dependence of the (103) reflection, separately measured on the four-circle diffractometer (page 24, [31]), equipped with a cylindrical home made aluminium heating device. All the $(h0l)$ reflections with h and l odd follow this type of critical behavior, which can be described by the power law $I(T) = a\,(T_s - T)^{2\beta}$,

where T_s is the temperature at which the phase transition occurs and β is the critical exponent. The fitted values for the (103) reflection are $T_s = 395.1\,(3)$ K and $\beta = 0.34\,(1)$, very close to the theoretical value of 0.33 for a three-dimensional second order phase transition: the intensities of theses reflections appear to be an appropriate external order parameter for the phase transition.

The drop in the $(h0l)$ intensities (h, l odd) is accompanied by an increase of the (004) intensity, from 300 K up to T_s, as shown in figure 3.22. Above T_s, the (004) intensity starts to decrease. The behavior of this reflection can be understood if we look at the temperature dependence of the atomic positions - we don't consider the Sr atom, being fixed on a special position. In the $(\mathbf{a}, \mathbf{b})$ plane, the position of the atoms is quasi-independent of the temperature. But along the c direction, all the Cu, B and O atoms appear to move continuously towards the same plane, situated at $z = 0.25$ (Fig. 3.23).

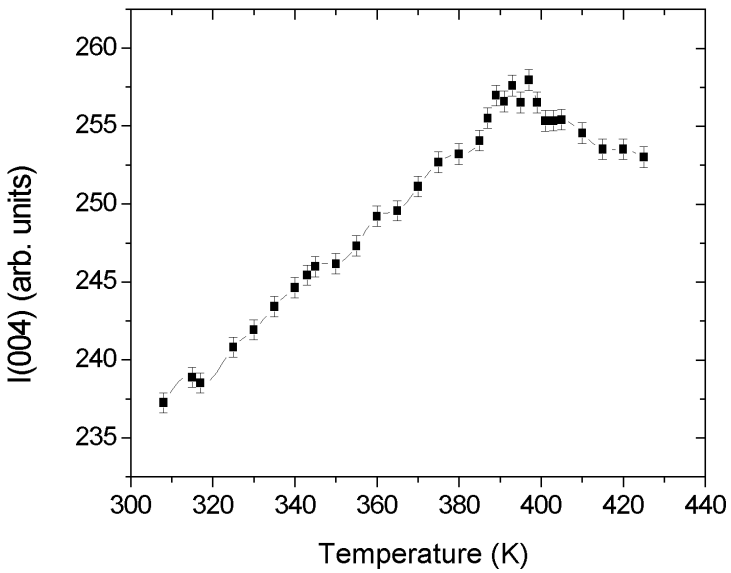

Figure 3.22: Temperature dependence of the intensity of the (004) reflection.

From the general formula for the static part of the structure factor

$$F(\vec{H}) = \sum_j f_j(\vec{H})\, e^{2i\pi \vec{H}\cdot\vec{r_j}} = \sum_j f_j(\vec{H})\, e^{2i\pi(hx_j+ky_j+lz_j)}$$

we see that the structure factor of the (004) reflection becomes maximum for the value $z = 0.25$, so that the movement of the atoms towards the plane $z = 0.25$ is directly seen in the temperature dependence of this reflection. Above T_s, the intensity of the (004) reflection decreases, due to the increasing thermal parameters of the atoms.
The temperature dependence of the $(h0l)$ reflections (h, l odd) is a direct consequence of the symmetry change at T_s, discussed later.

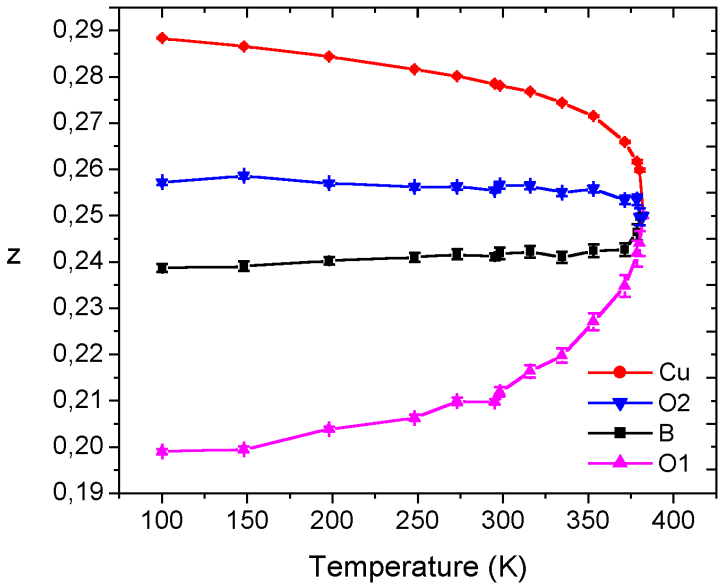

Figure 3.23: Temperature dependence of the z coordinate for the Cu, B and O atoms.

• The corrugation of the $Cu_2(BO_3)_2$ - layers is measured by the angles between the normals to two adjacent CuO_4 groups, two adjacent BO_3 groups, or adjacent CuO_4 and BO_3 groups (Fig. 3.18, page 40). As the Cu, B and O atoms move continuously towards the same plane, these angles also have a critical behavior and become zero at T_s (Fig. 3.24). They could therefore constitute good internal order parameters.

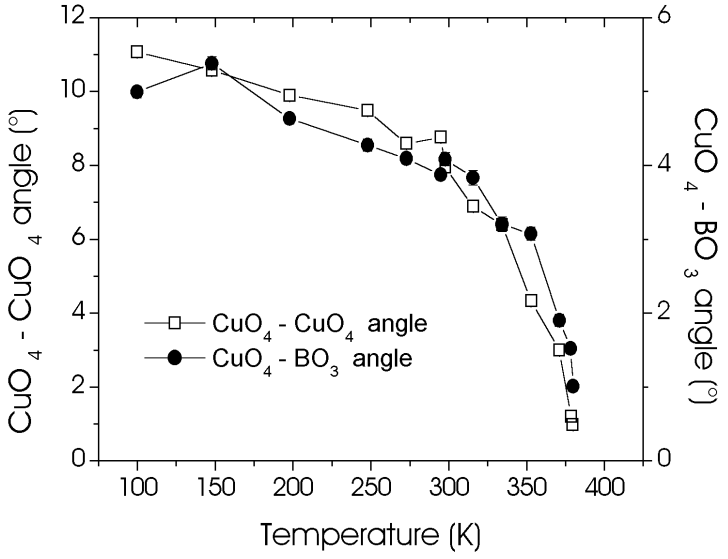

Figure 3.24: Temperature dependence of the corrugation of the $Cu_2(BO_3)_2$ - layers. The CuO_4 - CuO_4 and CuO_4 - BO_3 angles are defined in figure 3.18, page 40.

• The high anisotropy of the thermal displacement tensors, already observed at room temperature, becomes even higher when approching T_s (Fig. 3.25): For the Cu and O1 atoms, the ratio U_{33}:U_{11} increases from 3:1 at room temperature up to about 15:1 just below 395 K.
Moreover, the components of the thermal displacement tensors along the crystal axes for the Cu, B and O atoms exhibit a strongly non linear temperature dependence below the phase transition.

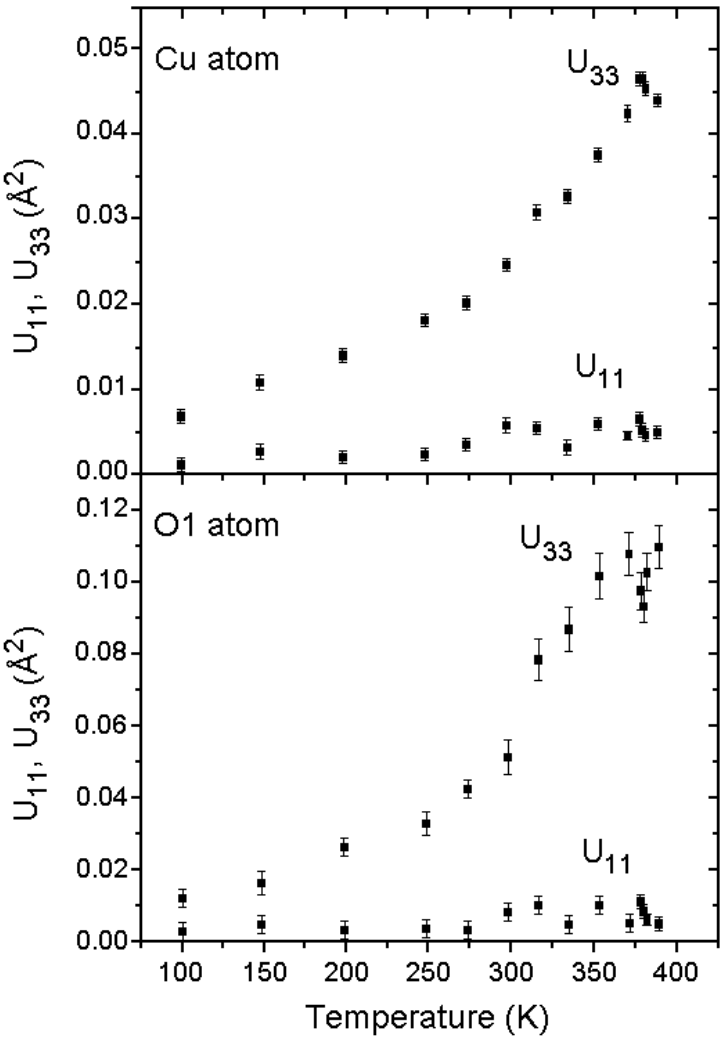

Figure 3.25: Temperature dependence of the components U_{11} and U_{33} of the thermal tensors for the Cu and O1 atoms, from 100 K up to 395 K.

3.4.3 Results from differential scanning calorimetry

• The Differential Scanning Calorimetry (DSC) is a technique used to measure the heat absorbed by a sample when it undergoes a phase transition. It can be used to determine the specific heat of the material, the transition temperature and the enthalpy change during the transition.

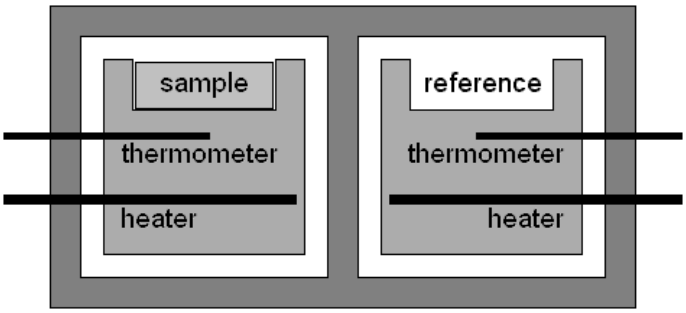

Figure 3.26: Schematic description of a DSC apparatus.

The experimental procedure is described as follows: A thermally isolated box contains two identical recipients, one holding the sample and the other one being used as a reference (Fig. 3.26). Both recipients are heated continuously so that they always have the same temperature, even during thermal events (phase transitions) within the sample. Hence, comparing the rates of heat flow for both recipients, one can detect any thermal effect occuring in the sample at a phase transition. For example, an endothermic or exothermic transition (e.g. melting and freezing) will give rise to a peak, whose area is proportional to the total enthalpy change, and a transition with a change in the specific heat (e.g. glass transitions in polymers) will create a discontinuity in the graph (Fig. 3.27).

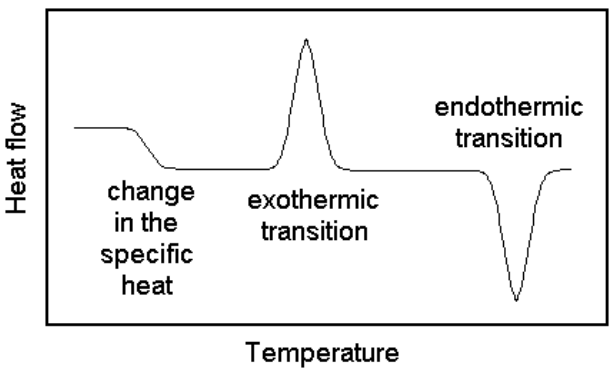

Figure 3.27: Schematic behaviour of a sample undergoing a phase transition with a change in the specific heat, an exothermic and an endothermic phase transition.

• The differential scanning calorimetry measurement on $SrCu_2(BO_3)_2$ was performed by Dr. H. Kageyama[10] [37], on a Mac Science DSC3200S analyzer in the 280 - 467 K temperature region in air at the warming or/and cooling rate of 10 K/min. Approximately 20 mg of finely ground sample was placed in an aluminum capsule. Calcined α - Al_2O_3 was used as internal reference standard in air.

The experiment confirms that the phase transition at 395 K is a second order one (Fig. 3.28): No obvious latent heat is associated with the transition. Instead, the thermal effect of the transition is smeared out over an appreciable temperature range, as expected for a second order phase transition.

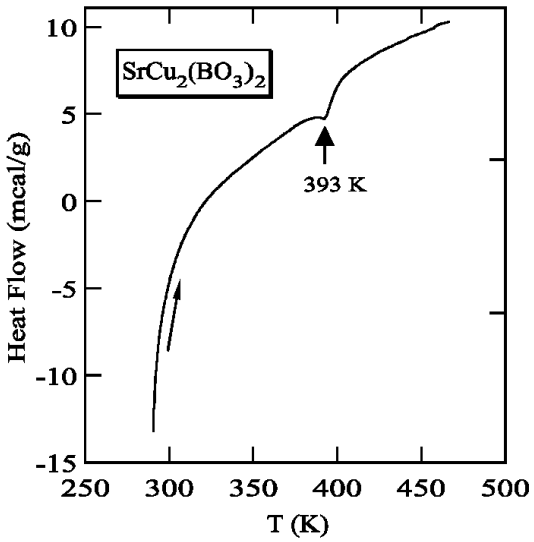

Figure 3.28: DSC-measurement of $SrCu_2(BO_3)_2$ upon heating (Fig. 5 from [37]).

3.5 Structure of $SrCu_2(BO_3)_2$ above 395 K

3.5.1 Determination of the structure

Above $T_s = 395$ K, the new reflection conditions are compatible with three space groups: the two non-centrosymmetric space groups $I\bar{4}c2$ (No. 120), $I4cm$ (No. 108) and the centrosymmetric one $I4/mcm$ (No. 140).

In order to solve the high temperature (HT) structure, a measurement was performed on the Stoe-IPDS-I diffractometer at 590 K, high above T_s, with the conditions given in table 3.20. The cell parameters at 590 K are $a = 9.004\,(2)$ Å, $c = 6.706\,(2)$ Å.

[10] Institute for Solid State Physics, Tokyo, Japan

There was no problem in solving the structure in the three possible space groups by means of direct methods (program SIR97 [48]).
The internal R - values of the data set before and after numerical absorption correction (Laue group $4/mmm$) are 11.44 % and 3.11 %, respectively. The obtained R - values at the end of the refinements for each space group show that the three models have comparable qualities (see below).

U (kV)	I (mA)	φ - range (°)	$\Delta\varphi$ (°)	d (mm)	2θ - range (°)	t (mn)
50	20	70 - 300	2	80	2.9 - 48.4	3

Table 3.20: Conditions of the measurement at 590 K with the Stoe-IPDS-I diffractometer.

Figure 3.29 shows the relationships between these space groups. $I422$, $I4/m$, $I4cm$, $I\bar{4}2m$ and $I\bar{4}c2$ (order 16) are all subgroups of $I4/mcm$ (order 32).

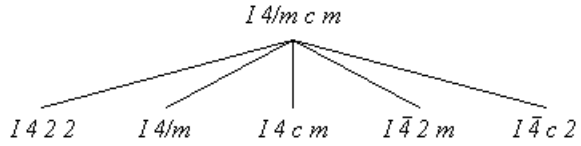

Figure 3.29: Maximal non-isomorphic tetragonal subgroups of type I of $I4/mcm$ [2]. $I\bar{4}2m$ is the space group of the room temperature structure.

It should be noted here that, for a second order phase transition, according to the Landau theory, a group - subgroup relationship between the high - and low - temperature space groups is a prerequisite.

- Solution in the space group $I\bar{4}c2$

The results are given in tables 3.21 and 3.22. The obtained R - values for the 24 parameters are R1 = 1.48 % for 218 unique reflections with F_{obs} ¿ 4 $\sigma_{F_{obs}}$, R1 = 1.56 % for all 221 data, wR2 = 3.26 %, and the goodness of fit GooF = 2.86.
However, in this model, the planarity of the $Cu_2(BO_3)_2$ - layers in the HT phase, suggested by the continuous movement of the atoms at low temperatures, is broken by the O2 atom (Tab. 3.21, Fig. 3.30). Also, the z position of the O2 atom is very far away from $\frac{1}{4}$, with a standard deviation much larger than in the other models (Tab. 3.23 and 3.25). It is often observed that the refinement in a wrong space group of the positions of atoms that should be on a special position leads to values significantly different than the real ones, while the standard deviations are very large.

Atom	Multiplicity	x	y	z	Site symmetry
Sr	4	0	$\frac{1}{2}$	0	2.22
Cu	8	0.11392 (4)	0.11392 (4)	$\frac{1}{4}$	..2
B	8	0.2947 (4)	0.2947 (4)	$\frac{1}{4}$	..2
O1	8	0.4018 (3)	0.4018 (3)	$\frac{1}{4}$	..2
O2	16	0.3266 (3)	0.1466 (3)	0.261 (2)	1

Table 3.21: $SrCu_2(BO_3)_2$ at 590 K, space group $I\bar{4}c2$: atomic coordinates.

Atom	U_{11} (Å^2)	U_{22} (Å^2)	U_{33} (Å^2)	U_{12} (Å^2)	U_{13} (Å^2)	U_{23} (Å^2)
Sr	0.0163 (3)	0.0163 (3)	0.0183 (4)	0 (n.s.)	0	0
Cu	0.0089 (3)	0.0089 (3)	0.0600 (6)	-0.0014 (2)	0.006 (1)	-0.006 (1)
B	0.016 (1)	non positive definite if anisotropic				
O1	0.008 (1)	0.008 (1)	0.128 (4)	0 (n.s.)	0 (n.s.)	0(n.s.)
O2	0.013 (1)	0.009 (1)	0.038 (3)	-0.0011 (8)	-0.014 (5)	0.007 (4)

Table 3.22: $SrCu_2(BO_3)_2$ at 590 K, space group $I\bar{4}c2$: thermal displacement parameters.

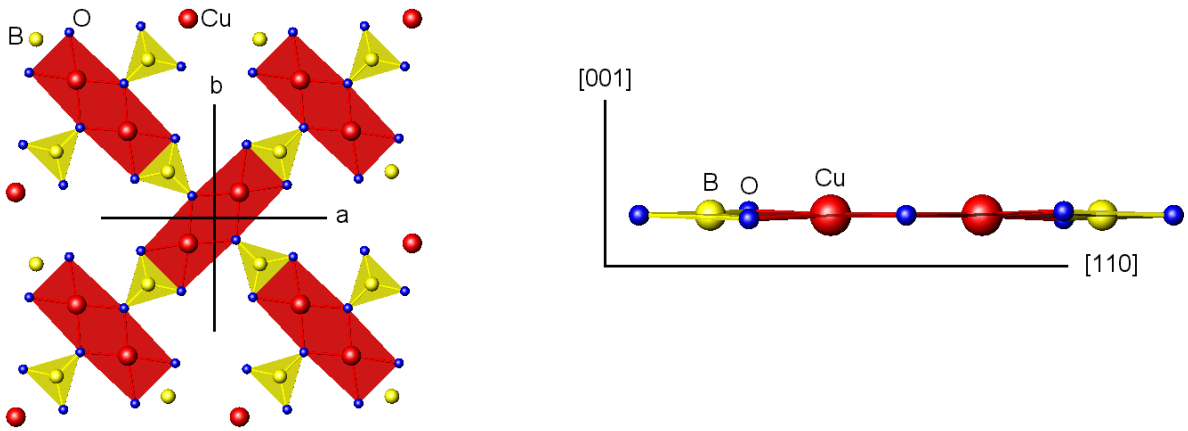

Figure 3.30: $SrCu_2(BO_3)_2$ at 590 K, space group $I\bar{4}c2$. Left: projection of a $Cu_2(BO_3)_2$ - layer in the (**a**, **b**) plane. Right: View of a plaquette with the c axis vertical.

- Solution in the space group $I4cm$

The results are given in tables 3.23 and 3.24. The obtained R - values for the 27 parameters are R1 = 1.51 % for 237 unique reflections with F_{obs} ¿ 4 $\sigma_{F_{obs}}$, R1 = 1.65 % for all 241 data, wR2 = 3.28 %, and the goodness of fit GooF = 2.97.
In this model, the $Cu_2(BO_3)_2$ - layers are definitely not flat. More disturbing is the extreme distortion of the BO_3 group from the ideal triangular planar shape (Fig. 3.31): the B atom lies far away from the plane defined by the oxygen atoms.

Atom	Multiplicity	x	y	z	Site symmetry
Sr	4	0	0	0	4..
Cu	8	0.38606 (4)	0.11394 (4)	0.254 (1)	..m
B	8	0.2054 (4)	0.2946 (4)	0.271 (2)	..m
O1	8	0.5981 (3)	0.0981 (3)	0.258 (5)	..m
O2	16	0.1735 (3)	0.1465 (3)	0.238 (3)	1

Table 3.23: $SrCu_2(BO_3)_2$ at 590 K, space group $I4cm$: atomic coordinates. The Sr atom was fixed to the position $z = 0$.

Atom	U_{11} (Å^2)	U_{22} (Å^2)	U_{33} (Å^2)	U_{12} (Å^2)	U_{13} (Å^2)	U_{23} (Å^2)
Sr	0.0156 (3)	0.0156 (3)	0.0189 (4)	0	0	0
Cu	0.0085 (3)	0.0085 (3)	0.0589 (5)	0.0014 (2)	0 (n.s.)	0 (n.s.)
B	0.011 (2)	non positive definite if anisotropic				
O1	0.009 (1)	0.009 (1)	0.131 (6)	0 (n.s.)	0.017 (7)	0.017 (7)
O2	0.011 (1)	0.010 (1)	0.036 (4)	0.0013 (9)	-0.007 (4)	-0.004 (3)

Table 3.24: $SrCu_2(BO_3)_2$ at 590 K, space group $I4cm$: thermal displacement parameters.

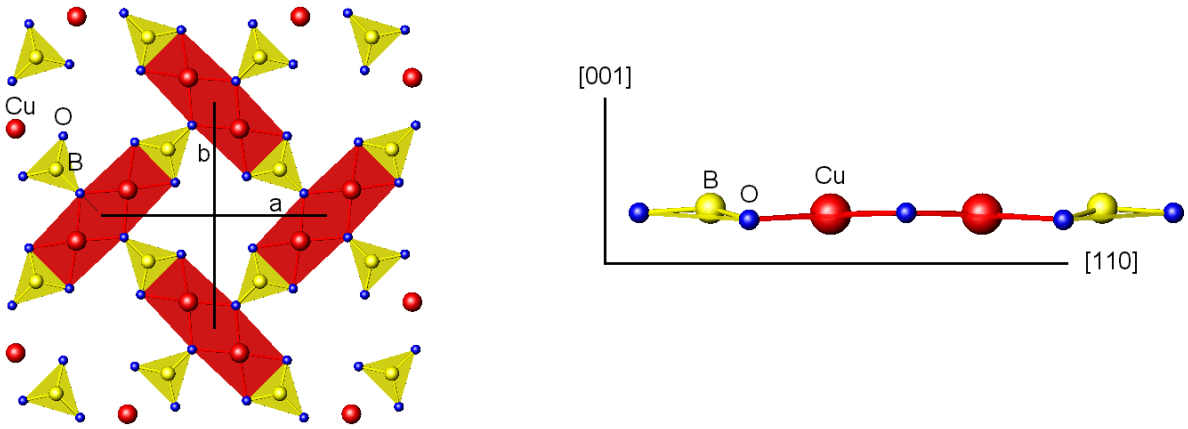

Figure 3.31: $SrCu_2(BO_3)_2$ at 590 K, space group $I4cm$. Left: projection of a $Cu_2(BO_3)_2$-layer in the (**a**, **b**) plane. Right: View of a plaquette with the c axis vertical.

- Solution in the space group $I4/mcm$

The results are given in tables 3.25 and 3.26. The obtained R-values for the 18 parameters are R1 = 1.48 % for 132 unique reflections with F_{obs} ¿ 4 $\sigma_{F_{obs}}$, R1 = 1.52 % for all 135 data, wR2 = 3.48 %, and the goodness of fit GooF = 3.83.
The BO_3 and CuO_4 groups are perfectly planar in this model (Tab. 3.25, Fig. 3.32), in agreement with the temperature dependence of the z coordinates of the atoms in the low

temperature phase. Moreover, the space group $I4/mcm$ is a minimal non-isomorphic supergroup of $I\bar{4}2m$.

Atom	Multiplicity	x	y	z	Site symmetry
Sr	4	0	0	$\frac{1}{4}$	422
Cu	8	0.11391 (6)	0.38609 (6)	0	$m.2m$
B	8	0.2947 (5)	0.2053 (5)	0	$m.2m$
O1	8	0.4020 (4)	0.0980 (4)	0	$m.2m$
O2	16	0.3271 (3)	0.3537 (3)	0	$m..$

Table 3.25: $SrCu_2(BO_3)_2$ at 590 K, space group $I4/mcm$: atomic coordinates.

Atom	U_{11} (Å^2)	U_{22} (Å^2)	U_{33} (Å^2)	U_{12} (Å^2)	U_{13} (Å^2)	U_{23} (Å^2)
Sr	0.0163 (4)	0.0163 (4)	0.0183 (5)	0	0	0
Cu	0.0090 (3)	0.0090 (3)	0.0590 (7)	0.0012 (3)	0	0
B	0.017 (2)	non positive definite if anisotropic				
O1	0.009 (2)	0.009 (2)	0.131 (6)	0 (n.s.)	0	0
O2	0.011 (2)	0.010 (2)	0.042 (2)	0 (n.s.)	0	0

Table 3.26: $SrCu_2(BO_3)_2$ at 590 K, space group $I4/mcm$: thermal displacement parameters.

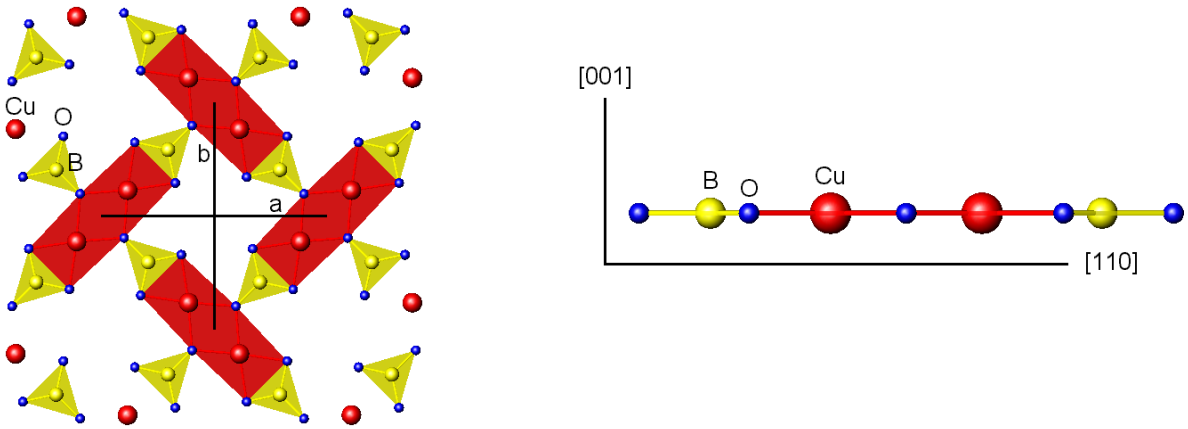

Figure 3.32: $SrCu_2(BO_3)_2$ at 590 K, space group $I4/mcm$. Left: projection of a $Cu_2(BO_3)_2$-layer in the (**a**, **b**) plane. Right: View of a plaquette with the c axis vertical.

From the refinements of the structure in the three possible space groups, we found no evidence that a non-centrosymmetric model should be used instead of the centrosymmetric one. Therefore, we chose the solution in the space group $I4/mcm$ for the HT structure model.

3.5.2 Discussion of the solution

The solution of the structure of $SrCu_2(BO_3)_2$ in the space group $I4/mcm$ is coherent with the temperature dependence of the internal parameters in the LT phase. Moreover, a direct group-subgroup relationship is consistent with a 2^{nd} order phase transition. Below T_s and with increasing temperatures, in the space group $I\bar{4}2m$, the atoms Cu, B, O1 and O2 of a $Cu_2(BO_3)_2$ - layer move continuously towards the plane $z = \frac{1}{4}$, which becomes a glide plane situated at $z = 0$ in the standard setting of the space group $I4/mcm$. This also explains that, above T_s, the intensity of the (004) reflection doesn't increase any more (Fig. 3.22): the atoms are locked at $z = 0$ in the HT space group ($z = \frac{1}{4}$ in the LT space group), and the intensity of this reflection decreases because of increasing thermal displacement parameters.
The atoms Cu and O1 still have strongly anisotropic thermal ellipsoids in the HT phase, but the anisotropy doesn't increase so much with the temperature above T_s (Fig. 3.33).

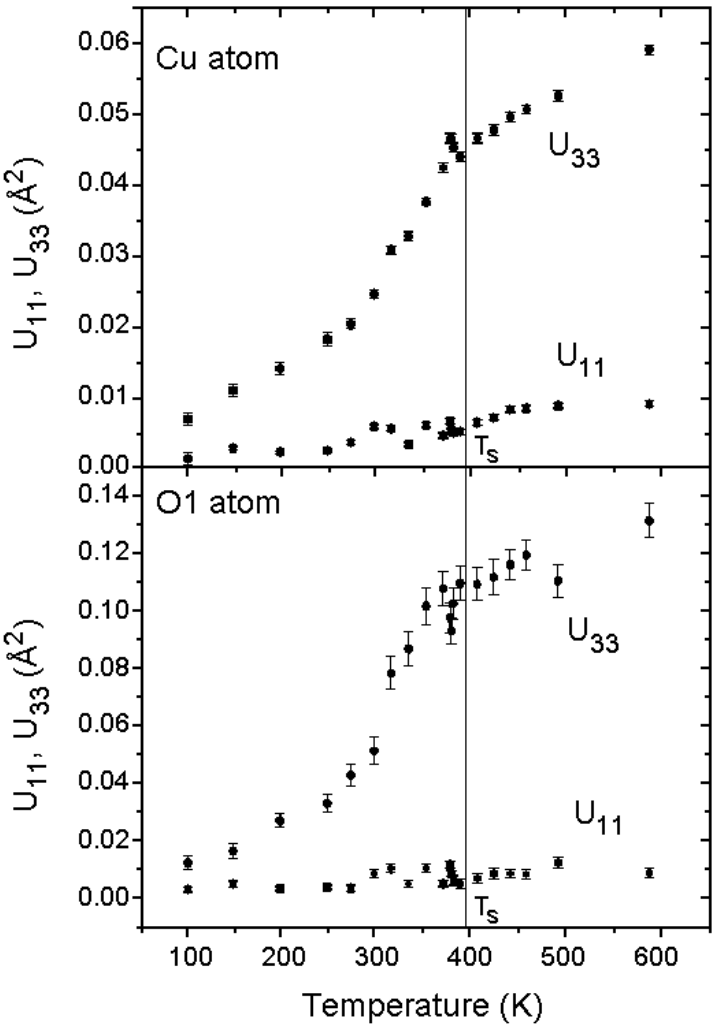

Figure 3.33: Temperature dependence of the components U_{11} and U_{33} of the thermal tensors for the Cu and O1 atoms, from 100 K up to 590 K.

3.5.3 Neutron diffraction experiment at 408 K

We used the same single crystal as for the room temperature neutron diffraction experiment. The idea was to look for anharmonicity in the crystal, in order to explain the strong thermal expansion coefficient observed for the c axis (see section 3.5.4).

The measurement was performed on the 5C2 four-circle diffractometer at the LLB [11]. The wavelength of the neutrons was set to 0.8375 Å. A cylindrical Vanadium furnace was used, similar to the one described in [49]. We measured the intensities of reflections in the range $2° < 2\theta < 90°$ at 408 K. The obtained cell parameters are $a = 9.00\,(1)$ Å, $c = 6.65\,(1)$ Å for the tetragonal cell, space group $I4/mcm$.

The internal R-value of the data set is 11.02 %. This high value doesn't come from any absorption of neutrons by the crystal, since the internal R - value of the room temperature data set was extremely good. A careful investigation of the reflection profiles revealed a non regular and quite high background, which must be coming from the furnace we used for the measurement.
An isotropic type II distribution was used for the secondary extinction, and the structure was refined using the program JANA2000 [32]. The R - values for the 21 parameters are R1 = 12.05 % for all the 1369 data, wR2 = 7.42 %, and the goodness of fit GooF = 1.46. Tables 3.27 and 3.28 give the results of the refinement for the harmonic model, in order to compare with the X-ray data.

Atom	Multiplicity	x	y	z	Site symmetry
Sr	4	0	0	$\frac{1}{4}$	422
Cu	8	0.1140 (1)	0.3860 (1)	0	$m.2m$
B	8	0.2951 (1)	0.2049 (1)	0	$m.2m$
O1	8	0.4021 (2)	0.0979 (1)	0	$m.2m$
O2	16	0.3269 (1)	0.3545 (1)	0	$m..$

Table 3.27: $SrCu_2(BO_3)_2$ at 408 K (neutrons): atomic coordinates.

Atom	U_{11} (Å^2)	U_{22} (Å^2)	U_{33} (Å^2)	U_{12} (Å^2)	U_{13} (Å^2)	U_{23} (Å^2)
Sr	0.0089 (5)	0.0089 (5)	0.0057 (9)	0	0	0
Cu	0.0038 (4)	0.0038 (4)	0.040 (1)	0.0008 (4)	0	0
B	0.0044 (4)	0.0044 (4)	0.0155 (8)	0.0008 (4)	0	0
O1	0.0041 (5)	0.0041 (5)	0.092 (3)	0.0009 (6)	0	0
O2	0.0056 (5)	0.0046 (5)	0.0208 (7)	0 (n.s.)	0	0

Table 3.28: $SrCu_2(BO_3)_2$ at 408 K (neutrons): thermal displacement parameters.

[11] Laboratoire commun CEA - CNRS

The difference Fourier maps calculated at the end of the refinement were quite noisy and no strong peak was observed around the atoms. Attempts to refine anharmonic thermal displacement parameters failed.

3.5.4 Temperature dependence of the cell parameters

We have measured 25 X-ray powder diffraction patterns, from room temperature up to 473 K, with the Siemens D500 diffractometer. Silicon was used as an internal standard in the weight ratio 1:1 in order to improve the accuracy on the cell parameters, which were refined with the program FULLPROF (Fig. 3.35 and 3.36, page 55).

Figure 3.34 shows the temperature dependence of the cell parameters a and c, the unit cell volume V as a function of temperature is shown in figure 3.37. The absence of a discontinuity in these quantities at the phase transition also supports the second order character of the phase transition. In fact, only their derivatives are discontinuous at T_s, and the change in the derivative of V through the phase transition is very small.

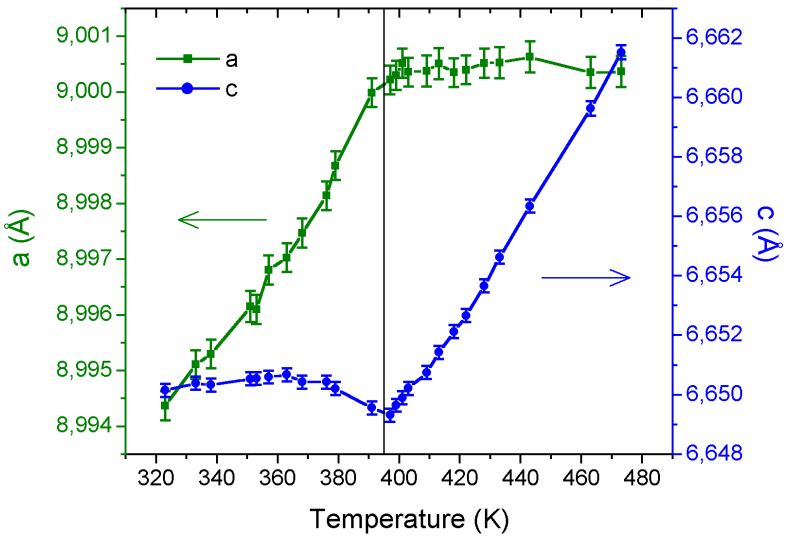

Figure 3.34: Temperature dependence of the cell parameters of $SrCu_2(BO_3)_2$.

The temperature dependence of the cell parameters exhibits unusual features.
Above T_s, a and c increase linearly with the temperature because of the linear thermal expansion, coming from the anharmonicity of the thermal vibrations of the atoms. The strong elongation of these ellipsoids along c seems to indicate an important anharmonic behavior of the atoms, which gives rise to a large expansion coefficient in this direction. In the (**a**, **b**) plane, the thermal displacement parameters are much smaller, so that the thermal expansion in the a direction is almost zero above T_s.

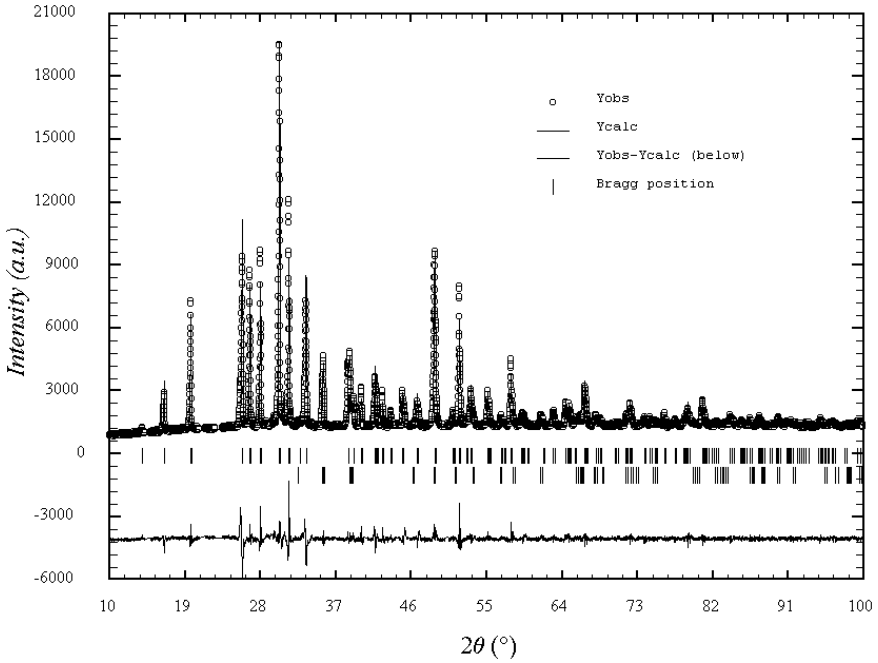

Figure 3.35: Room temperature powder diagram of $SrCu_2(BO_3)_2$. The difference between the observed and calculated intensities is displayed at the bottom of the graph. The first line of Bragg peaks is for $SrCu_2(BO_3)_2$, the second one for the internal standard Si.

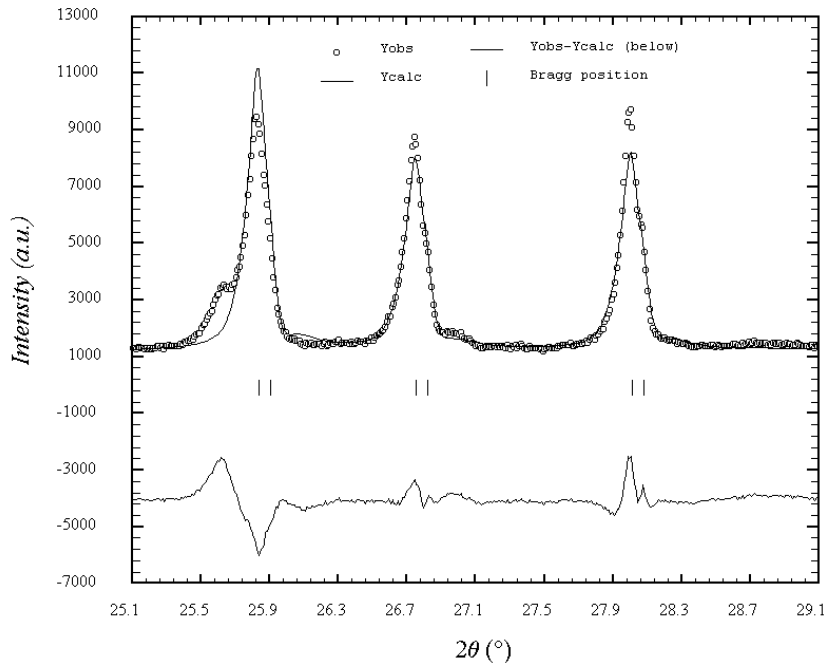

Figure 3.36: Room temperature powder diagram of $SrCu_2(BO_3)_2$ for $25.1\,° < 2\theta < 29.1\,°$. Most of the features in the difference between calculated and observed intensities come either from impurity phases in the sample or from the asymmetry of the reflection profiles.

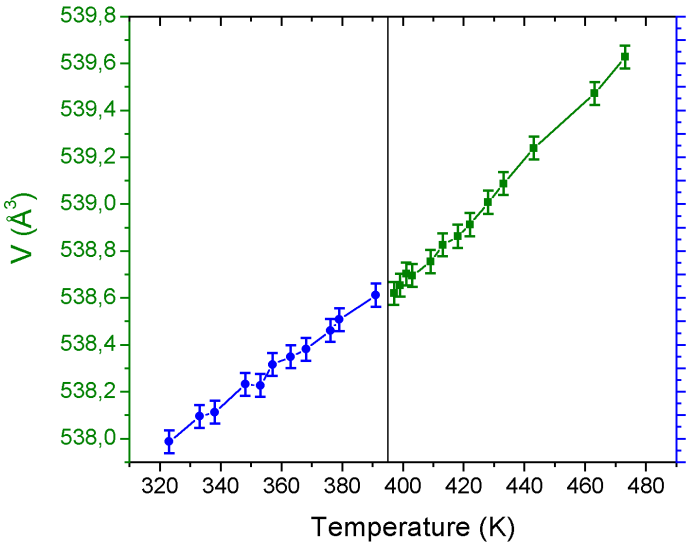

Figure 3.37: Temperature dependence of the unit cell volume of $SrCu_2(BO_3)_2$.

In the LT phase, the temperature dependence of a and c is completely different. The a parameter increases with the temperature, while c remains almost constant but exhibits a local maximum at about 363 K. In fact, this originates from the decrease of the corrugation of the $Cu_2(BO_3)_2$ - layers as the temperature increases. Since the layers become flatter when approaching T_s, they extend in the (**a**, **b**) plane to keep the bond lengths constant: this critical effect added to the linear thermal expansion makes a increase strongly in a non-linear way. Also, as the $Cu_2(BO_3)_2$ - layers become flatter, they need less space along c: this creates a negative term which competes with the linear thermal expansion. This negative term, with its critical behaviour, becomes larger and larger with increasing temperature, and eventually overcomes the linear thermal expansion term at 365 K. The c parameter then decreases until T_s is reached.

3.5.5 Magnetic susceptibility in the vicinity of T_s

Figure 3.38 displays the same measurement as in figure 3.2, but the magnetic susceptibility close to the phase transition at T_s=395 K has been displayed in a separate inset.

The phase transition is accompanied by a small increase in the magnetic susceptibility. This indicates that the magnetic interactions between the Cu^{2+} ions change at T_s. However, the Cu - Cu distances within a $Cu_2(BO_3)_2$ - layer are quasi independent of the temperature. We then have to investigate the interlayer Cu - Cu distances in order to explain the behavior of the magnetic susceptibility at T_s.
Figure 3.39 shows, at 100 K, the shortest intra - and inter - layer Cu - Cu distances. As mentioned before, there are two different shortest interlayer Cu - Cu distances to take

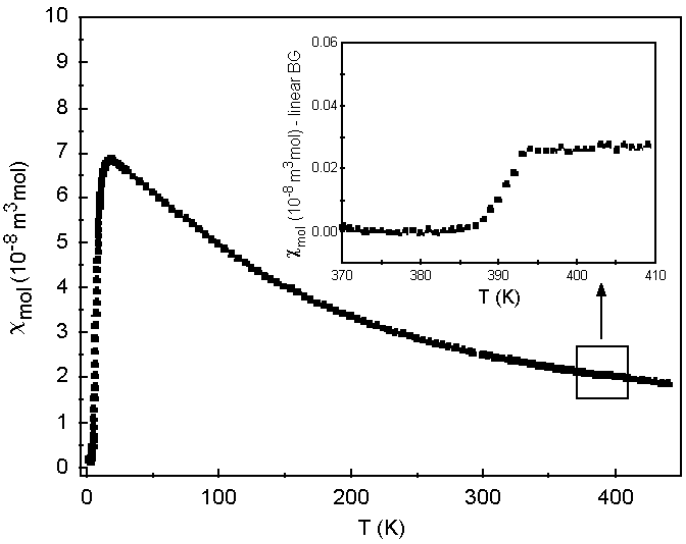

Figure 3.38: Temperature dependence of the magnetic susceptibility of $SrCu_2(BO_3)_2$. The inset shows the susceptibility around T_s (Fig. 4 from [37]).

into account: 3.48 Å, 4.35 Å. Figure 3.40 plots the temperature dependence of those two distances. As the temperature increases, the two interlayer Cu - Cu distances approach each other, and they are equal at T_s and above.

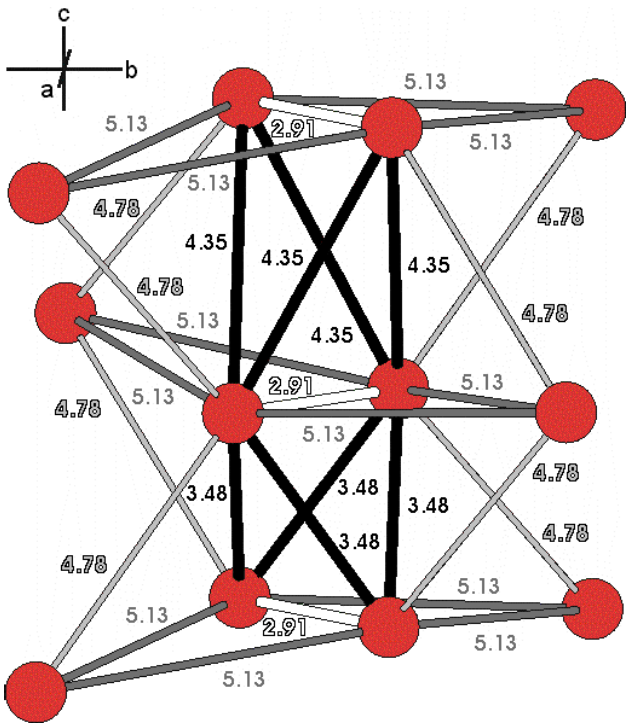

Figure 3.39: $SrCu_2(BO_3)_2$ at 100 K: shortest Cu - Cu distances (in Å).

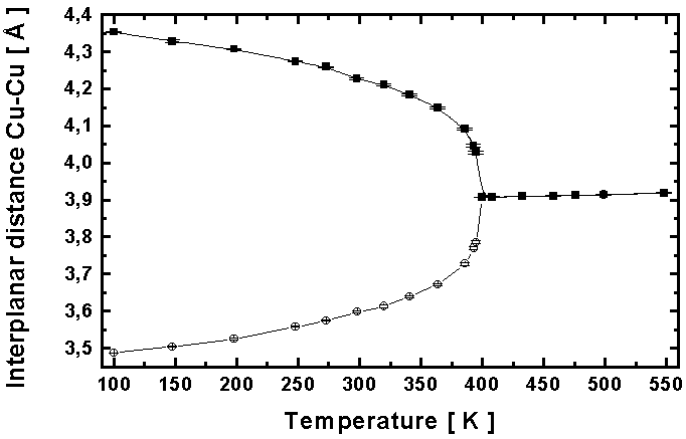

Figure 3.40: Shortest interlayer Cu - Cu distances as a function of temperature.

The anomaly of the magnetic susceptibility around T_s is the evidence for a weak but significant magnetic interaction between the $Cu_2(BO_3)_2$ - layers. This is in contrast to the large majority of theoretical papers, in which $SrCu_2(BO_3)_2$ has been treated as a purely two-dimensional system. In fact, the effects of an interlayer coupling J'' had been theoretically discussed in [50]. The magnetic susceptibility of $SrCu_2(BO_3)_2$ was fitted and the coupling constants were found to be $J = 85\,\mathrm{K}$ (intradimer coupling), $J' = 54\,\mathrm{K}$ (interdimer but intralayer coupling) and $J'' = 8\,\mathrm{K}$ (interlayer coupling). Thus, the ground state for $SrCu_2(BO_3)_2$ is still the exact dimer ground state, very close to the phase boundaries to an antiferromagnetically ordered state as well as a plaquette singlet ground state. Figure 3.41 shows the phase diagram at 0 K of the three dimensional orthogonal dimer model.

The disordered exact dimer ground state and ordered antiferromagnetic Néel state occupy a large part of the phase diagram.
For very small values of $\frac{J''}{J}$, there exists a disordered plaquette singlet ground state, as in the two-dimensional Shastry-Sutherland model (but it was not mentionned in [34]), in which the spins $\frac{1}{2}$ are distributed over plaquettes. Figure 3.42 shows the organization of the plaquettes (in black) within the two-dimensional spin system, based on the structure of a $Cu_2(BO_3)_2$ - layer that is topologically equivalent to the Shastry-Sutherland model. Figure 3.43 is the projection of such a layer onto the (**a**, **b**) plane, in order to compare the arrangement of the plaquettes with the crystallographic structure of $SrCu_2(BO_3)_2$.
For small values of the interdimer interactions J' and high interlayer interactions J'', a Haldane state appears, formed by chains of orthogonal dimers along c (Fig. 3.44). Since the dimers can be either in the ground state $S = 0$ or in the first excited state $S = 1$, they are considered as bosons. A chain of antiferromagnetically coupled bosons is called a Haldane chain, whose properties were discussed in [51].

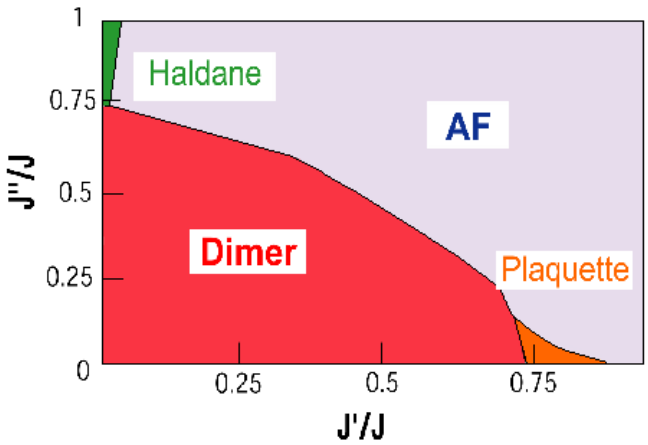

Figure 3.41: Schematic magnetic phase diagram at 0 K of the three dimensional orthogonal dimer model [52].

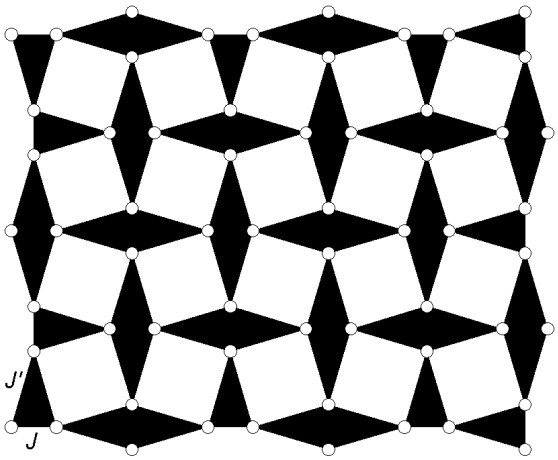

Figure 3.42: The plaquette ground state. The spins $\frac{1}{2}$ are symbolized by the empty circles. The plaquettes are represented by the black rhombs.

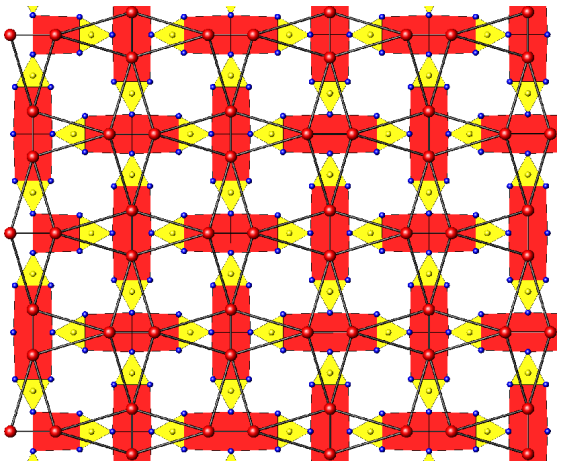

Figure 3.43: Projection of a $Cu_2(BO_3)_2$-layer onto the (**a**, **b**) plane. The thick bonds represent the next and second next nearest neighbors antiferromagnetic interactions.

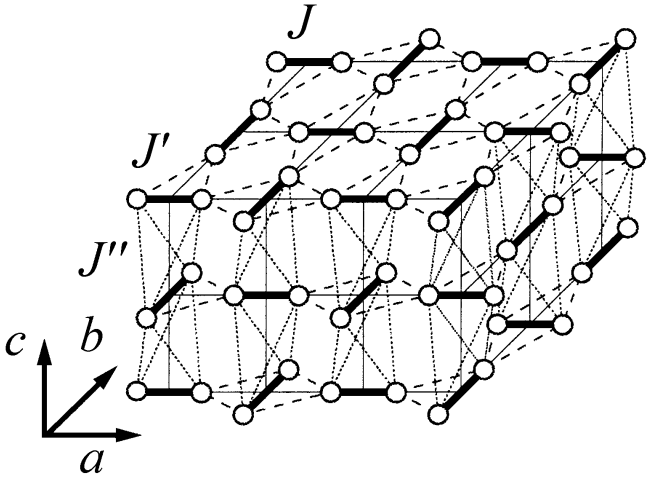

Figure 3.44: Structure of $SrCu_2(BO_3)_2$ and antiferromagnetic interactions (Fig.3 from [53]). In the case of small J' and for $\frac{J''}{J} > 0.7$, the orthogonally aligned dimers along the c axis build Haldane chains.

3.6 Study of Ba- and Ca- substituted $SrCu_2(BO_3)_2$

The boudaries between the different magnetic states in the phase diagram of figure 3.41 are pressure dependant. Since $SrCu_2(BO_3)_2$ is very close to the phase transition between the exact dimer ground state and the disordered plaquette and ordered Néel (AF) ground states, it was tempting to study the effects of pressure on the structure of the material. A way to achieve this is to replace the Sr atoms by other alkaline earth metals like Ca or Ba and, thereby, exert "chemical pressure" onto the $Cu_2(BO_3)_2$ - layers.

The structure and magnetic properties of $Sr_{1-x}M_xCu_2(BO_3)_2$, with M = Ba or Ca ($0 \leq x \leq 0.4$), had already been studied in [46, 47, 35], especially the compositions $Sr_{0.735}Ba_{0.265}Cu_2(BO_3)_2$ and $Sr_{0.661}Ba_{0.339}Cu_2(BO_3)_2$. It was not possible to grow single crystals with $x > 0.4$.
These phases are isostructural to $SrCu_2(BO_3)_2$. A significant effect of the substitution of Sr atoms by Ca or Ba on the interlayer separation was observed.

All the samples studied in [35] showed an exact dimer ground state and a spin gap at low temperatures.
It was found that the pressure applied to the layers by means of chemical substitution essentially affects the structure along the c direction, and the ratio J'/J of the magnetic interactions between nearest neighbors and second nearest neighbors within the layers hardly changes. However, the plateaux in the magnetisation curves seem to disappear with increasing Ba and Ca contents (Fig. 3.45).

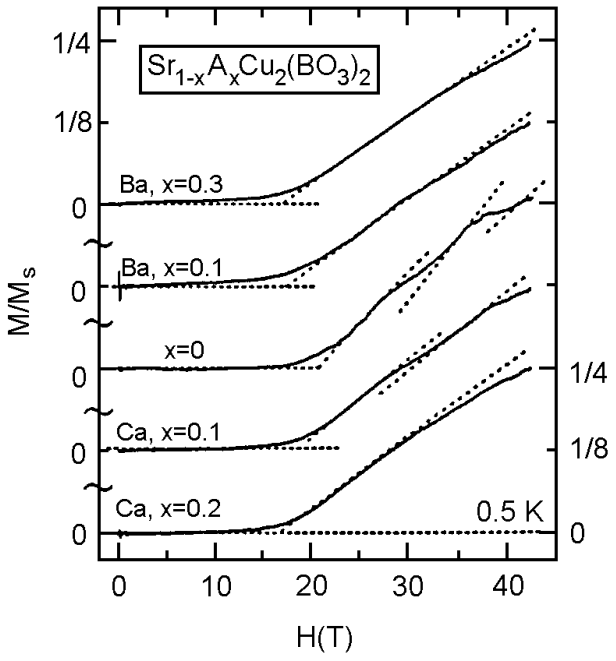

Figure 3.45: Disappearance of the plateaux in the magnetization curves with increasing Ca/Ba substitution for Sr (Fig. 5 from [35]).

By means of X-ray powder diffraction, we studied the effect of the substitution of the Sr atoms by Ba and Ca on the room temperature cell parameters and the temperature of the structural phase transition at high temperatures. Figures 3.46 and 3.47 show our results, together with the ones obtained by Dr. H. Kageyama [12]. The compositions of our Ba - doped samples were confirmed by comparisons with the cell parameters of single crystals. The Ca - doped powder sample we synthesized contained more impurities (CuO, $SrCO_3$, $CaCO_3$), and no single crystal was available to compare the cell parameters, so that the actual composition of our $Sr_{1-x}Ca_xCu_2(BO_3)_2$ samples is not determined independently. For the present purpose, we have used the nominal Ca - content instead.

As expected, the cell parameters decrease while incorporating Ca atoms and increase with the Ba content, due to the different values of the ionic radii: $r(Ca^{2+}) < r(Sr^{2+}) < r(Ba^{2+})$. Because of the layered structure, the effects of the substitution are mostly seen on the c lattice parameter. In spite of the fact that our powder samples were not strictly single phase, the agreement between our results and those of Kageyama is quite good.

To determine the temperature T_s of the phase transition in the doped compounds, the temperature dependence of the (101) reflection in the X-ray powder diffraction diagrams was studied, since this reflection vanishes at the phase transition. We observed almost no influence of the substitution on T_s, while the results from Dr. Kageyama show that T_s increases slightly with the Ba content and decreases with the Ca content (Fig. 3.47).

A priori, this behaviour would be more consistent with the cell parameters: the substitution of Sr by Ba atoms leads to larger interlayer distances, the layers can occupy more space and should be more corrugated, so that the phase transition should occur at higher temperatures, if the critical exponent of the transition doesn't change with the substitution. On the other hand, the substitution with Ca atoms should lead to a lower T_s. However, it is seen from our single crystal diffraction experiments on $Sr_{1-x}Ba_xCu_2(BO_3)_2$ that the corrugation of the $Cu_2(BO_3)_2$ - layers is maximum for $x = 0$ (see below).

An X-ray diffraction experiment was performed on a $(0.17 \times 0.14 \times 0.12)$ single crystal of $Sr_{0.9}Ba_{0.1}Cu_2(BO_3)_2$ at room temperature, with the conditions given in table 3.29. The internal R - values of the data set before and after absorption correction are 7.72 % and 4.67 %, respectively. Tables 3.30 and 3.31 give the results of the refinements. The obtained R - values for the 35 parameters are R1 = 1.90 % for 335 unique reflections with F_{obs} ¿ 4 $\sigma_{F_{obs}}$, R1 = 2.20 % for all 363 data, wR2 = 3.17 %, and the goodness of fit

[12] Institute for Solid State Physics, Tokyo, Japan

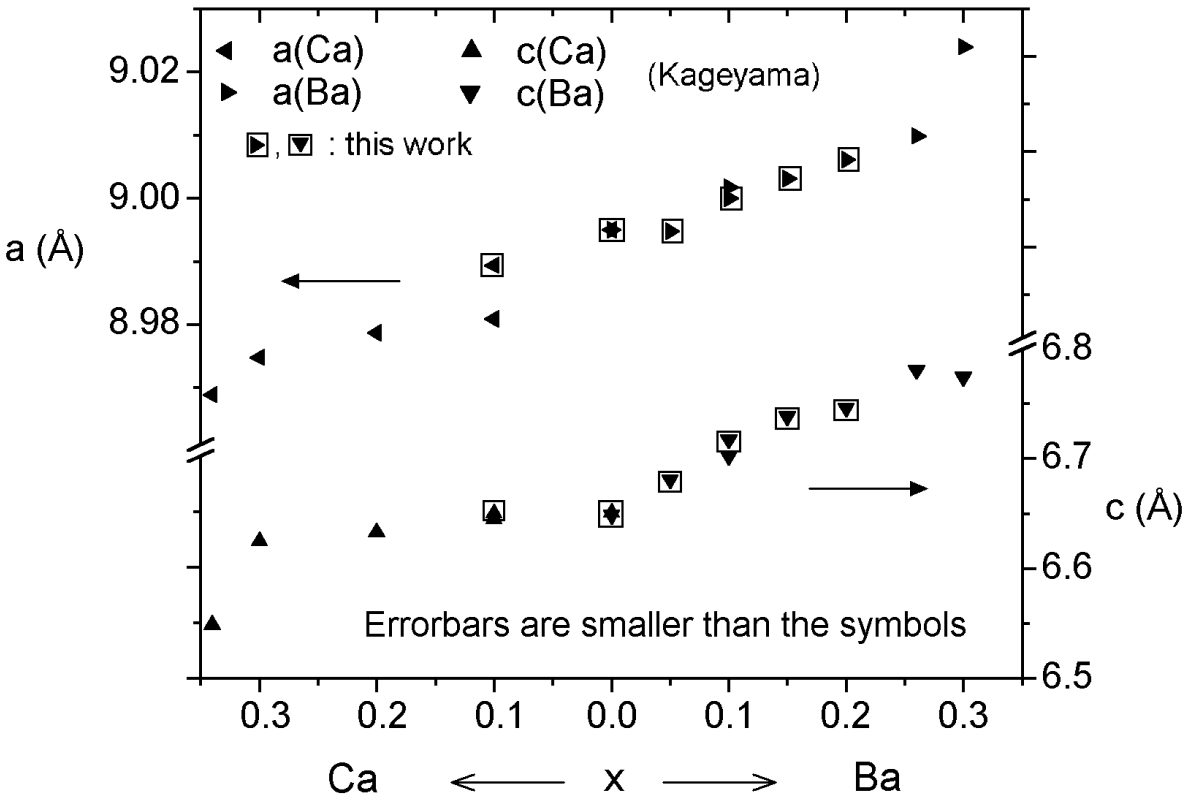

Figure 3.46: Evolution of the cell parameters with the Ca/Ba substitution for Sr.

GooF = 1.70. The Ba content x was refined to the value 0.11 (1).

U (kV)	I (mA)	φ - range (°)	$\Delta\varphi$ (°)	d (mm)	2θ - range (°)	t (mn)
50	20	50 - 290	1.5	60	3.8 - 55.9	2

Table 3.29: Conditions of the measurement of $Sr_{0.9}Ba_{0.1}Cu_2(BO_3)_2$ at room temperature with the Stoe-IPDS-I diffractometer.

From table 3.30, the calculated maximum distance between the atoms of a $Cu_2(BO_3)_2$ - layer and the plane $z = \frac{1}{4}$ is 0.248 (7) Å for the O1 atom. For the pure $SrCu_2(BO_3)_2$, this distance is 0.267 (4) Å, which shows that the corrugation of the layers significantly decreases when introducing Ba atoms in the structure. This can be explained by the fact that the Ba^{2+} ions have a larger radius than the Sr^{2+} ions, so that a higher pressure is applied on the layers, even though the c parameter is larger.
Thus, the substitution of the Sr atoms by Ba atoms leads to less corrugated $Cu_2(BO_3)_2$ - layers and almost unchanged temperatures T_s for the phase transition.
Moreover, the local occupancy disorder (either Sr or Ba/Ca) could drastically affect the interplane magnetic interactions and be the origin of the disapearance of the plateaux

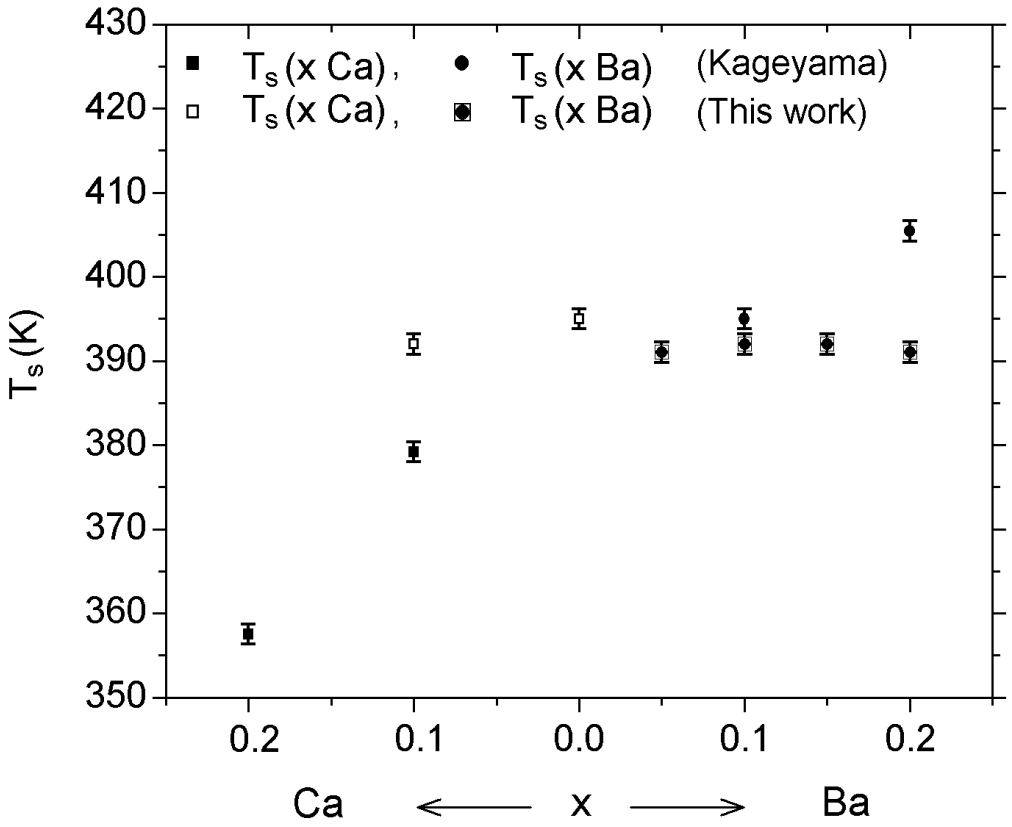

Figure 3.47: Evolution of T_s with the Ca/Ba substitution for Sr.

Space group		a (Å)	c (Å)	V (Å^3)	Z
$I\bar{4}2m$		9.022 (2)	6.713 (2)	546.3 (3)	4
Atom	Multiplicity	x	y	z	Site symmetry
Sr, Ba	4	0	$\frac{1}{2}$	0	222
Cu	8	0.1143 (1)	0.1143 (1)	0.2776 (2)	..m
B	8	0.2944 (4)	0.2944 (4)	0.241 (1)	..m
O1	8	0.4010 (3)	0.4010 (3)	0.213 (1)	..m
O2	16	0.3270 (2)	0.1461 (2)	0.2558 (9)	1

Table 3.30: Room temperature structure of $Sr_{0.9}Ba_{0.1}Cu_2(BO_3)_2$: atomic coordinates.

in the magnetization curves: The plateaux are the result of the creation of magnetic superstructures in order to minimize the energy of the system, under the condition that all the Cu^{2+} ions are equivalent. The presence of a local occupancy disorder would create different crystallographic sites for the Cu atoms.

To complete this substitution study, the same X-ray diffraction analysis should also be performed on $Sr_{1-x}Ca_xCu_2(BO_3)_2$, but no single crystal was available.

Atom	U_{11} (Å^2)	U_{22} (Å^2)	U_{33} (Å^2)	U_{12} (Å^2)	U_{13} (Å^2)	U_{23} (Å^2)
Sr, Ba	0.0065 (5)	0.0073 (5)	0.0113 (4)	0	0	0
Cu	0.0025 (2)	0.0025 (2)	0.0264 (6)	-0.0005 (3)	0.0007 (3)	0.0007 (3)
B	0.003 (2)	0.003 (2)	0.012 (3)	0.001 (2)	0.004 (2)	0.004 (2)
O1	0.002 (1)	0.002 (1)	0.054 (4)	-0.002 (1)	0.000 (1)	0.000 (1)
O2	0.007 (1)	0.003 (1)	0.023 (1)	-0.002 (1)	0.001 (2)	0.001 (2)

Table 3.31: Room temperature structure of $Sr_{0.9}Ba_{0.1}Cu_2(BO_3)_2$: thermal displacement parameters.

3.7 Conclusion

The room temperature structure of the quasi-2D spin gap system $SrCu_2(BO_3)_2$ was studied by means of single crystal X-ray and neutron diffraction, and powder X-ray diffraction. We confirmed the structural model given in [19], with the supplementary information of the presence of a merohedral inversion twin, and we could refine anisotropic thermal displacement parameters for all the atoms. We observed that the thermal ellipsoids of all the atoms within the $Cu_2(BO_3)_2$ - layers are very elongated along the c axis, but this elongation is neither due to a pronounced anharmonicity of the potential close to the layers nor to a double-welled characteristic of the potential. The material undergoes a second order structural phase transition at $T_s = 395\,K$, from the low temperature space group $I\bar{4}2m$ to the high temperature space group $I4/mcm$. The investigation of the structural changes upon the phase transition together with the careful measurement of the magnetic susceptibility around T_s showed that there exist magnetic interactions between the $Cu_2(BO_3)_2$ - layers, much weaker than the ones within the layers. This supports more recent theoretical claims and magnetic measurements which suggest that a 3D orthogonal dimer model has to be applied to $SrCu_2(BO_3)_2$ [50], rather than the 2D Shastry-Sutherland model that had been used before [34, 36, 54, 55]. The substitution of the Sr atoms by Ba or Ca atoms have very few impacts on the structure and properties of $SrCu_2(BO_3)_2$. The most significant influence of the substitution is seen in the change in the c parameter and the disappearence of the plateaux in the magnetization curves. It is still not really understood why the presence of Ba atoms in the structure, that leads to less corrugated $Cu_2(BO_3)_2$ - layers and higher interlayer distances, causes the temperature of the structural phase transition to increase. To complete this substitution study, measurements of the magnetic susceptibility around the phase transition of $Sr_{1-x}M_xCu_2(BO_3)_2$ (M = Ba, Ca) should be performed on single phase powder samples, which we unfortunately weren't able to synthesize.

Chapter 4

$BaCuSi_2O_6$

4.1 Structure of $BaCuSi_2O_6$ from the literature

The room temperature structure of barium copper cyclosilicate $BaCuSi_2O_6$ was first described by L. W. Finger *et al.* in 1989. According to [21], it crystallizes in the tetragonal non-centrosymmetric space group $I\bar{4}m2$ (No. 119, $Z = 4$, $a = 7.042\,(3)$ Å, $c = 11.133\,(3)$ Å). Tables 4.1 and 4.2 summarize the structural parameters for $BaCuSi_2O_6$, as published in [21].

Atom	Multiplicity	x	y	z	Site symmetry
Ba1	2	$\frac{1}{2}$	0	$\frac{1}{4}$	$\bar{4}m2$
Ba2	2	0	$\frac{1}{2}$	$\frac{1}{4}$	$\bar{4}m2$
Cu	4	0	0	0.1225 (1)	$2mm.$
Si	8	0.2759 (2)	0.2759 (2)	0	..2
O1	16	0.2185 (10)	0.1645 (12)	0.1190 (5)	1
O2	8	0.7429 (13)	0	.5300 (7)	$.m.$

Table 4.1: Room temperature structure of $BaCuSi_2O_6$: atomic coordinates [21].

The structure consists of $Cu_2Si_4O_{12}$ - layers orthogonal to the c axis, separated by 8-fold coordinated Ba1 atoms and 12-fold coordinated Ba2 atoms (Fig. 4.1, 4.3). The layers are built from SiO_4 tetrahedra and distorted CuO_4 planar square groups.

The smallest Cu - Cu distance within a layer is 2.728 (3)Å, along the c axis: the Cu atoms form dimers parallel to c. The distance in the (**a**, **b**) plane between two Cu - Cu dimers (Fig. 4.2) is equal to the a lattice parameter: 7.042 (3) Å.
It is already obvious in Fig. 4.2 that the CuO_4 groups deviate distinctly from the ideal square planar coordination. A detailled discussion of this feature will be presented in subsection 4.1.2, page 69.

Atom	B_{11} (Å^2)	B_{22} (Å^2)	B_{33} (Å^2)	B_{12} (Å^2)	B_{13} (Å^2)	B_{23} (Å^2)	B_{eq} (Å^2)
Ba1	1.29 (8)	1.29 (8)	1.18 (10)	0	0	0	1.25 (4)
Ba2	1.29 (8)	1.29 (8)	0.59 (10)	0	0	0	1.08 (3)
Cu	0.97 (20)	0.14 (16)	1.04 (5)	0	0	0	0.72 (3)
Si	0.33 (6)	0.33 (6)	1.04 (10)	-0.05 (6)	0.3 (2)	-0.3 (2)	0.59 (3)
O1	1.7 (3)	2.4 (4)	1.4 (2)	-1.5 (3)	-0.1 (2)	0.5 (2)	2.1 (2)
O2	1.4 (3)	0.5 (3)	1.9 (4)	0	0.2 (3)	0	1.3 (2)

Table 4.2: Room temperature structure of $BaCuSi_2O_6$: thermal displacement parameters (from [21]). $B_{ij} = 8\pi^2 U_{ij}$. We should note here that most of the atoms show surprisingly anisotropic thermal ellipsoids.

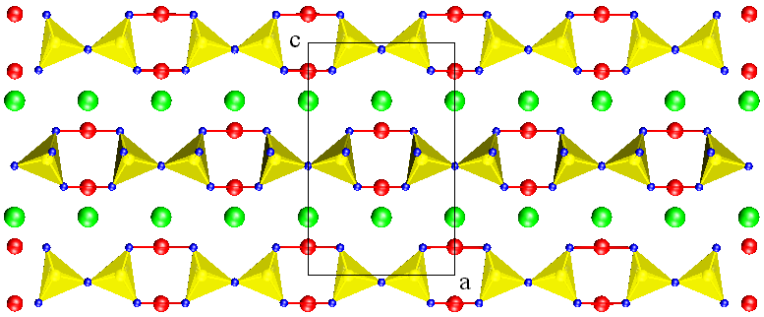

Figure 4.1: The $Cu_2Si_4O_{12}$ - layers normal to the c axis. The light polyhedra represent the SiO_4 tetrahedra, separated inside the layers by planar CuO_4 groups. The spheres between the layers represent the Ba atoms.

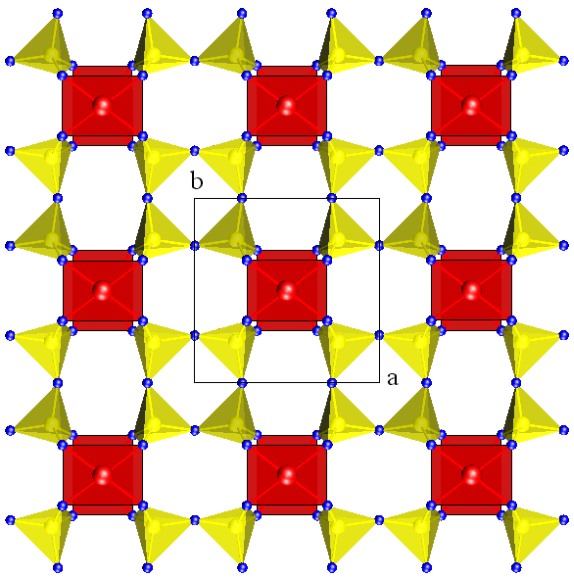

Figure 4.2: Projection of a $Cu_2Si_4O_{12}$ - layer onto the (**a**, **b**) plane.

In the Ba1 - O polyhedron (Fig. 4.3), all the Ba - O distances are equivalent and have the value 2.72 (1) Å. The Ba2 atom has two types of non equivalent O neighbors. The Ba2 - O distances are Ba2 - O1 = 3.17 (1) Å and Ba2 - O2 = 2.99 (1) Å.

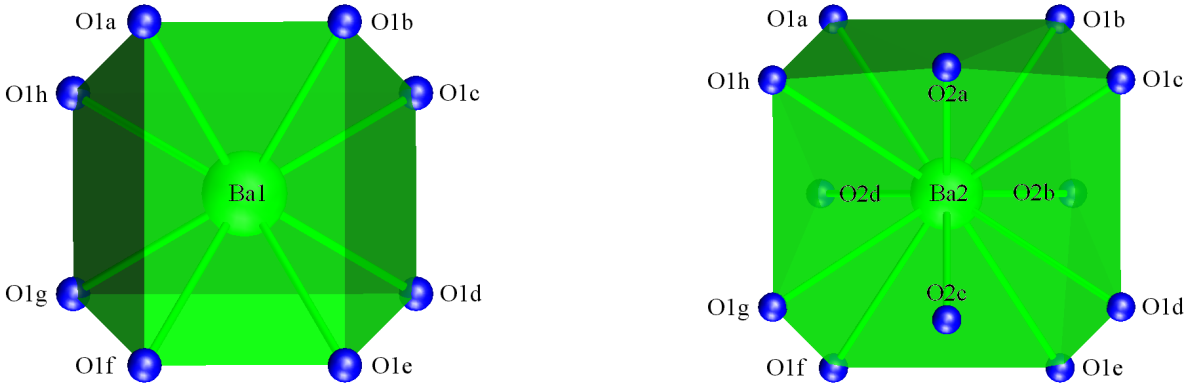

Figure 4.3: The environments of the Ba atoms, projected onto the (**a**, **b**) plane. Left: Ba1 atom. Right: Ba2 atom.

4.1.1 The isolated Si_4O_{12} rings

The structure of the barium copper silicate $BaCuSi_2O_6$ has the particularity to contain isolated Si_4O_{12} four-membered rings of SiO_4 tetrahedra. For this reason, this compound is assigned to the group of cyclosilicates.

Monocyclosilicates with isolated Si_4O_{12} single rings are very rare. Only seven such compounds have been enumerated in [56] (Tab. 4.3). The study of materials with unbranched Si_4O_{12} rings can be useful to get a better understanding of the Raman spectra and the structure of the amorphous SiO_2 [57], as will be seen in section 4.2. The simple structure of $BaCuSi_2O_6$ would make it a good candidate for this purpose: its Si_4O_{12} rings possess $2mm$ point symmetry, and the other compounds listed below exhibit lower point symmetries. They also present the inconvenience to be either hydrated, or to have some anions that do not belong to the Si_4O_{12} rings.

As an example, the structures of $BaCuSi_4O_{10}$, the synthetic isomorph of the gillepsite $BaFeSi_4O_{10}$, and of $BaCuSi_2O_6$ are compared in Fig. 4.4. $BaCuSi_4O_{10}$ crystallizes at room temperature in the tetragonal centrosymmetric space group $P4/ncc$ (No. 130), with the cell parameters $a = 7.447\,(1)$Å and $c = 16.138\,(2)$Å [58]. While the projections of both structures look almost identical in the (**a**, **b**) plane, the views of the structures with the c axis vertical clearly show that the Si_4O_{12} rings are isolated by the CuO_4 groups in the case of $BaCuSi_2O_6$, and that they form infinite layers in $BaCuSi_4O_{10}$.

Name	Formula
Taramellite	$Ba_4(Fe^{3+}, Ti)_4B_2[Si_4O_{12}]_2O_5Cl_x$
Nagashimalite	$Ba_4(V^{3+}, Ti)_4B_2[Si_4O_{12}]_2O_3(O, OH)_2Cl$
Baotite	$Ba_4Ti_4(Ti, Nb, Fe)_4[Si_4O_{12}]O_{16}Cl$
M' – $2PbO \cdot SiO_2$	$Pb_8[Si_4O_{12}]O_4$
Synthetic	$K_4Sc_2[Si_4O_{12}](OH)_2$
Synthetic	$Na_2BaNd_2[Si_4O_{12}][CO_3]$
Verplanckite	$Ba_{12}(Mn, Ti, Fe)_6[Si_4O_{12}]_3(O, OH)_2(OH, H_2O)_7Cl_9$

Table 4.3: Compounds with unbranched Si_4O_{12} single rings [56].

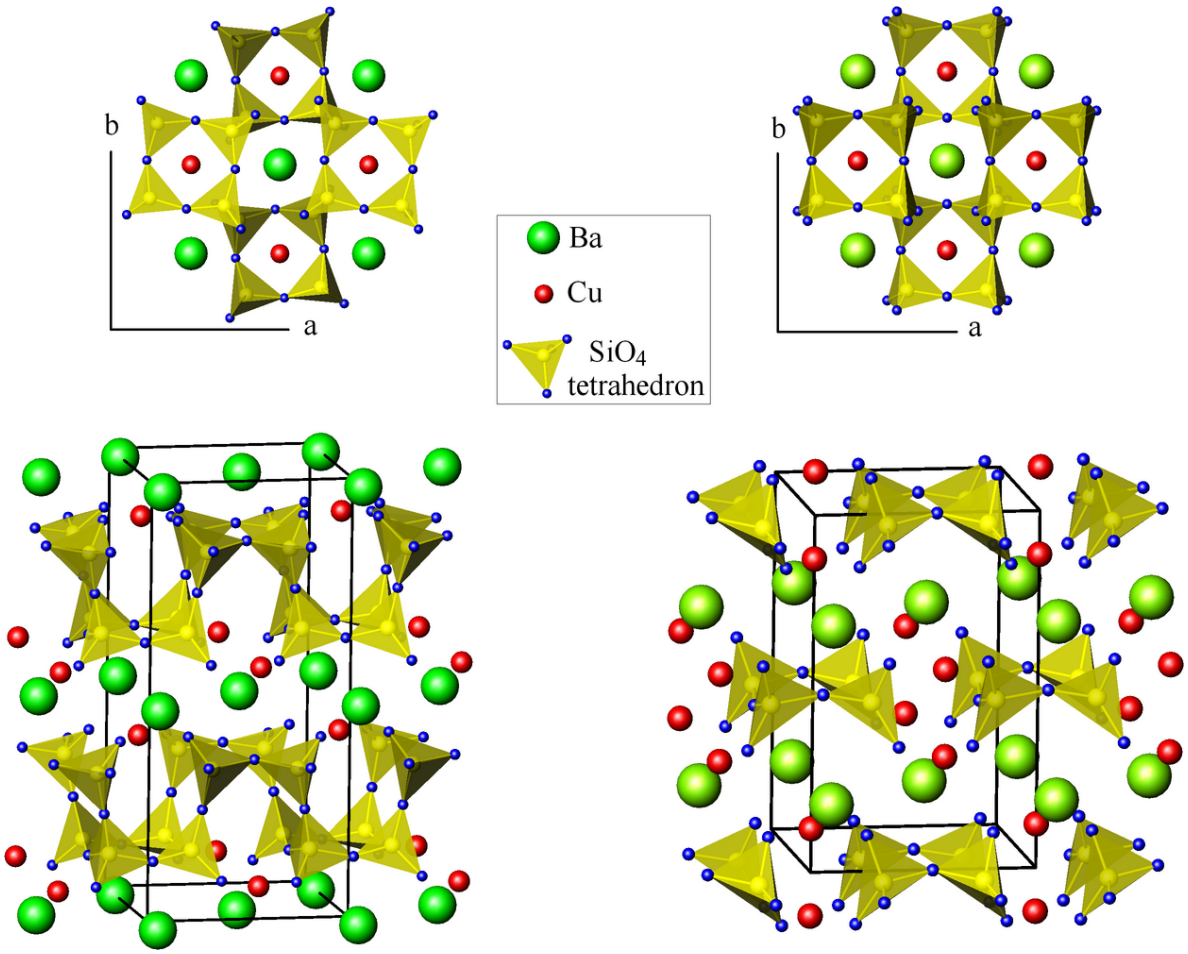

Figure 4.4: Top left (right): Projection of the structure of $BaCuSi_4O_{10}$ ($BaCuSi_2O_6$) in the (**a**, **b**) plane. Bottom left (right): View of $BaCuSi_4O_{10}$ ($BaCuSi_2O_6$) with the c axis vertical.

We now turn to the discussion of the geometry of the SiO_4 tetrahedra (Fig. 4.5). There are two non equivalent positions for the O atoms and one position for the Si atoms in the model from Finger [21]. Table 4.4 gives the bond lengths and angles in the SiO_4 tetrahedron. From these values, it can be seen that this group is slightly distorted. In the ideal case where it possesses the tetrahedral symmetry, the O - Si - O angle is equal to 109.28 °. Typical Si - O and O - O distances in a SiO_4 tetrahedron are respectively 1.60 Å and 2.62 Å [59].

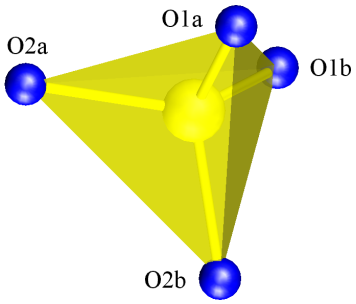

Figure 4.5: $BaCuSi_2O_6$: SiO_4 tetrahedron. O1a and O1b are equivalent, just as O2a and O2b.

Distances (Å)		Angles (°)	
Si - O1a	1.59 (1)	O1a - Si - O2a	110 (1)
Si - O2a	1.630 (5)	O2a - Si - O2b	109 (1)
O1a - O1b	2.70 (2)	O1a - Si - O1b	116 (2)
O2a - O2b	2.65 (2)	O2a - Si - O1b	106 (1)
O1a - O2a	2.64 (2)		

Table 4.4: Bond lengths and angles in the SiO_4 tetrahedron for $BaCuSi_2O_6$, calculated from the atomic coordinates given in [21].

4.1.2 The symmetry problem of the CuO_4 groups

All the Cu atoms in the structure occupy equivalent positions. It was already mentioned above that the CuO_4 groups have a quite distorted planar-rectangular coordination. This can be seen on figure 4.6. Table 4.5 lists the bond lengths and angles for the CuO_4 group.

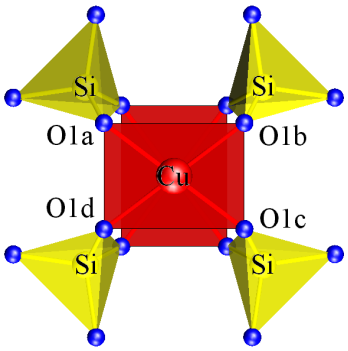

Figure 4.6: $BaCuSi_2O_6$: CuO_4 group. The atoms O1a, O1b, O1c and O1d are equivalent.

Distances (Å)		Angles (°)	
Cu - O1a	1.93 (1)	O1a - Cu - O1b	106 (1)
O1a - O1b	3.08 (2)	O1b - Cu - O1c	74 (1)
O1b - O1c	2.32 (2)	O1a - Cu - O1c	177.7 (5)

Table 4.5: Bond lengths and angles in the CuO_4 group for $BaCuSi_2O_6$, calculated from the atomic coordinates given in [21].

In the ideal planar-square coordination, the O - Cu - O angles are 90 °. The Cu - O distance is about 1.9 Å, the O - O distances lie between 2.5 Å and 3 Å.
Here, the short O - O distance of the CuO_4 group, 2.32 (2) Å, is very close to the limit where the electronic orbitals of the oxygen atoms could overlap. This was already the case in $SrCu_2(BO_3)_2$, but the CuO_4 group shared an edge with a BO_3 group that imposed the short O - O distance. There is no such constraint on the CuO_4 groups in $BaCuSi_2O_6$, as they only share corners with the SiO_4 tetrahedra.
The O1a - Cu - O1c angle, 177.7 (9) °, also shows that the CuO_4 group deviates from the planar configuration. The Cu atom stands slightly but significantly out of the perfect plane formed by the four O1 atoms: its distance to this plane is 0.039 (7) Å.
The high distortion of the planar-square coordination of the CuO_4 groups may point to a symmetry problem in the description of the structure of $BaCuSi_2O_6$.

4.1.3 Another, centrosymmetric model for $BaCuSi_2O_6$

A model in the centrosymmetric space group $I4/mmm$ (No. 139) was also suggested in [21], although not very satisfying because of the too large (unpublished) temperature factors for the oxygen atoms. The authors proposed that $BaCuSi_2O_6$ might undergo a phase transition at high temperature, from $I\bar{4}m2$ up to $I4/mmm$, but they said their crystals were untwinned, so that the temperature of this hypothetical phase transition would presumably be higher than the temperature of the synthesis (880 ° - 910 °, [60]). However, both centric and acentric models for the room temperature structure of $BaCuSi_2O_6$ were used in later papers [57]. The small difference between these models comes from the oxygen atoms, containing few electrons compared to the other atoms, and therefore being the less visible by X-ray diffraction.

Atom	Multiplicity	x	y	z	Site symmetry
Ba	4	$\frac{1}{2}$	0	$\frac{1}{4}$	$\bar{4}m2$
Cu	4	0	0	0.125	$4mm$
Si	8	0.275	0.275	0	$m.2m$
O1	16	0.195	0.195	0.120	$..m$
O2	8	0.740	0	$\frac{1}{2}$	$m2m.$

Table 4.6: $BaCuSi_2O_6$, described in the space group $I4/mmm$: idealized atomic coordinates. There were no error bars in [21].

Table 4.6 lists the atomic coordinates for the centric model. The projection of the structure in the (**a**, **c**) plane, showing the $Cu_2Si_4O_{12}$ - layers separated by Ba atoms along the c axis, is drawn in figure 4.7, to be compared with figure 4.1.

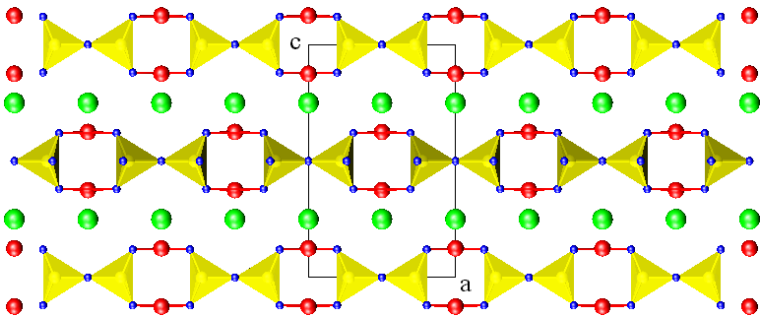

Figure 4.7: The $Cu_2Si_4O_{12}$ - layers normal to the c axis, in the space group $I4/mmm$ [21]. The light polyhedra represent the SiO_4 tetrahedra, separated by planar CuO_4 groups. The spheres between the layers represent the Ba atoms.

In fact, the structure of $BaCuSi_2O_6$ was also published, independently, by another team in 1992 [24]. The authors obtained the same model in the space group $I4/mmm$ (within a few standard deviations), but the isotropic thermal parameters of the oxygen atoms were very high.

There is, in this model, only one type of Ba atoms, with twelvefold coordination by oxygen (Fig. 4.8). The Ba - O1 distance is 2.931 (1) Å, the Ba - O2 distance 3.256 (1)Å.

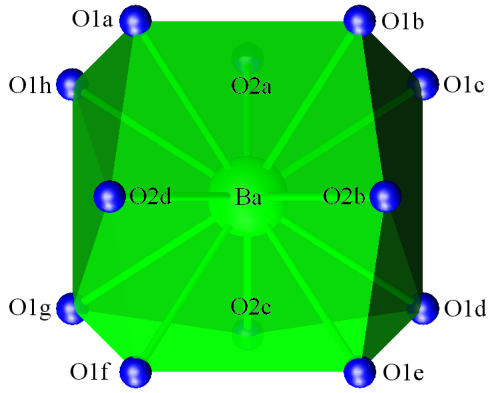

Figure 4.8: Coordination of the Ba atom, projected onto the (**a**, **b**) plane.

All the Cu atoms occupy equivalent positions. The Cu - Cu distance in the (**a**, **b**) plane is equal to a, 7.042 (3) Å, and the intradimer Cu - Cu distance along c is 2.783 (1) Å (see fig. 4.7). The small difference to the acentric model comes from the fact that only idealized (and not refined) atomic coordinates are presented in table 4.6.
Table 4.7 lists the bond angles and distances within the CuO_4 group, calculated from the centrosymmetric model.
It appears that the CuO_4 group deviates very little from the ideal planar square configuration (Fig. 4.9), because the Cu atom is situated at 0.055 (1)Å above the perfect plane formed by the O1 atoms. The O - O edges of the CuO_4 group are identical in this model.

To complete the overview of the centric model for $BaCuSi_2O_6$, the symmetry of the SiO_4 tetrahedra and of the Si_4O_{12} isolated rings will now be briefly discussed.
The bond lengths and angles for the SiO_4 tetrahedron are presented in table 4.8. The use of the centric space group makes the bond lengths become smaller, and the difference between the O - Si - O angles increases, compared to the space group $I\bar{4}m2$.

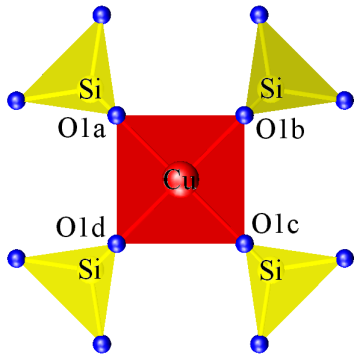

Figure 4.9: Centric model: CuO_4 group. The atoms O1a, O1b, O1c and O1d are equivalent.

Distances (Å)		Angles (°)	
Cu - O1a	1.943 (1)	O1a - Cu - O1b	89.9 (1)
O1a - O1b	2.746 (1)	O1b - Cu - O1c	89.9 (1)
O1b - O1c	2.746 (1)	O1a - Cu - O1c	176.7 (1)

Table 4.7: Bond lengths and angles in the CuO_4 group for $BaCuSi_2O_6$, calculated from the centric model given in [21].

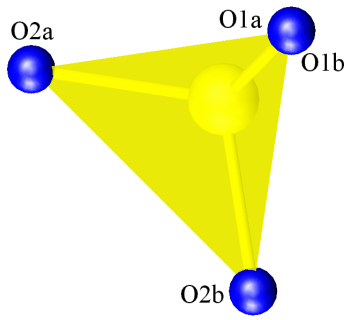

Figure 4.10: Centric model: the SiO_4 tetrahedron. O1a and O1b are equivalent, like O2a and O2b.

Distances (Å)		Angles (°)	
Si - O1a	1.555 (1)	O1a - Si - O2a	107.6 (1)
Si - O2a	1.604 (1)	O2a - Si - O2b	107.7 (1)
O1a - O1b	2.672 (1)	O1a - Si - O1b	118.4 (1)
O2a - O2b	2.589 (1)	O2a - Si - O1b	107.6 (1)
O1a - O2a	2.549 (1)		

Table 4.8: Bond lengths and angles in the SiO_4 tetrahedron for $BaCuSi_2O_6$, calculated from the centric model given in [21].

In the model with the acentric space group $I\bar{4}m2$ (Fig. 4.11), the Si_4O_{12} rings have $2mm$ point symmetry. They have $4/mmm$ point symmetry in the $I4/mmm$ centric model (Fig. 4.12).
The symmetry of the Si_4O_{12} rings in $BaCuSi_2O_6$ was used to analyze the structure of amorphous SiO_2 by means of Raman spectroscopy measurements [21, 57].

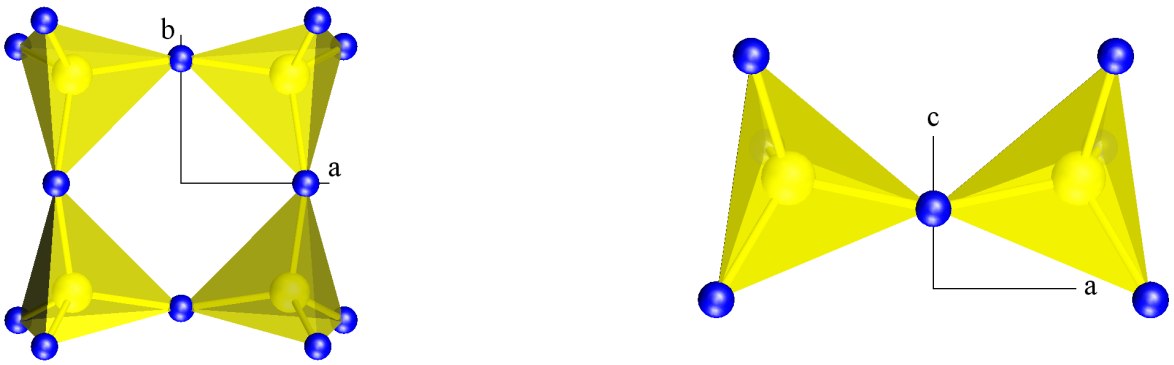

Figure 4.11: Si_4O_{12} rings in the acentric model. Left: projection onto the (**a**, **b**) plane. Right: projection onto the (**a**, **c**) plane.

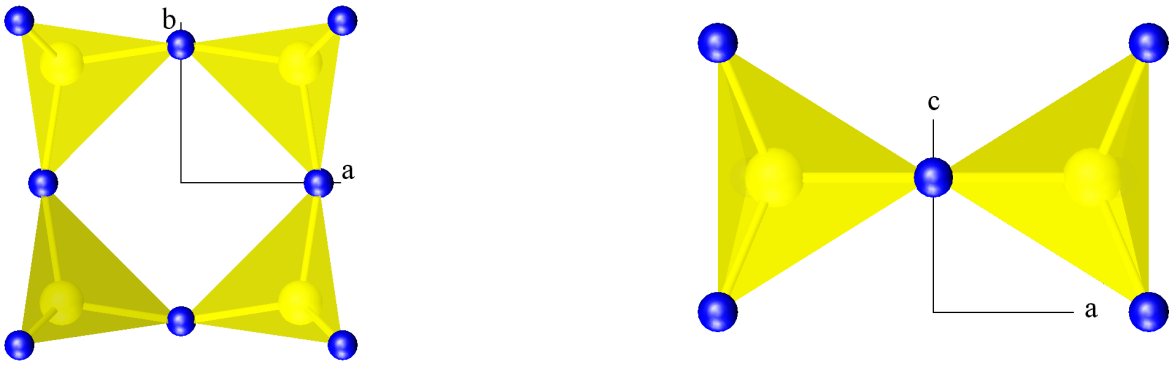

Figure 4.12: Si_4O_{12} rings in the centric model. Left: projection onto the (**a**, **b**) plane. Right: projection onto the (**a**, **c**) plane.

4.2 Raman spectroscopy experiments

The Raman spectroscopy measurements were performed by L. W. Finger *et al.* [21], in order to observe the vibrational modes characteristic of the Si_4O_{12} four-membered rings and of the CuO_4 planar group (Fig. 4.13).
According to [21], the band at 579 cm^{-1} corresponds to in-plane streching motion of the Cu - O bonds in the CuO_4 group.
The phonon mode at 506 cm^{-1} is associated to a vibration inside the Si_4O_{12} ring. This idea is supported by the fact that many silicates with a 4 - ring structure exhibit a phonon mode with a frequency very close to the one measured here, independent of the isolated or linked nature of these rings. For example, the frequency of this mode is 513 cm^{-1} for the orthoclase $KAlSi_3O_8$, 506 cm^{-1} for the low albite $NaAlSi_3O_8$ and 503 cm^{-1} for the anorthite $CaAl_2Si_2O_8$ – these three feldspars have a similar linkage of the Si_4O_{12} rings (Fig. 4.14). This indicates the strong localization within the Si_4O_{12} rings of the 506 cm^{-1} phonon mode in $BaCuSi_2O_6$.

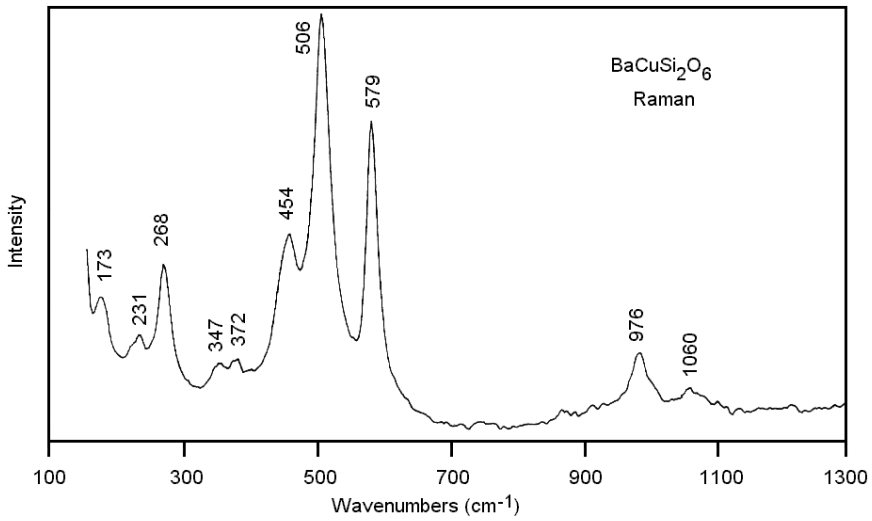

Figure 4.13: Raman spectroscopy measurement on $BaCuSi_2O_6$ (Fig. 3 from [21]).

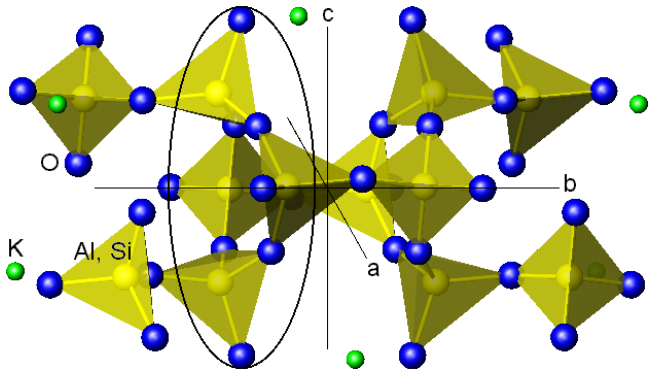

Figure 4.14: Structure of $KAlSi_3O_8$: $C\frac{2}{m}$ (No. 12), $Z = 4$, $a = 8.563\,(1)$ Å, $b = 12.96\,(1)$ Å, $c = 7.210\,(1)$ Å, $\beta = 116.073\,(9)\,^\circ$ [61]. The Si_4O_{12} rings (shown in the ellipse) are connected to each other.

With the Raman spectroscopy measurements from [21], D. A. McKeown and M. I. Bell published lattice dynamics calculations for both centric and acentric models of the structure of $BaCuSi_2O_6$ [57]. Figure 4.15 shows calculated vibration modes of the Si_4O_{10} rings in $BaCuSi_2O_6$ for the acentric model.
It was demonstrated in the acentric case that the bridging-oxygen breathing mode of the rings, responsible for the $506\,cm^{-1}$ line (Fig. 4.15.a, left), can only exist when the rings are strongly coupled to each other. This coupling between the rings is achieved by the CuO_4 groups, sharing edges with the SiO_4 tetrahedra (Fig. 4.2, page 66). For the centrosymmetric model, the calculated inter-ring bond strength is weaker and no such breathing mode was obtained, so that the acentric model was considered as correct.

In the Raman spectrum of amorphous SiO_2, a mode of frequency 495 cm^{-1} (the D_1 defect line) was observed and interpreted as a localized vibration within four-membered Si_4O_{12} rings [62]. The closeness of this frequency to the calculated one for the bridging-oxygen breathing mode of the SiO_4 rings in $BaCuSi_2O_6$ confirms the idea that both modes are related.

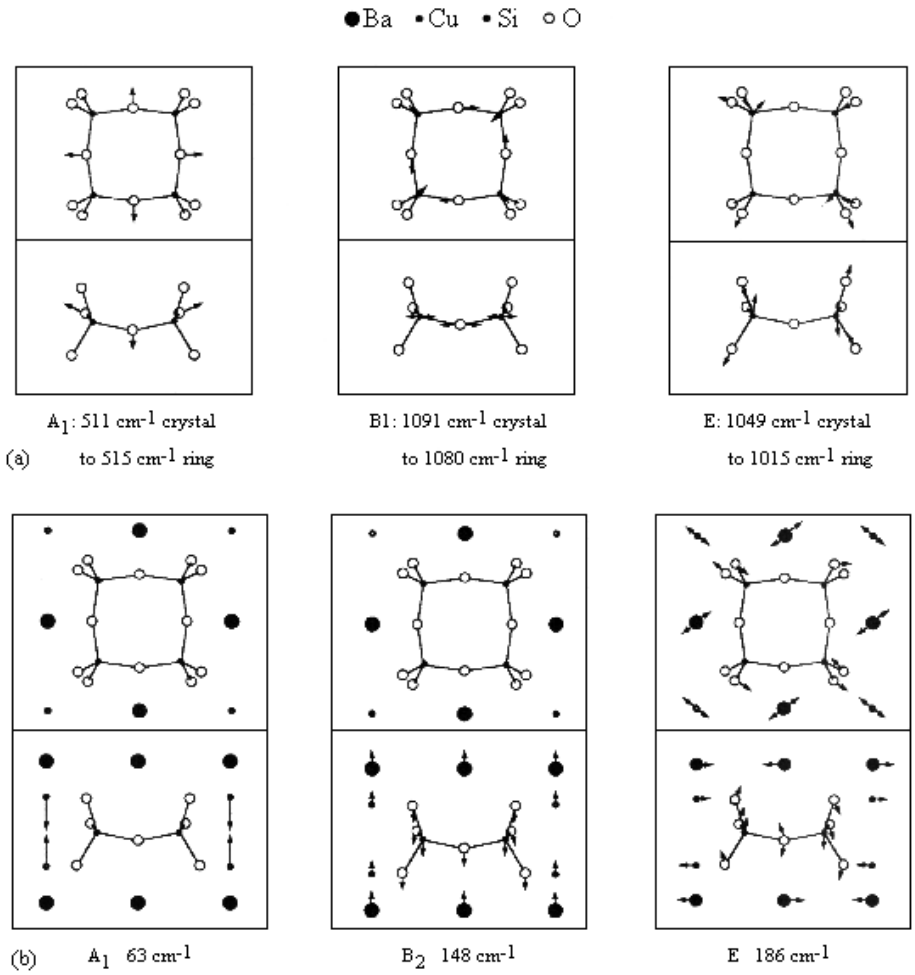

Figure 4.15: (a): Calculated normal modes of the Si_4O_{12} rings. (b): Examples of lattice vibrational modes for $BaCuSi_2O_6$ (Fig. 3 from [57]). In (a) and (b), the diagrams in the upper and the lower boxes are respectively the projections along the z and the x axes.

4.3 Magnetic properties of $BaCuSi_2O_6$

The Cu^{2+} ions in $BaCuSi_2O_6$ are arranged in layers perpendicular to the c direction. They form a square-lattice of Cu - Cu antiferromagnetic dimers, parallel to the c axis (Fig. 4.16). Figure 4.17 shows the structure constituted by the Cu^{2+} ions only.

The intralayer Cu - Cu distance is 2.728 (3) Å. The next shortest Cu - Cu distance in the structure is 5.732 (3) Å, this is the distance between a Cu^{2+} ion and its equivalent by bodycentering. Finally, the Cu - Cu dimers within a layer are at a distance of $a = 7.042\,(3)$ Å. To a reasonnable approximation, we can then consider the dimers as magnetically isolated.

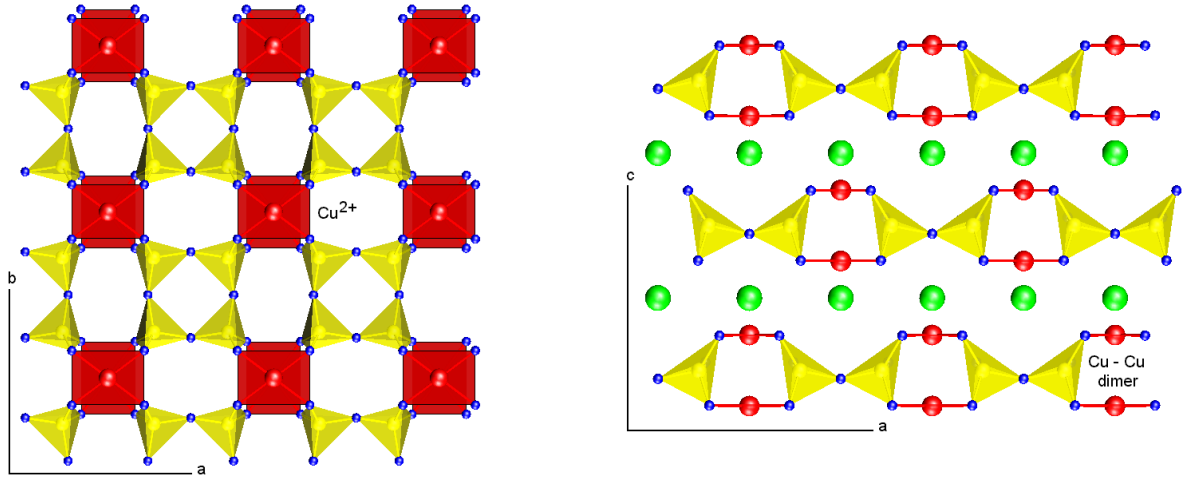

Figure 4.16: The acentric structure of $BaCuSi_2O_6$. Left: projection onto the (**a**, **b**) plane. Right: View with the c axis vertical.

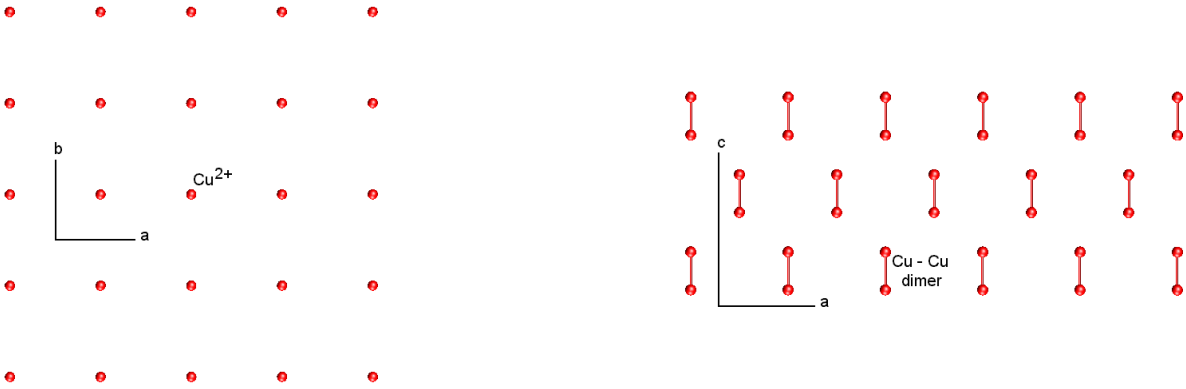

Figure 4.17: The structure formed by the Cu^{2+} ions. Left: projection onto the (**a**, **b**) plane. Right: View with the c axis vertical.

$BaCuSi_2O_6$ is a quasi-two dimensional antiferromagnetic system. It has a spin-singlet dimerized quantum ground state, with a spin-gap $\Delta \approx 4.5$ meV. Figure 4.18 shows the magnetic susceptibility of a $BaCuSi_2O_6$ single crystal between 0 K and 200 K (from [22]). As can be seen, the compound doesn't undergo any magnetic phase transition.

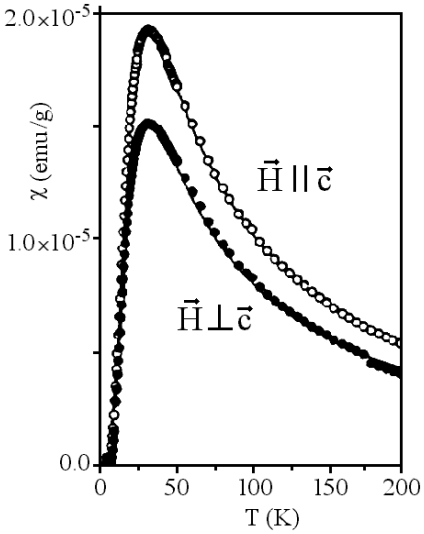

Figure 4.18: Magnetic susceptibility of a $BaCuSi_2O_6$ single crystal. The solid lines are calculated for the isolated-dimer model (Fig. 2.a from [22]).

The Heisenberg $S = \frac{1}{2}$ Hamiltonian of the system is written as

$$\mathscr{H} = J_1 \sum_i \widehat{S_i^1}\widehat{S_i^2} + J_2 \sum_{<i,j>,\alpha} \widehat{S_i^\alpha}\widehat{S_j^\alpha} + J_2' \sum_{<i,j>',\alpha} \widehat{S_i^\alpha}\widehat{S_i^\alpha}$$

with J_1 the intradimer exchange constant, J_2 and J_2' the exchange constants between nearest and second nearest neighbors within each plane of a layer. The index i labels the sites in a given plane, $< i, j >$ and $< i, j >'$ are nearest and second nearest neighbors in the same plane, and $\alpha = 1, 2$ indexes the two planes of the layer.
The fit of this equation, together with physical considerations from inelastic neutron scattering experiments, lead to $J_1 = \Delta \approx 4.5\,\text{meV}$, $J_2 = 0$ and $\frac{J_1}{J_2'} \approx 24$ [22].

4.4 A new model for the room temperature structure

4.4.1 The superstructure reflections

In order to clarify the somehow unsatisfying situation concerning the crystal structure of $BaCuSi_2O_6$, a room temperature data set on a $0.20 \times 0.19 \times 0.13$ mm^3 single crystal has been measured, with the Stoe-IPDS-I diffractometer (Tab. 4.9).

During the indexation of the diffracted intensities, we have noticed the presence of many weak superstructure reflections. They correspond to a $(\sqrt{2} \times \sqrt{2} \times 2)$ supercell, rotated by 45 ° in the $(\mathbf{a}, \mathbf{b})$ plane and doubled along $\mathbf{c}$ compared to the one given in [21].
In order to avoid the presence of the $\frac{\lambda}{2}$ radiation in the diffracted intensities, a new

U (kV)	I (mA)	φ - range (°)	$\Delta\varphi$ (°)	d (mm)	2θ - range (°)	t (mn)
50	25	0 - 229.5	1.7	40	5.7 - 66	3

Table 4.9: Conditions of the measurement with the Stoe-IPDS-I diffractometer.

measurement was performed with the conditions given in table 4.10.

U (kV)	I (mA)	φ - range (°)	$\Delta\varphi$ (°)	d (mm)	2θ - range (°)	t (mn)
30	25	0 - 300	0.8	40	5.7 - 66	10

Table 4.10: Conditions of the second measurement with the Stoe-IPDS-I diffractometer.

Figure 4.19 shows the measured reflections in the reciprocal space, projected onto the $(\mathbf{a}^*, \mathbf{b}^*)$ plane. The reflections are represented by the light dots, and the drawn reciprocal cell is the one published by L. W. Finger *et al.* [21].

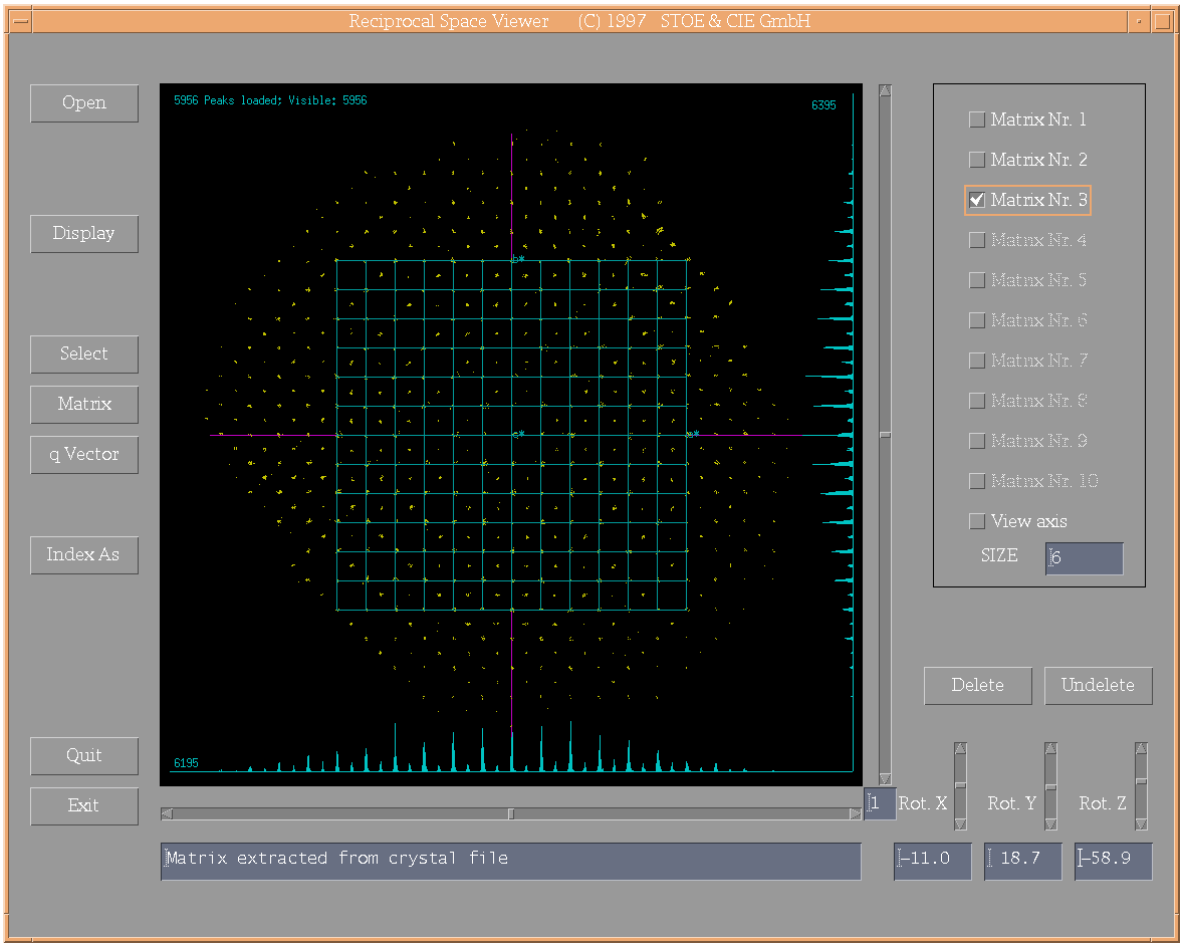

Figure 4.19: $BaCuSi_2O_6$ at room temperature: the superstructure reflections.

All the superstructure reflections are still present with a X-ray tube voltage of 30 kV. It appears from the diffracted intensities that the cell remains tetragonal and I - centered. The new basis vectors are then $\mathbf{a'} = \mathbf{a} + \mathbf{b}$, $\mathbf{b'} = \mathbf{b} - \mathbf{a}$ and $\mathbf{c'} = \mathbf{2\,c}$, and the new cell parameters are $a' = 10.009\,(2)$ Å and $c' = 22.467\,(6)$ Å.

4.4.2 Attempts to solve the room temperature structure

The room temperature structure of $BaCuSi_2O_6$ was redetermined using the data set measured with 30 kV.

The average intensity ratio between the superstructure and the main reflections is very small, about $\frac{1}{100}$. This could be an indication that $BaCuSi_2O_6$ might undergo a structural phase transition close to room temperature, with the space group $I\bar{4}m2$ in the high temperature phase.
We thus first tried to systematically solve the room temperature structure by means of direct methods in all the subgroups of $I\bar{4}m2$ that are tetragonal and I - centered, but this attempt failed.
We then transformed the model published in [21] into space group $P1$ (No. 1) by calculating all the atomic positions in the new cell. This structure was refined using geometrical constraints on the bond lengths, namly the Cu - O, Si - O and Ba - O bond lenghts. At the end of the refinement, the CuO_4 planar groups had become more symmetric and were closer to squares than in the model with the space group $I\bar{4}m2$.
Using the software Platon, we looked for the presence of symmetry elements in the structure and obtained three possible space groups: $I4_1/a$ (No. 88), $I4_1cd$ (No. 110) and $I4_1/acd$ (No. 142). In order to compare the results in each space group, the refinements were made with isotropic thermal parameters for all atoms.

- Solution in the space group $I4_1/a$

The internal R - values of the data set for the centrosymmetric space group $I4_1/a$ before and after absorption correction (Laue group $4/m$) are 8.20 % and 5.37 %, respectively. The refinement of the 42 parameters converged without any problem, but the obtained R - values are R1 = 10.69 % for 1276 unique reflections with F_{obs} ¿ $4\,\sigma_{F_{obs}}$ (containing 722 unique superstructure reflections), R1 = 17.48 % for all 2099 data, wR2 = 14.91 %, and the goodness of fit GooF = 6.64. Table 4.11 gives the atomic coordinates in this model. It is noteworthy that, within the standard deviations, the position of the Ba atom is $(\frac{1}{4}, 0.0116, \frac{1}{2})$, which suggests a lack of symmetry in the model. The Ba - O, Cu - O and Si - O bond lengths have reasonable values. The CuO_4 planar squares are distorted (Fig. 4.20), but not as much as in the acentric model $I\bar{4}m2$ with the subcell.

Atom	Multiplicity	x	y	z	U_{eq}	Site symmetry
Ba	16	0.2500 (2)	0.0116 (1)	0.5000 (1)	0.0118 (2)	1
Cu1	8	0	$\frac{1}{4}$	0.0637 (1)	0.0097 (5)	2..
Cu2	8	0	$\frac{1}{4}$	0.5638 (1)	0.0097 (5)	2..
Si1	16	0.0006 (3)	0.9743 (3)	0.6251 (6)	0.0087 (8)	1
Si2	16	0.2244 (3)	0.7505 (3)	0.6249 (6)	0.0092 (9)	1
O1	16	0.128 (1)	0.879 (1)	0.6115 (8)	0.026 (3)	1
O2	16	0.307 (2)	0.766 (2)	0.685 (1)	0.042 (5)	1
O3	16	0.372 (1)	0.378 (1)	0.1406 (8)	0.024 (3)	1
O4	16	0.471 (1)	0.442 (1)	0.8149 (7)	0.015 (2)	1
O5	16	0.473 (1)	0.559 (1)	0.0657 (7)	0.017 (3)	1
O6	16	0.486 (2)	0.444 (2)	0.315 (1)	0.041 (5)	1

Table 4.11: Atomic coordinates and isotropic thermal parameters for $BaCuSi_2O_6$ in the space group $I4_1/a$ (origin choice 2).

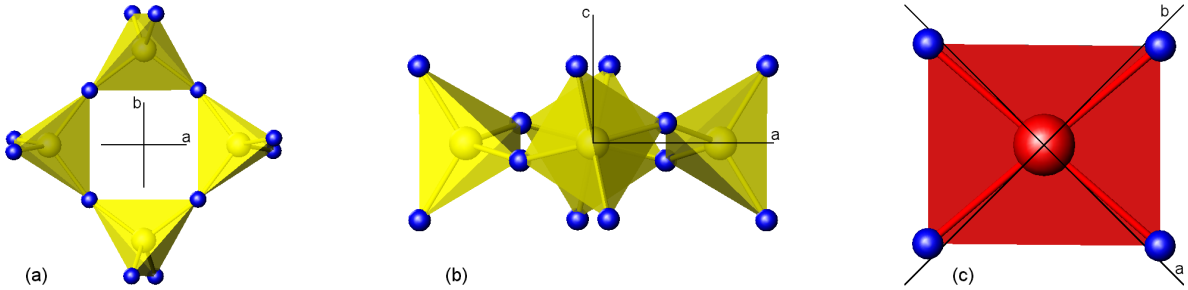

Figure 4.20: Structural details of $BaCuSi_2O_6$ in the space group $I4_1/a$. (a): Projection of a Si_4O_{12} ring onto the (**a**, **b**) plane. (b): The same ring seen with the c axis vertical. (c): Projection of a CuO_4 group onto the (**a**, **b**) plane.

- Solution in the space group $I4_1cd$

The non-centrosymmetric space group $I4_1cd$ gives a more satisfactory structure. The internal R - values of the data set before and after absorption correction (Laue group $4/mmm$) are 7.91 % and 5.06 %, respectively. The refinement was stable, the R - values for the 43 parameters are R1 = 4.11 % for 1364 unique reflections with F_{obs} ¿ 4 $\sigma_{F_{obs}}$ (containing 719 unique superstructure reflections), R1 = 7.01 % for all 2099 data, wR2 = 5.34 %, and the goodness of fit GooF = 2.48. The atomic coordinates are given in table 4.12. It is remarkable that the isotropic displacement parameters have become much smaller for the Si and O atoms.
The distortion of the CuO_4 planar squares (Fig. 4.21) is almost gone and subsists only slightly on the bond lengths.

Atom	Multiplicity	x	y	z	U_{eq}	Site symmetry
Ba	16	0.2517 (3)	0.7387 (1)	0	0.0118 (1)	1
Cu1	8	0	0	0.0642 (2)	0.0095 (6)	2..
Cu2	8	0	0	0.1867 (2)	0.0095 (7)	2..
Si1	16	0.2241 (8)	0.5017 (5)	0.6269 (3)	0.007 (1)	1
Si2	16	0.2753 (8)	0.5005 (5)	0.3780 (3)	0.009 (2)	1
O1	16	0.123 (1)	0.624 (1)	0.6444 (4)	0.014 (2)	1
O2	16	0.189 (1)	0.468 (2)	0.3150 (6)	0.011 (3)	1
O3	16	0.192 (1)	0.522 (1)	0.4392 (4)	0.009 (2)	1
O4	16	0.306 (2)	0.475 (2)	0.6820 (6)	0.017 (3)	1
O5	16	0.307 (1)	0.538 (1)	0.5672 (5)	0.012 (2)	1
O6	16	0.367 (1)	0.632 (1)	0.3634 (4)	0.017 (2)	1

Table 4.12: Atomic coordinates and isotropic thermal parameters for $BaCuSi_2O_6$ in the space group $I4_1cd$. Since the z coordinate is free in this space group, the Ba atom was fixed at $z = 0$.

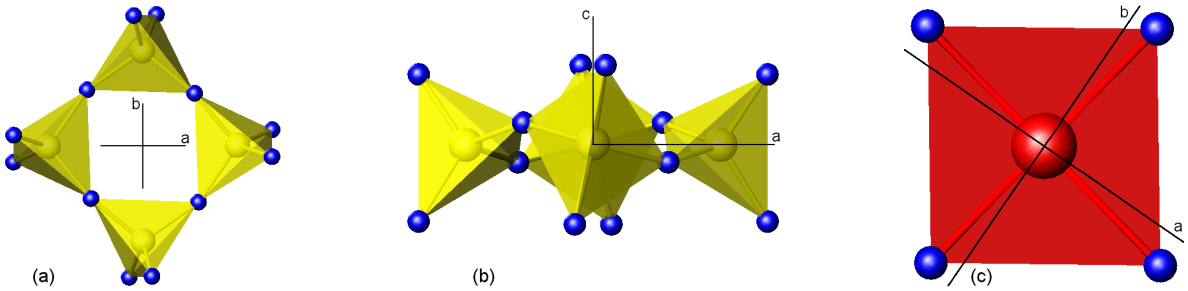

Figure 4.21: Structural details of $BaCuSi_2O_6$ in the space group $I4_1cd$. (a): Projection of a Si_4O_{12} ring onto the (**a**, **b**) plane. (b): The same ring seen with the c axis vertical. (c): Projection of a CuO_4 group onto the (**a**, **b**) plane.

- Solution in the space group $I4_1/acd$

From the space group $I4_1cd$ to the space group $I4_1/acd$, the origin is shifted by the translation vector $(0, \frac{1}{4}, 0)$. The comparison of the atomic coordinates after translation and the special positions in the space group $I4_1/acd$ was sufficient to find a starting model for the refinement. There are two origin choices possible for this space group, and we have to choose here the second one, with the origin on the inversion center.
The refinement was stable, the R - values for the 22 parameters are R1 = 4.22 % for 739 unique reflections with F_{obs} ¿ 4 $\sigma_{F_{obs}}$ (containing 385 unique superstructure reflections), R1 = 6.78 % for all 1056 data, wR2 = 5.58 %, and the goodness of fit GooF = 3.59. Table 4.13 gives the atomic coordinates.

Projections of the Si_4O_{12} rings and CuO_4 groups are shown in figure 4.22.

Atom	Multiplicity	x	y	z	U_{eq}	Site symmetry
Ba	16	$\frac{1}{4}$	0.98862 (5)	$\frac{1}{2}$	0.0124 (1)	.2.
Cu	16	0	$\frac{1}{4}$	0.06374 (3)	0.0101 (2)	2..
Si	32	0.2757 (1)	0.7510 (2)	0.8768 (2)	0.0088 (2)	1
O1	32	0.1912 (6)	0.7206 (7)	0.8161 (3)	0.015 (1)	1
O2	32	0.3723 (6)	0.8784 (6)	0.8594 (1)	0.019 (1)	1
O3	32	0.3074 (6)	0.7797 (7)	0.0641 (3)	0.015 (1)	1

Table 4.13: Atomic coordinates and isotropic thermal parameters for $BaCuSi_2O_6$ in the space group $I4_1/acd$ (origin choice 2).

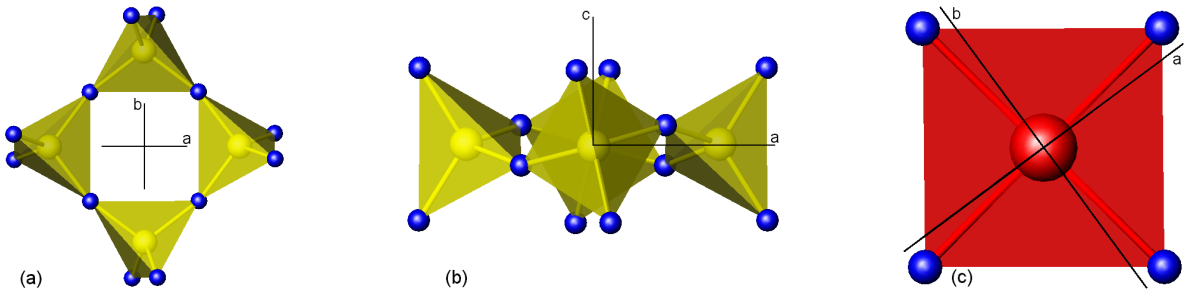

Figure 4.22: Structural details of $BaCuSi_2O_6$ in the space group $I4_1/acd$. (a): Projection of a Si_4O_{12} ring onto the (**a**, **b**) plane. (b): The same ring seen with the c axis vertical. (c): Projection of a CuO_4 group onto the (**a**, **b**) plane.

4.4.3 Discussion of the solution

Thus, the right space group to describe the room temperature structure of $BaCuSi_2O_6$ is either $I4_1cd$ or $I4_1/acd$. New absorption corrections for both Laue groups ($4mm$ and $4/mmm$) were made in order to improve the internal R - values.

- $I4_1cd$

The structure given in table 4.12 was refined using anisotropic thermal displacement parameters for the Ba, Cu and Si atoms. The R - values for the 58 parameters are then R1 = 3.34 % for 1364 unique reflections with F_{obs} ¿ 4 $\sigma_{F_{obs}}$, R1 = 6.10 % for all 2099 data, wR2 = 4.61 %, and the goodness of fit GooF = 2.19. Tables 4.14 and 4.15 give the results of the refinement.

Atom	Multiplicity	x	y	z	Site symmetry
Ba	16	0.2500 (3)	0.73868 (4)	0	1
Cu1	8	0	0	0.0638 (2)	2..
Cu2	8	0	0	0.1863 (2)	2..
Si1	16	0.2246 (7)	0.5004 (8)	0.6260 (4)	1
Si2	16	0.2757 (7)	0.5018 (8)	0.3765 (4)	1
O1	16	0.124 (1)	0.625 (1)	0.6445 (3)	1
O2	16	0.1908 (9)	0.4797 (9)	0.3113 (4)	1
O3	16	0.196 (2)	0.525 (2)	0.4340 (7)	1
O4	16	0.3088 (7)	0.4631 (8)	0.6805 (4)	1
O5	16	0.310 (1)	0.534 (1)	0.5640 (5)	1
O6	16	0.368 (1)	0.632 (1)	0.3638 (4)	1

Table 4.14: $BaCuSi_2O_6$: atomic coordinates in the space group $I4_1cd$.

Atom	U_{11} (Å^2)	U_{22} (Å^2)	U_{33} (Å^2)	U_{12} (Å^2)	U_{13} (Å^2)	U_{23} (Å^2)
Ba	0.0131 (2)	0.0122 (2)	0.0129 (1)	0 (n.s.)	-0.0019 (1)	0 (n.s.)
Cu1	0.005 (2)	0.005 (2)	0.016 (1)	0.003 (1)	0	0
Cu2	0.014 (2)	0.015 (2)	0.008 (1)	-0.004 (2)	0	0
Si1	0.007 (3)	0.008 (3)	0.012 (3)	-0.004 (2)	0 (n.s.)	0 (n.s.)
Si2	0.007 (3)	0.007 (3)	0.013 (4)	0 (n.s.)	-0.007 (2)	0 (n.s.)
O1	0.014 (2)	O2	0.010 (2)	O3	0.024 (4)	
O4	0.009 (2)	O5	0.006 (2)	O6	0.017 (2)	

Table 4.15: $BaCuSi_2O_6$: thermal displacement parameters ($I4_1cd$). Isotropic thermal displacement parameters were used for the oxygen atoms.

We then have one type of Ba atom in the structure, being 9 - coordinated, with Ba - O distances between 2.69 (1) Å and 3.14 (2) Å, but the O4b atom is also quite close to the Ba atom (Fig. 4.23, Tab. 4.16). However, the Ba - O4b distance is too big to consider O4b as a possible polyhedron ligand for Ba [63].
There are also two non-equivalent Cu atoms, two Si atoms and six O atoms.
The refinement pointed to an inversion twin, with an occupation of 42 (6) % in volume for the structure in table 4.14, that could also be a growth twin.

In fact, the structure deviates from the model published in [21] by a small displacement of the oxygen atoms around the $\bar{4}$ rotation axis. This explains the very weak intensities of the superstructure reflections, compared to the main reflections.
The influence of this deviation on the geometry of the Si_4O_{12} rings and of the CuO_4 groups is as follows:
In the model $I4_1cd$, the SiO_4 tetrahedra are less symmetric than in the model $I\bar{4}m2$

with the subcell (Fig. 4.5, 4.24 and 4.25; Tab. 4.4, 4.17 and 4.18).
All the distances in each SiO_4 tetrahedra are different. The Si - O distances range from 1.53 (1) Å up to 1.71 (1) Å, the O - O distances from 2.49 (2) Å up to 2.82 (1) Å, and the O - Si - O angles lie between 103.0 (9) ° and 118.9 (7) °.
Figure 4.26 shows the projections of the Si_4O_{12} rings onto the (**a**, **b**) and (**a**, **c**) planes. Although we have two non-equivalent Si atoms in the structure, they build only one type of Si_4O_{12} ring.
The Si_4O_{12} ring possesses 2.. point symmetry, the 2-fold rotation axis being on the position $(0, 0, z)$.

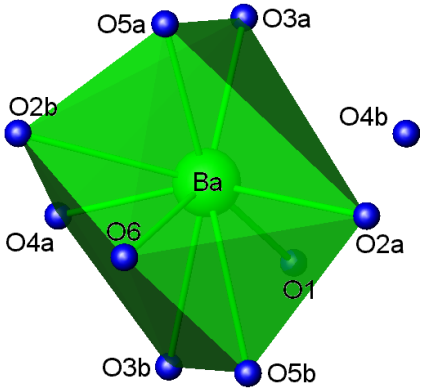

Figure 4.23: Coordination of the Ba atom, projected onto the (**a**, **b**) plane.

Distances (Å)		Distances (Å)	
Ba - O1	2.92 (2)	Ba - O4a	2.69 (1)
Ba - O2a	2.72 (1)	Ba - O4b	3.34 (2)
Ba - O2b	3.12 (2)	Ba - O5a	2.76 (1)
Ba - O3a	2.85 (2)	Ba - O5b	3.14 (2)
Ba - O3b	3.08 (2)	Ba - O6	3.01 (2)

Table 4.16: Coordination of the Ba atom: Ba - O distances.

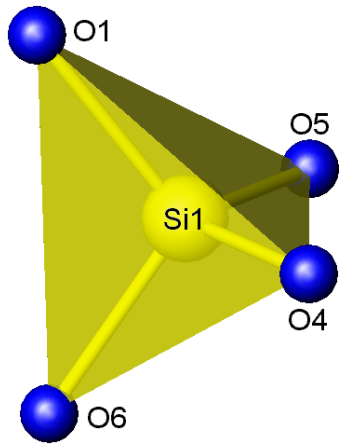

Figure 4.24: $BaCuSi_2O_6$: $Si1O_4$ tetrahedron.

Distances (Å)		Angles (°)	
Si1 - O1	1.66 (2)	O1 - Si1 - O4	108.7 (7)
Si1 - O4	1.53 (1)	O1 - Si1 - O5	111.6 (6)
Si1 - O5	1.67 (1)	O1 - Si1 - O6	107.7 (4)
Si1 - O6	1.64 (1)	O4 - Si1 - O5	115.9 (6)
O1 - O4	2.59 (2)	O4 - Si1 - O6	104.4 (6)
O1 - O5	2.75 (2)	O5 - Si1 - O6	108.0 (7)
O1 - O6	2.66 (2)		
O4 - O5	2.71 (2)		
O4 - O6	2.51 (1)		
O5 - O6	2.68 (2)		

Table 4.17: $BaCuSi_2O_6$: bond lengths and angles in the $Si1O_4$ tetrahedron, for the model $I4_1cd$.

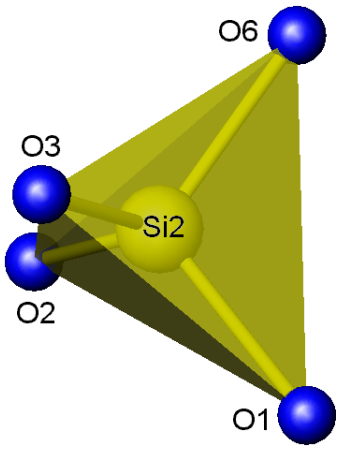

Figure 4.25: $BaCuSi_2O_6$: $Si2O_4$ tetrahedron.

Distances (Å)		Angles (°)	
Si2 - O1	1.65 (1)	O1 - Si2 - O2	114.3 (6)
Si2 - O2	1.71 (1)	O1 - Si2 - O3	103.0 (9)
Si2 - O3	1.53 (2)	O1 - Si2 - O6	108.0 (5)
Si2 - O6	1.63 (1)	O2 - Si2 - O3	118.9 (7)
O1 - O2	2.82 (1)	O2 - Si2 - O6	103.5 (6)
O1 - O3	2.49 (2)	O3 - Si2 - O6	108.9 (8)
O1 - O6	2.65 (2)		
O2 - O3	2.79 (2)		
O2 - O6	2.62 (2)		
O3 - O6	2.57 (2)		

Table 4.18: $BaCuSi_2O_6$: bond lengths and angles in the $Si2O_4$ tetrahedron, for the model $I4_1cd$.

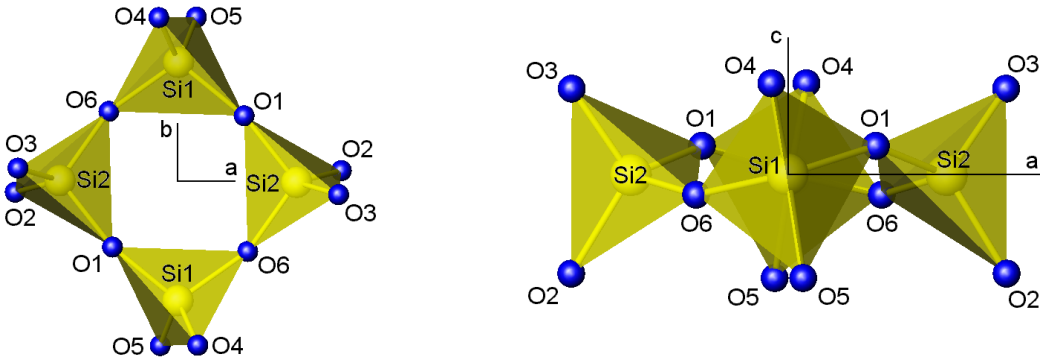

Figure 4.26: Si_4O_{12} rings in the model $I4_1cd$. Left: projection onto the (**a**, **b**) plane. Right: projection onto the (**a**, **c**) plane.

The geometry of the CuO_4 groups is improved a lot, compared to the $I\bar{4}m2$ model (Fig. 4.6, 4.27 and 4.28; Tab. 4.5, 4.19 and 4.20). There are now two different Cu - O bond lengths, but the O - O distances have become closer to each other and the O - Cu - O angles are closer to 90 °.

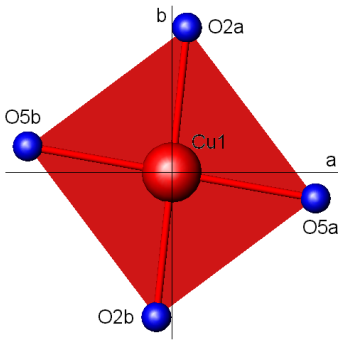

Figure 4.27: $BaCuSi_2O_6$: $Cu1O_4$ group.

Distances (Å)		Angles (°)	
Cu1 - O2a	1.92 (1)	O2a - Cu1 - O5a	94.1 (4)
Cu1 - O5a	1.94 (2)	O5a - Cu1 - O2b	85.9 (4)
O2a - O5a	2.83 (1)	O2a - Cu1 - O2b	176.6 (5)
O5a - O2b	2.63 (1)	O5a - Cu1 - O5b	179.7 (7)

Table 4.19: $BaCuSi_2O_6$: bond lengths and angles in the $Cu1O_4$ group, for the model $I4_1cd$.

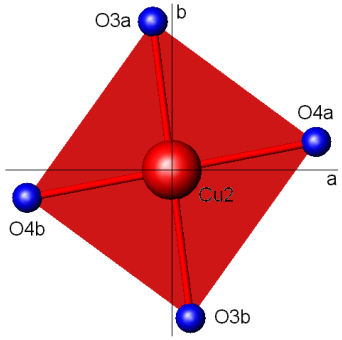

Figure 4.28: $BaCuSi_2O_6$: $Cu2O_4$ group.

Distances (Å)		Angles (°)	
Cu2 - O3a	1.95 (1)	O3a - Cu2 - O4a	86.2 (5)
Cu2 - O4a	1.98 (2)	O4a - Cu2 - O3b	93.6 (5)
O3a - O4a	2.69 (2)	O3a - Cu2 - O3b	176.9 (9)
O4a - O3b	2.87 (2)	O4a - Cu2 - O4b	172.3 (6)

Table 4.20: $BaCuSi_2O_6$: bond lengths and angles in the $Cu2O_4$ group, for the model $I4_1cd$.

- $I4_1/acd$

In this model, anisotropic thermal displacement parameters could be correctly refined for all the atoms. The obtained R - values for the 48 parameters are R1 = 3.11 % for 739 unique reflections with F_{obs} ¿ 4 $\sigma_{F_{obs}}$, R1 = 4.95 % for all 1056 data, wR2 = 4.47 %, and the goodness of fit GooF = 2.92. Tables 4.21 and 4.22 give the results of the refinement.

Atom	Multiplicity	x	y	z	Site symmetry
Ba	16	$\frac{1}{4}$	0.98860 (5)	$\frac{1}{2}$	.2.
Cu	16	0	$\frac{1}{4}$	0.06375 (2)	2..
Si	32	0.27568 (8)	0.7511 (1)	0.8755 (4)	1
O1	32	0.1912 (6)	0.7214 (6)	0.8159 (3)	1
O2	32	0.3726 (4)	0.8783 (4)	0.8594 (1)	1
O3	32	0.3074 (6)	0.7803 (7)	0.0644 (3)	1

Table 4.21: $BaCuSi_2O_6$: atomic coordinates in the space group $I4_1/acd$.

In this model, all the Cu atoms are equivalent, as well as all the Ba and Si atoms. We have three non-equivalent O atoms.

The coordination polyhedron of the Ba atom (Fig. 4.29) looks very similar to the one in the model $I4_1cd$ (Fig. 4.23), but the O4b atom that was too far away from Ba has moved closer, so that the Ba atom is now 10-fold coordinated, with Ba - O distances between 2.707 (6) Å and 3.234 (7) Å (Tab. 4.23). The effective coordination number of the Ba atom was calculated using the program CHARD-IT [64].

Atom	U_{11} (Å^2)	U_{22} (Å^2)	U_{33} (Å^2)	U_{12} (Å^2)	U_{13} (Å^2)	U_{23} (Å^2)
Ba	0.0126 (3)	0.0120 (2)	0.0124 (1)	0	-0.0019 (1)	0
Cu	0.0093 (9)	0.0091 (9)	0.0116 (2)	0.0000 (3)	0	0
Si	0.0065 (4)	0.0079 (4)	0.0130 (4)	0.0000 (5)	-0.001 (2)	-0.0007 (5)
O1	0.008 (2)	0.019 (2)	0.019 (3)	-0.001 (2)	0.001 (2)	-0.004 (3)
O2	0.016 (2)	0.017 (2)	0.028 (2)	-0.007 (1)	-0.003 (2)	0.002 (2)
O3	0.011 (2)	0.018 (2)	0.016 (3)	-0.000 (2)	0.001 (2)	0.005 (3)

Table 4.22: $BaCuSi_2O_6$: thermal displacement parameters ($I4_1/acd$).

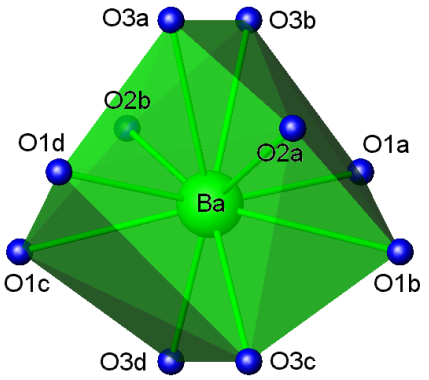

Figure 4.29: Coordination of the Ba atom, projected onto the (**a**, **b**) plane.

Distances (Å)	
Ba - O1a (= Ba - O1d)	2.707 (6)
Ba - O3c (= Ba - O3d)	2.788 (6)
Ba - O2a (= Ba - O2b)	2.960 (3)
Ba - O3a (= Ba - O3b)	3.109 (7)
Ba - O1b (= Ba - O1c)	3.234 (7)

Table 4.23: Coordination of the Ba atom: Ba - O distances.

The symmetry of the SiO_4 tetrahedra is greatly improved, compared to the model $I4_1cd$ (Fig. 4.29, Tab. 4.24). Although the four Si - O distances are non-equivalent, they lie between 1.612 (9) Å and 1.642 (6) Å. Also, the O - O distances are distributed within a smaller range, between 2.592 (7) Å and 2.753 (4) Å, and the O - Si - O angles range from 105.6 (5) ° up to 117.3 (2) °. The center of the Si_4O_{12} ring is at $(0, \frac{1}{4}, 0)$, its point symmetry is 2.., with a 2-fold rotation axis at $(0, \frac{1}{4}, z)$.

In the CuO_4 groups, the O - O distances are close to each other, and the O1 - Cu - O3 bond angles are almost 90 ° (Fig. 4.32, Tab. 4.25). The CuO_4 groups deviate slightly from planarity, as can be seen from the O1 - Cu - O1 and O3 - Cu - O3 angles.

If we compare both $I4_1cd$ and $I4_1/acd$ models, we see that the refinement of the structure with less parameters in the centrosymmetric space group $I4_1/acd$ leads to better R - values and improves the symmetries of the SiO_4 tetrahedra and CuO_4 groups. This is also the case for refinements of the structure in both space groups with only the superstructure reflections (Tab. 4.26). Thus, $I4_1/acd$ is chosen as the correct space group to describe the room temperature structure of $BaCuSi_2O_6$.

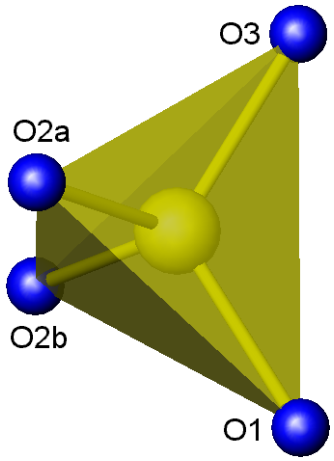

Figure 4.30: $BaCuSi_2O_6$: SiO_4 tetrahedron.

Distances (Å)		Angles (°)	
Si - O1	1.612 (9)	O1 - Si - O2a	109.5 (4)
Si - O3	1.612 (9)	O1 - Si - O2b	105.6 (5)
Si - O2a	1.640 (5)	O1 - Si - O3	117.3 (2)
Si - O2b	1.642 (6)	O2a - Si - O2b	107.9 (2)
O1 - O2a	2.656 (8)	O2a - Si - O3	105.8 (5)
O1 - O2b	2.592 (7)	O2b - Si - O3	110.4 (4)
O1 - O3	2.753 (4)		
O2a - O2b	2.654 (5)		
O2a - O3	2.593 (7)		
O2b - O3	2.672 (8)		

Table 4.24: $BaCuSi_2O_6$: bond lengths and angles in the SiO_4 tetrahedron, for the model $I4_1/acd$.

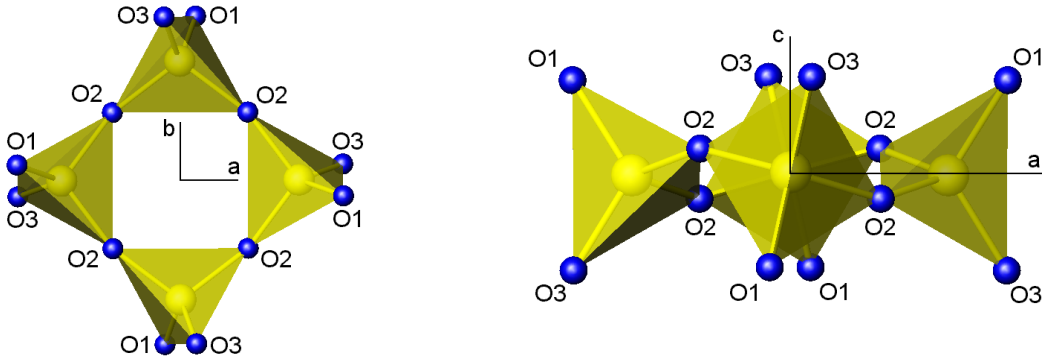

Figure 4.31: Si_4O_{12} rings in the model $I4_1/acd$. Left: projection onto the (**a**, **b**) plane. Right: projection onto the (**a**, **c**) plane.

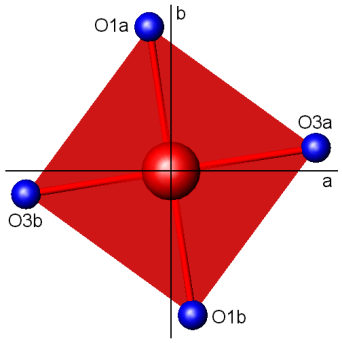

Figure 4.32: $BaCuSi_2O_6$: CuO_4 group.

Distances (Å)		Angles (°)	
Cu - O1	1.936 (6)	O1a - Cu - O3a	89.6 (4)
Cu - O3	1.952 (6)	O1a - Cu - O1b	177.1 (4)
O1a - O3a	2.739 (9)	O3a - Cu - O1b	90.4 (4)
O3a - O1b	2.759 (9)	O3a - Cu - O3b	179.1 (4)

Table 4.25: $BaCuSi_2O_6$: bond lengths and angles in the CuO_4 group, for the model $I4_1/acd$.

Space group	R1	Unique reflections with F_{obs} ¿ 4 $\sigma_{F_{obs}}$	Total number of unique reflections	wR2	GooF	Number of parameters
$I4_1cd$	4.07 %	719	951	6.63 %	1.097	43
$I4_1/acd$	4.04 %	385	477	6.06 %	1.440	37

Table 4.26: Qualities of the refinements of the structure of $BaCuSi_2O_6$ in the space groups $I4_1cd$ and $I4_1/acd$, taking only into account the superstructure reflections. The parameters for the Cu atom were not refined, since they only contribute to the main reflections.

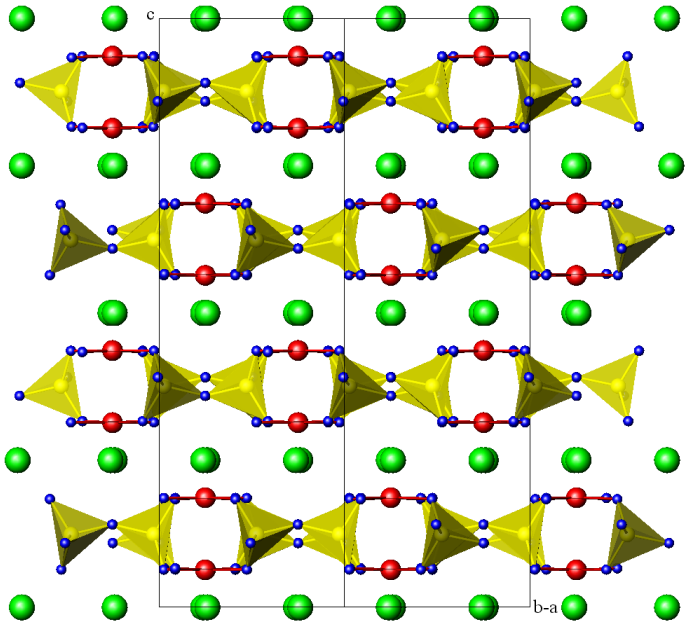

Figure 4.33: Room temperature structure of $BaCuSi_2O_6$ in the space group $I4_1/acd$: The $Cu_2Si_4O_{12}$ - layers normal to the c axis.

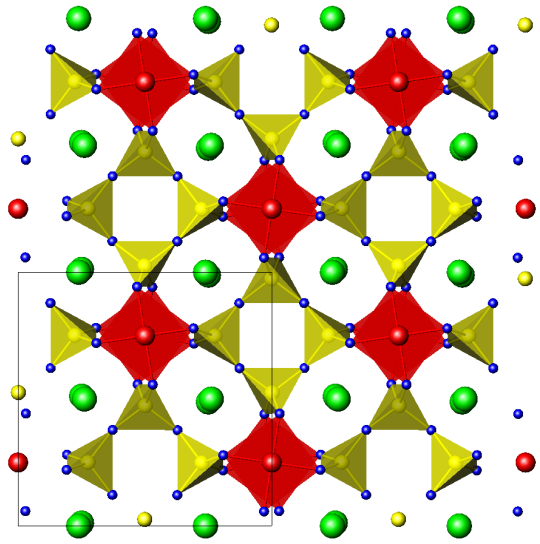

Figure 4.34: Room temperature structure of $BaCuSi_2O_6$ in the space group $I4_1/acd$: Projection of a $Cu_2Si_4O_{12}$ - layer onto the (**a**, **b**) plane.

4.5 $BaCuSi_2O_6$ at 200 K

The same crystal of $BaCuSi_2O_6$ was measured at 200 K on the Stoe-IPDS-I diffractometer (Tab. 4.27), because the hypothetical phase transition was thought to occur close to room temperature, so that the superstructure reflections would be already a lot stronger at 200 K.

U (kV)	I (mA)	φ - range (°)	$\Delta\varphi$ (°)	d (mm)	2θ - range (°)	t (mn)
30	25	0 - 300.8	0.8	40	5.7 - 66	10

Table 4.27: Conditions of the measurement at 200 K with the Stoe-IPDS-I diffractometer.

However, we noticed that the intensity ratio between the main and superstructure reflections didn't increase significantly, so that the accuracy on the position of the oxygen atoms couldn't be improved. The small temperature dependence of the intensity of the superstructure reflections indicates that if $BaCuSi_2O_6$ should undergo a structural phase transition at high temperatures, it should occur far above room temperature.

The cell parameters obtained from this measurement at 200 K are $a = 9.995\,(2)$ Å and $c = 22.497\,(6)$ Å. The space group remains $I4_1/acd$.
The internal R - values of the data set before and after absorption correction are 9.22 % and 6.72 %, respectively. The refinement was stable, and all the atoms could be refined with anisotropic thermal displacement parameters. The R - values for the 48 parameters are R1 = 2.43 % for 756 unique reflections with F_{obs} ¿ 4 $\sigma_{F_{obs}}$, R1 = 4.20 % for all 1050 data, wR2 = 3.36 %, and the goodness of fit GooF = 1.82. The results of the refinement are given in tables 4.28 and 4.29.

Atom	Multiplicity	x	y	z	Site symmetry
Ba	16	$\frac{1}{4}$	0.98780 (3)	$\frac{1}{2}$	.2.
Cu	16	0	$\frac{1}{4}$	0.06382 (2)	2..
Si	32	0.27571 (6)	0.75121 (8)	0.8755 (2)	1
O1	32	0.1913 (3)	0.7198 (4)	0.8157 (2)	1
O2	32	0.3731 (3)	0.8780 (3)	0.8587 (1)	1
O3	32	0.3080 (3)	0.7820 (4)	0.0648 (2)	1

Table 4.28: $BaCuSi_2O_6$ at 200 K: atomic coordinates.

At 200 K, the bond lengths and bond angles in the SiO_4 tetrahedra are almost identical to the ones at room temperature (Fig. 4.35, Tab. 4.30).

Atom	U_{11} (Å^2)	U_{22} (Å^2)	U_{33} (Å^2)	U_{12} (Å^2)	U_{13} (Å^2)	U_{23} (Å^2)
Ba	0.0071 (2)	0.0068 (2)	0.0062 (1)	0	-0.0014 (1)	0
Cu	0.0048 (5)	0.0044 (5)	0.0062 (2)	0.0000 (2)	0	0
Si	0.0036 (3)	0.0042 (3)	0.0069 (3)	-0.0000 (3)	-0.0010 (1)	-0.0006 (3)
O1	0.004 (1)	0.011 (1)	0.011 (2)	0.001 (1)	-0.001 (1)	0.004 (2)
O2	0.010 (1)	0.009 (1)	0.017 (1)	-0.005 (1)	-0.003 (1)	-0.005 (1)
O3	0.006 (1)	0.011 (1)	0.009 (2)	-0.000 (1)	0.001 (1)	0.001 (2)

Table 4.29: $BaCuSi_2O_6$ at 200 K: thermal displacement parameters.

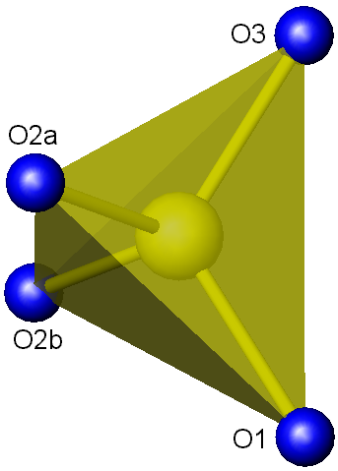

Figure 4.35: $BaCuSi_2O_6$ at 200 K: SiO_4 tetrahedron.

Distances (Å)		Angles (°)	
Si - O1	1.619 (6)	O1 - Si - O2a	109.5 (2)
Si - O3	1.611 (6)	O1 - Si - O2b	105.5 (3)
Si - O2a	1.641 (3)	O1 - Si - O3	117.3 (1)
Si - O2b	1.642 (4)	O2a - Si - O2b	107.7 (1)
O1 - O2a	2.663 (5)	O2a - Si - O3	105.9 (3)
O1 - O2b	2.595 (5)	O2b - Si - O3	110.7 (2)
O1 - O3	2.759 (3)		
O2a - O2b	2.651 (3)		
O2a - O3	2.595 (5)		
O2b - O3	2.676 (5)		

Table 4.30: $BaCuSi_2O_6$ at 200 K: bond lengths and angles in the SiO_4 tetrahedron.

Figure 4.36 shows the environments of the Cu atom at 200 K. The geometry of the CuO_4 groups remains constant with decreasing temperatures (Tab. 4.31).

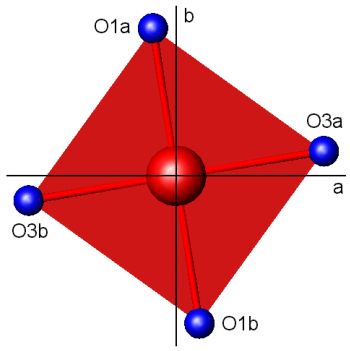

Figure 4.36: $BaCuSi_2O_6$ at 200 K: CuO_4 group.

Distances (Å)		Angles (°)	
Cu - O1	1.937 (3)	O1a - Cu - O3a	89.5 (2)
Cu - O3	1.946 (3)	O1a - Cu - O1b	177.5 (2)
O1a - O3a	2.733 (6)	O3a - Cu - O1b	90.5 (2)
O3a - O1b	2.757 (6)	O3a - Cu - O3b	178.7 (2)

Table 4.31: $BaCuSi_2O_6$ at 200 K: bond lengths and angles in the CuO_4 group.

4.6 Structural phase transition at 610 K

In order to determine the temperature of a possible structural phase transition with a change in the cell parameters, a series of orienting data sets were performed on the Stoe-IPDS-I diffractometer, with the same heating goniometer head as the one used in section 3.4.2, page 42. We found that $BaCuSi_2O_6$ undergoes a phase transition at 610 K: the weak superstructure reflections observed at room temperature disappear. A data set was collected at 640 K, with the conditions given in table 4.32. The cell parameters are $a = 7.110\,(2)$ Å and $c = 11.175\,(3)$ Å.

U (kV)	I (mA)	φ - range (°)	$\Delta\varphi$ (°)	d (mm)	2θ - range (°)	t (mn)
50	25	70 - 300.4	1.2	75	3.1 - 50.2	3

Table 4.32: Conditions of the measurement at 640 K with the Stoe-IPDS-I diffractometer.

The analysis of the diffracted intensities shows that the structure of $BaCuSi_2O_6$ remains tetragonal and I - centered in the high temperature phase. In order to solve the structure at 640 K, the room temperature structure from [21] was transformed to triclinic, refined and the possible symmetry elements were searched for with the program Platon, since this method proved to be successful for the room temperature structure.

The data set was corrected for absorption effects for the Laue group $4/m$. The structure is still tetragonal and body - centered. The internal R - values before and after absorption correction are 6.99 % and 3.48 %, respectively.
During the refinement of the structure in the space group $I1$, constraints were imposed on the Ba - O, Cu - O and Si - O bond lengths. The only space group proposed by the software Platon after the symmetry analysis is $I4/mmm$ (No. 139). The internal R - values of the data set before and after absorption correction for the corresponding Laue group $4/mmm$ are 13.92 % and 4.42 %, respectively.

Since the unit cell volume is divided by 4 upon the phase transition, we have $Z = 4$ for the high temperature structure. Hence, the unit cell contains 4 Ba atoms, 4 Cu atoms, 8 Si atoms and 24 O atoms. The multiplicity of a general position in the space group $I4/mmm$ being 32, all the atoms have to be located on special positions.
By comparing the atomic positions in the space group $I1$ with the special positions of the space group $I4/mmm$, the high temperature structure could be easily solved. The results of the refinement are given in tables 4.33 and 4.34. The R - values for the 21 parameters are R1 = 1.73 % for 151 unique reflections with F_{obs} ¿ 4 $\sigma_{F_{obs}}$, R1 = 2.11 % for all 170 data, wR2 = 2.66 %, and the goodness of fit GooF = 1.90.

Atom	Multiplicity	x	y	z	Site symmetry
Ba	4	0	$\frac{1}{2}$	$\frac{1}{4}$	$\bar{4}m2$
Cu	4	0	0	0.1234 (1)	$4mm$
Si	8	0.2755 (1)	0.2755 (1)	0	$m.2m$
O1	8	0.2403 (9)	$\frac{1}{2}$	0	$m2m.$
O2	16	0.1923 (4)	0.1923 (4)	0.1213 (4)	$..m$

Table 4.33: $BaCuSi_2O_6$ at 640 K: atomic coordinates ($I4/mmm$).

Atom	U_{11} (Å^2)	U_{22} (Å^2)	U_{33} (Å^2)	U_{12} (Å^2)	U_{13} (Å^2)	U_{23} (Å^2)
Ba	0.0236 (3)	0.0236 (3)	0.0242 (4)	0	0	0
Cu	0.0186 (5)	0.0186 (5)	0.0210 (7)	0	0	0
Si	0.0091 (5)	0.0091 (5)	0.030 (1)	-0.0009 (7)	0	0
O1	0.057 (4)	0.010 (2)	0.121 (7)	0	0	0
O2	0.046 (1)	0.046 (1)	0.025 (2)	-0.021 (2)	0.002 (1)	0.002 (1)

Table 4.34: $BaCuSi_2O_6$ at 640 K: thermal displacement parameters.

This high temperature structure model is very similar to the idealized centrosymmetric model suggested for the room temperature structure in [21].

In the high temperature phase, the CuO_4 group is a quasi perfect planar square, only surrounded by O2 atoms (Fig. 4.37). The Cu - O bond length is 1.934 (4) Å, the O - O distance 2.735 (6) Å, the O - Cu - O bond angle between two adjacent O atoms is per symmetry 90 °, and the diagonal O - Cu - O angle is 178.6 (3) °: The Cu atom is slightly out of the perfect square formed by the O2 atoms.

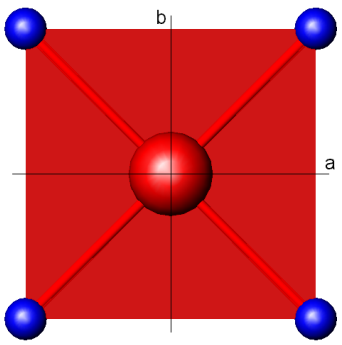

Figure 4.37: $BaCuSi_2O_6$ at 640 K: coordination of the Cu atom, projected onto the (**a**, **b**) plane.

The SiO_4 tetrahedra have become slightly more symmetrical (Fig. 4.38, Tab. 4.35): The bond length and angle distortions are smaller than at room temperature. The Si_4O_{10} rings have $4/mmm$ point symmetry (Fig. 4.39).

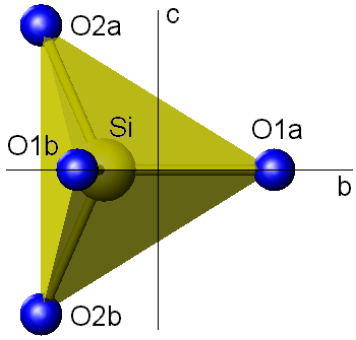

Figure 4.38: $BaCuSi_2O_6$ at 640 K: SiO_4 tetrahedron.

Distances (Å)		Angles (°)	
Si - O1	1.616 (1)	O1 - Si - O1	107.9 (4)
Si - O2	1.593 (4)	O1 - Si - O2	108.1 (1)
O1 - O1	2.612 (9)	O2 - Si - O2	116.6 (3)
O1 - O2	2.596 (4)		
O2 - O2	2.711 (8)		

Table 4.35: $BaCuSi_2O_6$ at 640 K: bond lengths and angles in the SiO_4 tetrahedron.

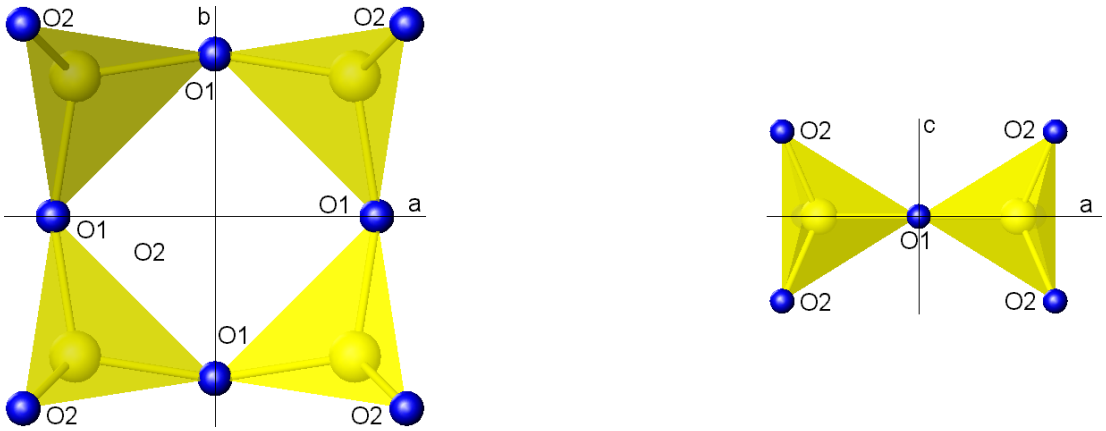

Figure 4.39: Si_4O_{12} rings at 640 K. Left: projection onto the (**a**, **b**) plane. Right: projection onto the (**a**, **c**) plane.

Discussion of the symmetry change upon the phase transition

The group-subgroup relationship between the high temperature space group $I4/mmm$ and the low temperature space group $I4_1/acd$ is a chain of maximal non-isomorphic subgroups, described in figure 4.40. $P4_2/nnm$ (No. 134) is a maximal non-isomorphic subgroup of $I4/mmm$ (decentric case, IIa). $F4_1/ddc$ is a maximal non-isomorphic subgroup of $P4_2/nnm$ (enlargement case, IIb), with a doubling of all the cell parameters: $\boldsymbol{a'} = 2\boldsymbol{a}$, $\boldsymbol{b'} = 2\boldsymbol{b}$ and $\boldsymbol{c'} = 2\boldsymbol{c}$. However, the space group $F4_1/ddc$ is equivalent to the standard space group $I4_1/acd$, with the choice of the unit cell vectors $\boldsymbol{a''} = \frac{1}{2}(\boldsymbol{a'} + \boldsymbol{b'})$, $\boldsymbol{b''} = \frac{1}{2}(\boldsymbol{b'} - \boldsymbol{a'})$ and $\boldsymbol{c''} = \boldsymbol{c'}$.

According to the Landau theory, a group-subgroup relationship is a necessary (but not sufficient) condition for a second order phase transition. On the other hand, first order phase transitions are accompagnied by a change in the volume of the unit cell. A de-

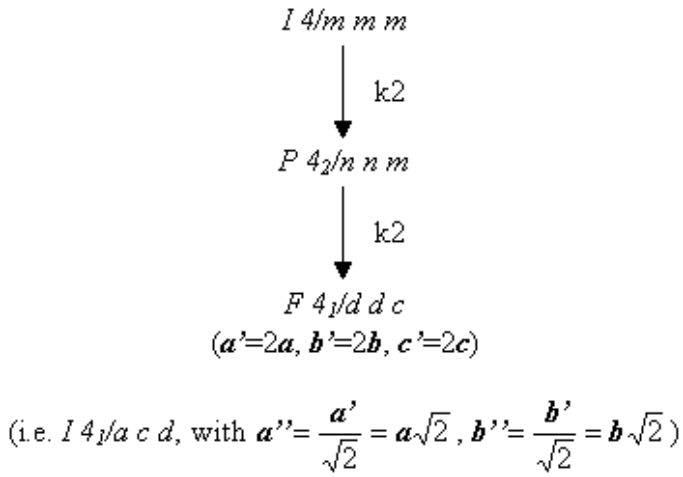

Figure 4.40: Relationship between the high and low temperature space groups $I4/mmm$ and $I4_1/acd$.

tailled investigation of the internal structural parameters would be useful to determine the order of the phase transition.
Since the phase transition at 610 K only involves class equivalent group-subgroup relationships, it doesn't lead to the formation of twin domains but antiphase domains at lower temperatures. These antiphase domains can't be observed by means of X-ray diffraction, but they should be evidenced by electron microscopy.

4.7 Conclusion

At room temperature, we discovered many very weak superstructure reflections in the diffraction pattern of $BaCuSi_2O_6$ that lead to a unit cell four times bigger than the one published in [21]. Our structural model deviates from it mainly by the rotation of the oxygen atoms around the 4-fold rotation axis, which explains the weakness of the intensities of the superstructure reflections.
In order to gain more accuracy on the positions of the atoms and to verify that the room temperature space group is really $I4_1/acd$ instead of $I4_1cd$, a neutron diffraction experiment would be necessary, since the simulated ratio between the intensities of the superstructure and main reflections would be five times larger than for an X-ray diffraction measurement. Unfortunately, no large enough single crystals of $BaCuSi_2O_6$ are available. Our japanese collaborators (K. Uchinokura et al.) are currently working on the growth of such crystals but haven't succeeded yet.
The results from Raman spectroscopy experiments presented in section 4.2, page 73, interpreted with the crystallographic models of the average structure, should then be reviewed taking into account the superstructure. In particular, the point symmetry of

the isolated Si_4O_{12} rings changes from $2mm$ in the $I\bar{4}m2$ average model to 2.. in the $I4_1cd$ and $I4_1/acd$ models.
At 610 K, $BaCuSi_2O_6$ undergoes a structural phase transition, from the low temperature space group $I4_1/acd$ to the high temperature space group $I4/mmm$, with a unit cell volume divided by four. In fact, the structural model in the high temperature phase is the same as the centrosymmetric model proposed for the room temperature average structure in [21] and [24].

Chapter 5

$Li_6CuB_4O_{10}$

5.1 Room temperature structure

We have measured a very small single crystal of $Li_6CuB_4O_{10}$ (about $100\,\mu m^3$) on the Stoe-IPDS-I diffractometer at room temperature. The conditions of the experiment are given in table 5.1.

U (kV)	I (mA)	φ - range (°)	$\Delta\varphi$ (°)	d (mm)	2θ - range (°)	t (mn)
50	25	0 - 270.4	0.8	80	2.9 - 48.4	6

Table 5.1: Conditions of the first measurement of $Li_6CuB_4O_{10}$ with the Stoe-IPDS-I diffractometer.

5.1.1 Determination of the cell parameters

From the indexation of the diffracted intensities, it appeared that $Li_6CuB_4O_{10}$ crystallizes in the triclinic system, with the cell parameters

$$a = 4.833\,(1)\,\text{Å},\ b = 9.240\,(2)\,\text{Å},\ c = 14.008\,(3)\,\text{Å},$$
$$\alpha = 104.33\,(2)\,°, \beta = 96.37\,(2)\,°, \gamma = 94.59\,(2)\,° \quad (V = 598.6\,(4)\,\text{Å}^3)$$

However, we noticed that one third of the reflections were significantly stronger than the rest of the data set (Fig. 5.1), so that this cell seems to result from the trippling of another cell (subcell), having the lattice parameters

$$a' = 4.838\,(3)\,\text{Å},\ b' = 6.509\,(5)\,\text{Å},\ c' = 7.032\,(5)\,\text{Å},$$
$$\alpha' = 83.44\,(9)\,°, \beta' = 71.82\,(7)\,°, \gamma' = 72.97\,(7)\,° \quad (V' = 202.0\,(6)\,\text{Å}^3)$$

Both cells have the same **a** vector in common, but they differ in the lengths and directions of the **b** and **c** vectors (Fig. 5.2). They are related by the following idealized

equation:

$$(\mathbf{a}' \quad \mathbf{b}' \quad \mathbf{c}') = \begin{pmatrix} 1 & 0 & 0 \\ \frac{1}{3} & \frac{1}{3} & \frac{1}{3} \\ \frac{1}{3} & \frac{2}{3} & \frac{1}{3} \end{pmatrix} \begin{pmatrix} \mathbf{a} \\ \mathbf{b} \\ \mathbf{c} \end{pmatrix}$$

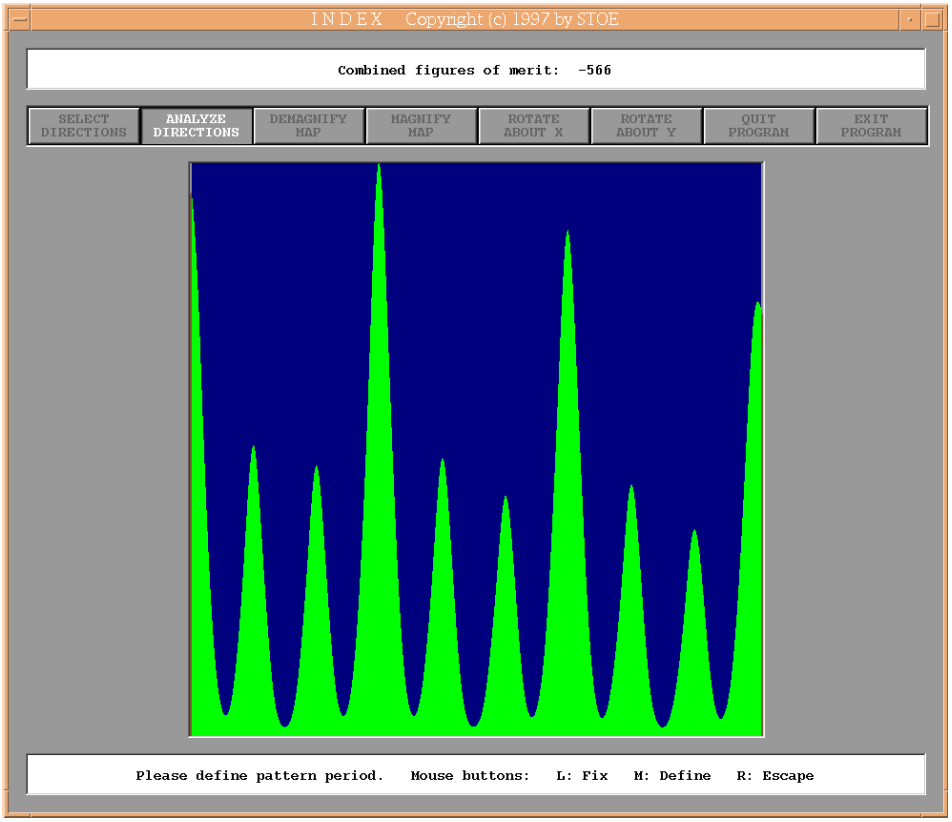

Figure 5.1: $Li_6CuB_4O_{10}$: the "superstructure" reflections.

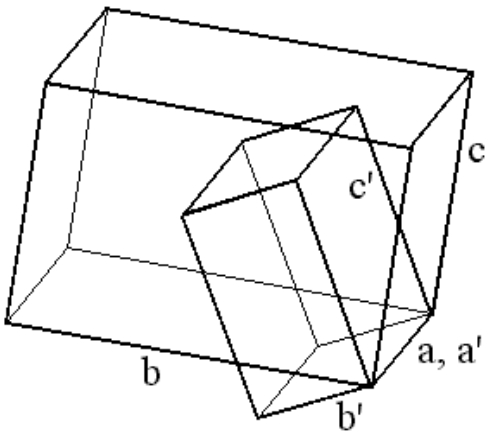

Figure 5.2: Mutual orientation of the unit cell and the subcell of $Li_6CuB_4O_{10}$.

5.1.2 Determination of the structure

• The stoichiometry of the compound was not known at the beginning, but the rather small scattering intensities indicated that neither Sr nor Ba were present (see section 2.3, page 17). We then supposed that the material could contain Cu, O, B and Li, as it was grown under $LiBO_3$ - flux. No absorption correction was then performed.
Our attempts to find solutions via direct methods (programs SIR97, SHELXS) in the space groups $P1$ and $P\bar{1}$ failed.

• The structure was first solved in the space group $P1$ (No. 1).
Using Patterson maps, six very high peaks were found, corresponding to the distances between the Cu atoms. Hence, the unit cell contains three Cu atoms.
The choice of the origin being of no importance in the space group $P1$, one Cu atom was fixed at $(0, 0, 0)$, and the other two ones were placed at positions corresponding to the distances indicated by the Patterson maps. The structure was then refined with only the three Cu atoms, and the peaks in the difference Fourier maps (listed in the SHELXL output file with their distances to the atoms) were examined.

The usual Cu - O distance being between 1.9 Å and 2.1 Å, the oxygen atoms around the Cu atoms could be found. The next refinement with the Cu and O atoms allowed to find some B and Li atoms, and by repeating this procedure, the structure could almost be completely solved. The program CAMERON, included in the package WINGX, was also used to see graphic representations in the unit cell of the atoms and Fourier peaks: It appeared that the B and O atoms form B_2O_5 groups around CuO_4 groups.
We then noticed that, apart from the Cu atom in $(0, 0, 0)$, the atoms could mostly be arranged in pairs that are related to each other by an inversion center.
The use of this "symmetry" element, combined together with the consideration of chemical configurations and of the electroneutrality of the crystal, made it possible to find all the atoms in the unit cell: three Cu atoms, eighteen Li atoms, twelve B atoms and thirty O atoms.
The compound formula is thus $Li_6CuB_4O_{10}$, with $Z = 3$.

The structure was then refined using the same isotropic thermal displacement parameter for all the Li and B atoms, and both atoms in an oxygen pair, except for the Cu atoms that were refined anisotropically, leading to 216 adjustable parameters. However, the results are not very satisfying, since some major axis components of the thermal tensors tend to zero or are almost non positive definite, and the positions of some Li atoms were quite unstable. The R - values are $R1 = 6.57\,\%$ for 1990 unique reflections with F_{obs} ¿ $4\,\sigma_{F_{obs}}$, $R1 = 11.84\,\%$ for all 3370 data, $wR2 = 9.02\,\%$, and the goodness of fit $GooF = 2.09$.

• Because of the very probable presence of an inversion centre, the structure was then refined in the space group $P\bar{1}$ (No. 2). The determination of a start model for the refinement in $P\bar{1}$ was straightforward, since the atoms were already arranged in more or less symmetric pairs with respect to the point $(0, 0, 0)$.

The results of the refinement (Tab. 5.2, 5.3, 5.4 and 5.5) show that this space group is the correct one to describe the room temperature structure of $Li_6CuB_4O_{10}$. We used the same isotropic thermal displacement parameter for all the Li and B atoms. There wasn't any problem of convergence for the positions of the Li atoms and the thermal displacement parameters have more reasonnable values. For a total of 123 adjustable parameters, the R - values are R1 = 5.94 % for 1115 unique reflections with F_{obs} ¿ $4\,\sigma_{F_{obs}}$, R1 = 9.09 % for all 1721 data, wR2 = 8.83 %, and the goodness of fit GooF = 2.04.

Atom	x	y	z	Atom	x	y	z
Cu1	0	0	0	Cu2	0.2996 (3)	0.3166 (2)	0.6706 (1)
B1	0.082 (2)	0.453 (1)	0.332 (1)	B2	0.170 (2)	0.686 (1)	0.482 (1)
B3	0.207 (2)	0.656 (1)	0.182 (1)	B4	0.275 (2)	0.891 (1)	0.334 (1)
B5	0.414 (2)	0.776 (1)	0.996 (1)	B6	0.462 (3)	0.002 (1)	0.148 (1)
Li1	0.032 (4)	0.804 (2)	0.816 (1)	Li2	0.067 (4)	0.373 (2)	0.031 (1)
Li3	0.083 (3)	0.087 (2)	0.813 (1)	Li4	0.216 (3)	0.945 (2)	0.632 (1)
Li5	0.337 (4)	0.138 (2)	0.487 (1)	Li6	0.363 (3)	0.433 (2)	0.912 (1)
Li7	0.384 (3)	0.180 (2)	0.313 (1)	Li8	0.444 (3)	0.563 (2)	0.601 (1)
Li9	0.498 (3)	0.398 (2)	0.193 (1)				
O1	0.030 (1)	0.591 (1)	0.1016 (5)	O2	0.063 (1)	0.259 (1)	0.5454 (5)
O3	0.113 (1)	0.786 (1)	0.2507 (5)	O4	0.160 (1)	0.807 (1)	0.9530 (5)
O5	0.161 (1)	0.024 (1)	0.3579 (5)	O6	0.185 (1)	0.526 (1)	0.6990 (5)
O7	0.191 (1)	0.031 (1)	0.1317 (5)	O8	0.217 (1)	0.340 (1)	0.2814 (5)
O9	0.238 (1)	0.545 (1)	0.4203 (5)	O10	0.352 (1)	0.749 (1)	0.5613 (5)
O11	0.354 (1)	0.927 (1)	0.7736 (5)	O12	0.439 (1)	0.122 (1)	0.9189 (5)
O13	0.472 (1)	0.132 (1)	0.6252 (5)	O14	0.472 (1)	0.353 (1)	0.0425 (5)
O15	0.458 (1)	0.619 (1)	0.2059 (4)				

Table 5.2: $Li_6CuB_4O_{10}$ at room temperature: atomic positions (space group $P\bar{1}$).

Atom	U_{11} (Å^2)	U_{22} (Å^2)	U_{33} (Å^2)	U_{12} (Å^2)	U_{13} (Å^2)	U_{23} (Å^2)
Cu1	0.008 (1)	0.013 (1)	0.009 (1)	0.006 (1)	-0.002 (1)	-0.002 (1)
Cu2	0.0109 (8)	0.0165 (8)	0.0081 (7)	0.0130 (4)	-0.0037 (6)	-0.0040 (6)

Table 5.3: $Li_6CuB_4O_{10}$: anisotropic thermal displacement parameters for the Cu atoms.

Atom	Li	B
U_{eq} (Å^2)	0.016 (1)	0.0088 (7)

Table 5.4: $Li_6CuB_4O_{10}$: isotropic thermal displacement parameters for the Li and B atoms.

Atom	U_{eq} (Å^2)	Atom	U_{eq} (Å^2)	Atom	U_{eq} (Å^2)
O1	0.011 (2)	O2	0.018 (2)	O3	0.012 (2)
O4	0.009 (2)	O5	0.011 (2)	O6	0.013 (2)
O7	0.010 (1)	O8	0.011 (2)	O9	0.013 (2)
O10	0.016 (2)	O11	0.012 (2)	O12	0.011 (2)
O13	0.012 (2)	O14	0.016 (2)	O15	0.007 (1)

Table 5.5: $Li_6CuB_4O_{10}$: isotropic thermal displacement parameters for the O atoms.

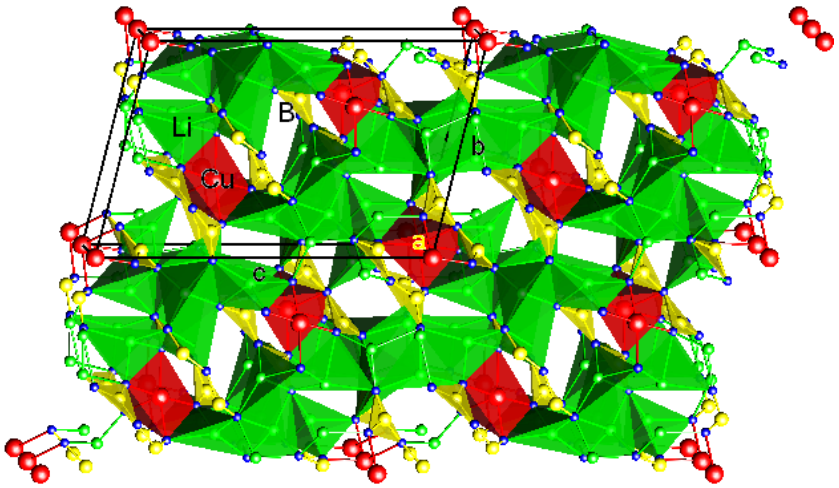

Figure 5.3: Room temperature structure of $Li_6CuB_4O_{10}$ ($P\bar{1}$).

5.1.3 Discussion of the solution

A new measurement was performed with a 0.06 × 0.12 × 0.32 mm^3 single crystal of $Li_6CuB_4O_{10}$ (grown by Dr. G. Redhammer) on the Stoe-IPDS-I diffractometer at room temperature, with the conditions given in table 5.6. The internal R - value of the data set after the (necessary) absorption correction is 3.43 %.

U (kV)	I (mA)	φ - range (°)	$\Delta\varphi$ (°)	d (mm)	2θ - range (°)	t (mn)
50	25	0 - 217.0	1.5	60	3.8 - 56.3	3

Table 5.6: Conditions of the second measurement with the Stoe-IPDS-I diffractometer.

Atom	x	y	z	Atom	x	y	z
Cu1	0	0	0	Cu2	0.2979 (1)	0.31561 (5)	0.67025 (4)
B1	0.0805 (8)	0.4516 (4)	0.3307 (4)	B2	0.1713 (8)	0.6850 (4)	0.4798 (4)
B3	0.2017 (8)	0.6593 (4)	0.1833 (3)	B4	0.2759 (8)	0.8937 (4)	0.3325 (4)
B5	0.4130 (8)	0.7744 (4)	0.9935 (4)	B6	0.4620 (8)	-0.0013 (5)	0.1459 (4)
Li1	0.045 (1)	0.8030 (7)	0.8151 (6)	Li2	0.067 (1)	0.3792 (7)	0.0325 (6)
Li3	0.088 (1)	0.0804 (7)	0.8115 (6)	Li4	0.212 (1)	0.9383 (7)	0.6324 (6)
Li5	0.332 (1)	0.1401 (7)	0.4874 (6)	Li6	0.369 (1)	0.4315 (6)	0.9127 (5)
Li7	0.384 (1)	0.1718 (7)	0.3108 (6)	Li8	0.437 (1)	0.5690 (7)	0.6025 (5)
Li9	0.495 (1)	0.4039 (7)	0.1965 (5)				
O1	0.0276 (5)	0.5911 (3)	0.1005 (2)	O2	0.0616 (5)	0.2567 (3)	0.5464 (2)
O3	0.1136 (5)	0.7841 (3)	0.2502 (2)	O4	0.1614 (5)	0.8067 (3)	0.9531 (2)
O5	0.1611 (5)	0.0239 (3)	0.3578 (2)	O6	0.1866 (5)	0.5240 (3)	0.6972 (2)
O7	0.1904 (5)	0.0312 (3)	0.1321 (2)	O8	0.2187 (5)	0.3408 (3)	0.2808 (2)
O9	0.2401 (5)	0.5460 (3)	0.4199 (2)	O10	0.3565 (5)	0.7486 (3)	0.5624 (2)
O11	0.3514 (5)	0.9267 (3)	0.7736 (2)	O12	0.4375 (5)	0.1213 (3)	0.9199 (2)
O13	0.4707 (5)	0.1295 (3)	0.6254 (2)	O14	0.4711 (5)	0.3528 (3)	0.0422 (2)
O15	0.4593 (5)	0.6170 (3)	0.2065 (2)				

Table 5.7: $Li_6CuB_4O_{10}$ at room temperature: atomic positions ($P\bar{1}$).

Atom	U_{11} (Å^2)	U_{22} (Å^2)	U_{33} (Å^2)	U_{12} (Å^2)	U_{13} (Å^2)	U_{23} (Å^2)
Cu1	0.0047 (3)	0.0048 (3)	0.0026 (4)	0.0034 (3)	-0.0016 (3)	-0.0013 (3)
Cu2	0.0054 (2)	0.0041 (2)	0.0026 (3)	0.0041 (2)	-0.0031 (2)	-0.0025 (2)

Table 5.8: $Li_6CuB_4O_{10}$: anisotropic thermal displacement parameters for the Cu atoms.

Atom	U_{eq} (Å^2)	Atom	U_{eq} (Å^2)	Atom	U_{eq} (Å^2)
B1	0.0029 (8)	B2	0.0043 (8)	B3	0.0024 (8)
B4	0.0026 (8)	B5	0.0029 (9)	B6	0.0033 (8)
Li1	0.009 (1)	Li2	0.011 (1)	Li3	0.019 (1)
Li4	0.009 (1)	Li5	0.010 (1)	Li6	0.012 (1)
Li7	0.014 (1)	Li8	0.015 (1)	Li9	0.012 (1)
O1	0.0064 (6)	O2	0.0091 (6)	O3	0.0036 (5)
O4	0.0061 (6)	O5	0.0045 (5)	O6	0.0061 (5)
O7	0.0036 (5)	O8	0.0046 (5)	O9	0.0056 (6)
O10	0.0057 (6)	O11	0.0048 (6)	O12	0.0054 (6)
O13	0.0053 (6)	O14	0.0051 (6)	O15	0.0027 (5)

Table 5.9: $Li_6CuB_4O_{10}$: isotropic thermal displacement parameters for the Li, B and O atoms.

The aim of this new measurement with a bigger crystal was to improve the statistics on the weaker intensities in order to get more reliable structural informations.
The obtained cell parameters are

$$a = 4.858\,(1)\,\text{Å},\ b = 9.288\,(2)\,\text{Å},\ c = 14.019\,(3)\,\text{Å},$$
$$\alpha = 104.36\,(2)\,°, \beta = 95.98\,(3)\,°, \gamma = 94.93\,(3)\,° \quad (V = 605.3\,(5)\,\text{Å}^3)$$

The results are given in tables 5.7, 5.8 and 5.9. The structure was refined with individual thermal parameters for all the atoms. The obtained R - values (136 parameters) are R1 = 3.53 % for 1882 unique reflections with F_{obs} ¿ $4\,\sigma_{F_{obs}}$, R1 = 5.93 % for all 2662 data, wR2 = 5.41 %, and the goodness of fit GooF = 1.63.
The structure of $Li_6CuB_4O_{10}$ thus consists of CuO_4 distorted squares, surrounded by two B_2O_5 groups and two LiO_4 tetrahedra.
The Li atoms are coordinated by four oxygen atoms. Some sit in quite distorted tetrahedra (Li2, Li3, Li5, Li6, Li7), the others are in triangular pyramids (Li1, Li4, Li8, Li9). The Li - O bond lengths run from 1.887 (7) Å up to 2.163 (7) Å.
The B and O atoms form slightly distorted BO_3 equilateral triangles, with B - O bond lengths from 1.343 (5) Å up to 1.442 (5) Å, and O - B - O bond angles between 113.1 (3) ° and 125.6 (3) °.

The shortest Cu^{2+} - Cu^{2+} distance within the structure is a = 4.858 (1) Å, and the second shortest Cu^{2+} - Cu^{2+} distance is 6.281 (2) Å: There are only very weak magnetic interactions between the Cu^{2+} ions in $Li_6CuB_4O_{10}$.
The CuO_4 groups are surrounded by both two opposed B_2O_5 groups and two LiO_4 groups. Both CuO_4 groups are somewhat sheared and the $Cu2O_4$ group is highly non planar (Fig. 5.5 and 5.6, Tab. 5.11), although there is no strong chemical constraint imposed on them.

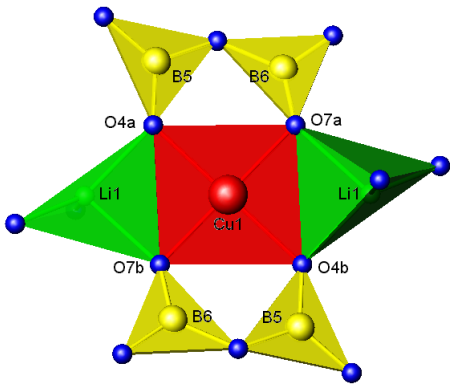

Figure 5.4: $Li_6CuB_4O_{10}$ (s.g. $P\bar{1}$): $Cu1O_4$ group.

Distances (Å)		Angles (°)	
Cu1 - O4a	2.009 (3)	O4a - Cu1 - O7a	91.6 (1)
Cu1 - O7a	1.923 (3)	O4a - Cu1 - O4b	180.0 (0)
O4a - O7a	2.819 (4)	O7a - Cu1 - O4b	88.4 (1)
O7a - O4b	2.742 (4)	O7a - Cu1 - O7b	180.0 (0)

Table 5.10: $Li_6CuB_4O_{10}$ (s.g. $P\bar{1}$): bond lengths and angles in the $Cu1O_4$ group.

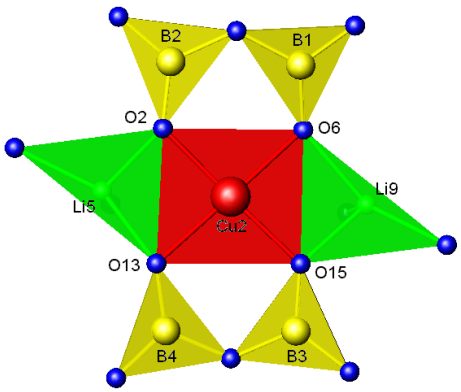

Figure 5.5: $Li_6CuB_4O_{10}$ (s.g. $P\bar{1}$): $Cu2O_4$ group.

Distances (Å)		Angles (°)	
Cu2 - O2	1.907 (3)	O2 - Cu2 - O6	91.4 (1)
Cu2 - O6	2.010 (3)	O6 - Cu2 - O15	86.7 (1)
Cu2 - O15	1.918 (3)	O15 - Cu2 - O13	94.3 (1)
Cu2 - O13	1.977 (3)	O13 - Cu2 - O2	87.1 (1)
O2 - O6	2.806 (4)	O2 - Cu2 - O15	177.4 (1)
O6 - O15	2.697 (4)	O6 - Cu2 - O13	166.3 (1)
O15 - O13	2.855 (4)		
O13 - O2	2.677 (4)		

Table 5.11: $Li_6CuB_4O_{10}$ (s.g. $P\bar{1}$): bond lengths and angles in the $Cu2O_4$ group.

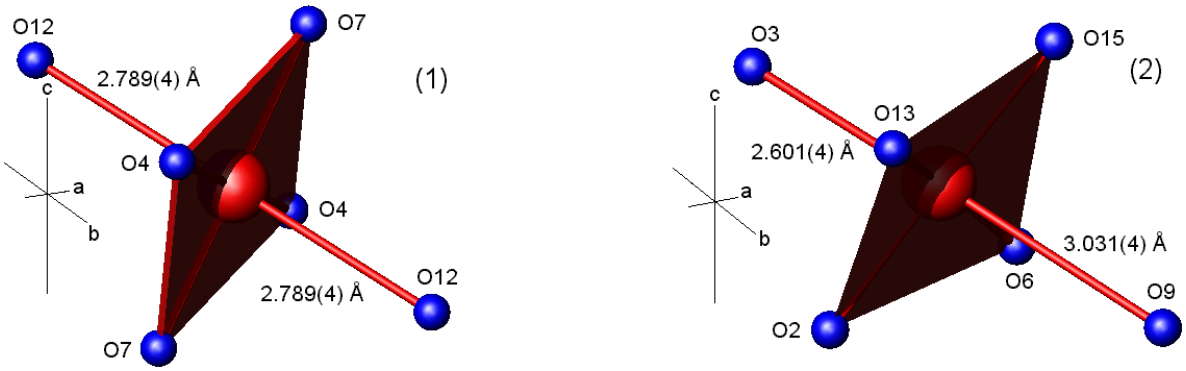

Figure 5.6: Oxygen coordination of the Cu1 atom (1) and Cu2 atom (2).

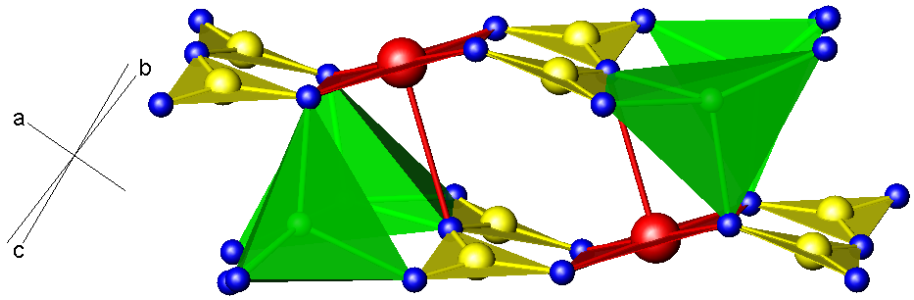

Figure 5.7: Linkage between the Cu^{2+} ions.

In fact, a closer look at the Cu - O distances reveals that around each CuO_4 group, there are some other oxygen atoms that could be considered as ligands (Fig. 5.6):
$|Cu1 - O_{12}| = 2.789\,(4)$ Å and $|Cu2 - O_3| = 2.601\,(4)$ Å.
However, a charge distribution calculation, performed with the program CHARD-IT [64], showed that both Cu atoms are four-fold coordinated.

In the a direction, the Cu atoms are linked by B_2O_5 groups and LiO_4 pyramids. Any magnetic interaction by superexchange would have to be via quite a long path: Cu - O - B - O - Li - O - Cu (Fig. 5.7).

5.2 $Li_6CuB_4O_{10}$ from 100 K up to room temperature

The same single crystal was measured on the Stoe-IPDS-II diffractometer at 100 K, 150 K, 200 K, 250 K and 290 K, with the conditions given in table 5.12. The internal R - values of the data sets after absorption correction range between 4.17 % and 4.91 %.

U (kV)	I (mA)	φ (°)	ω - range (°)	$\Delta\omega$ (°)	d (mm)	2θ - range (°)	t (mn)
50	20	270	0 - 180.0	1.5	80	2.86 - 64.8	2.5
50	20	180	70 - 119.5	1.5	80	2.86 - 64.8	2.5

Table 5.12: Conditions of the measurements at low temperatures with the Stoe-IPDS-II diffractometer.

$Li_6CuB_4O_{10}$ doesn't undergo any structural phase transition from 100 K up to room temperature. The intensitiy ratio between the "main" and "superstructure" reflection becomes closer to 1 at lower temperature, which reinforces the idea of a structural phase transition at high temperatures.
The temperature dependences of the cell parameters and volume are shown in figure 5.8. Whereas the thermal expansions along a and b have normal values ($\alpha_{11} \approx \alpha_{22} \approx 5.3(6) \cdot 10^{-5}$ Å·K^{-1}), the one along c is much higher ($\alpha_{33} = 28.1(9) \cdot 10^{-5}$ Å·K^{-1}). We noticed that the angles β and γ, whose values are close to 96 °, show opposite behaviours as the temperature increases.

The results of the refinement at 100 K (program SHELXL) are given in tables 5.13, 5.14 and 5.15. The obtained R - values (137 parameters) are R1 = 3.64 % for 3265 unique reflections with F_{obs} ¿ 4 $\sigma_{F_{obs}}$, R1 = 4.88 % for all 3935 data, wR2 = 5.26 %, and the goodness of fit GooF = 2.01. There is one more refined parameter than at room temperature, because extinction effects have to be taken into account for the low temperature data below 250 K.

Atom	x	y	z	Atom	x	y	z
Cu1	0	0	0	Cu2	0.29745 (5)	0.31522 (3)	0.67027 (2)
B1	0.0824 (5)	0.4519 (3)	0.3316 (2)	B2	0.1741 (5)	0.6855 (3)	0.4798 (2)
B3	0.2012 (5)	0.6594 (3)	0.1838 (2)	B4	0.2734 (5)	0.8936 (3)	0.3321 (2)
B5	0.4144 (5)	0.7740 (3)	0.9940 (2)	B6	0.4614 (5)	-0.0013 (3)	0.1466 (2)
Li1	0.0431 (8)	0.8045 (4)	0.8145 (3)	Li2	0.0632 (8)	0.3795 (5)	0.0332 (3)
Li3	0.0880 (8)	0.0805 (5)	0.8102 (3)	Li4	0.2133 (8)	0.9391 (5)	0.6312 (3)
Li5	0.3291 (8)	0.1394 (4)	0.4870 (3)	Li6	0.3708 (8)	0.4316 (4)	0.9133 (3)
Li7	0.3809 (8)	0.1706 (4)	0.3107 (3)	Li8	0.4402 (8)	0.5713 (5)	0.6031 (3)
Li9	0.4966 (8)	0.4038 (4)	0.1959 (3)				
O1	0.0286 (3)	0.5895 (2)	0.0999 (1)	O2	0.0584 (3)	0.2543 (2)	0.5464 (1)
O3	0.1117 (3)	0.7834 (2)	0.2504 (1)	O4	0.1621 (3)	0.8069 (2)	0.9528 (1)
O5	0.1603 (3)	0.0233 (2)	0.3571 (1)	O6	0.1868 (3)	0.5237 (2)	0.6966 (1)
O7	0.1917 (3)	0.0322 (2)	0.1323 (1)	O8	0.2190 (3)	0.3411 (2)	0.2812 (1)
O9	0.2420 (3)	0.5464 (2)	0.4206 (1)	O10	0.3589 (3)	0.7504 (2)	0.5630 (1)
O11	0.3508 (3)	0.9267 (2)	0.7731 (1)	O12	0.4353 (3)	0.1216 (2)	0.9196 (1)
O13	0.4704 (3)	0.1289 (2)	0.6254 (1)	O14	0.4710 (3)	0.3533 (2)	0.0425 (1)
O15	0.4599 (3)	0.6159 (2)	0.2066 (1)				

Table 5.13: $Li_6CuB_4O_{10}$ at room temperature: atomic positions ($P\bar{1}$).

Atom	U_{11} (Å^2)	U_{22} (Å^2)	U_{33} (Å^2)	U_{12} (Å^2)	U_{13} (Å^2)	U_{23} (Å^2)
Cu1	0.0041 (2)	0.0054 (2)	0.0018 (2)	0.0022 (1)	-0.0004 (1)	0.0001 (1)
Cu2	0.0038 (1)	0.0051 (1)	0.0018 (1)	0.0023 (1)	-0.0009 (1)	-0.0002 (1)

Table 5.14: $Li_6CuB_4O_{10}$: anisotropic thermal displacement parameters for the Cu atoms.

Atom	U_{eq} (Å^2)	Atom	U_{eq} (Å^2)	Atom	U_{eq} (Å^2)
B1	0.0052 (4)	B2	0.0046 (4)	B3	0.0048 (4)
B4	0.0048 (4)	B5	0.0046 (4)	B6	0.0049 (4)
Li1	0.0084 (7)	Li2	0.0095 (7)	Li3	0.0106 (7)
Li4	0.0090 (7)	Li5	0.0078 (7)	Li6	0.0083 (7)
Li7	0.0087 (7)	Li8	0.0110 (7)	Li9	0.0093 (7)
O1	0.0049 (3)	O2	0.0066 (3)	O3	0.0046 (3)
O4	0.0056 (3)	O5	0.0048 (3)	O6	0.0052 (3)
O7	0.0040 (3)	O8	0.0047 (3)	O9	0.0051 (3)
O10	0.0051 (3)	O11	0.0045 (3)	O12	0.0048 (3)
O13	0.0045 (3)	O14	0.0051 (3)	O15	0.0039 (3)

Table 5.15: $Li_6CuB_4O_{10}$: isotropic thermal displacement parameters for the Li, B and O atoms.

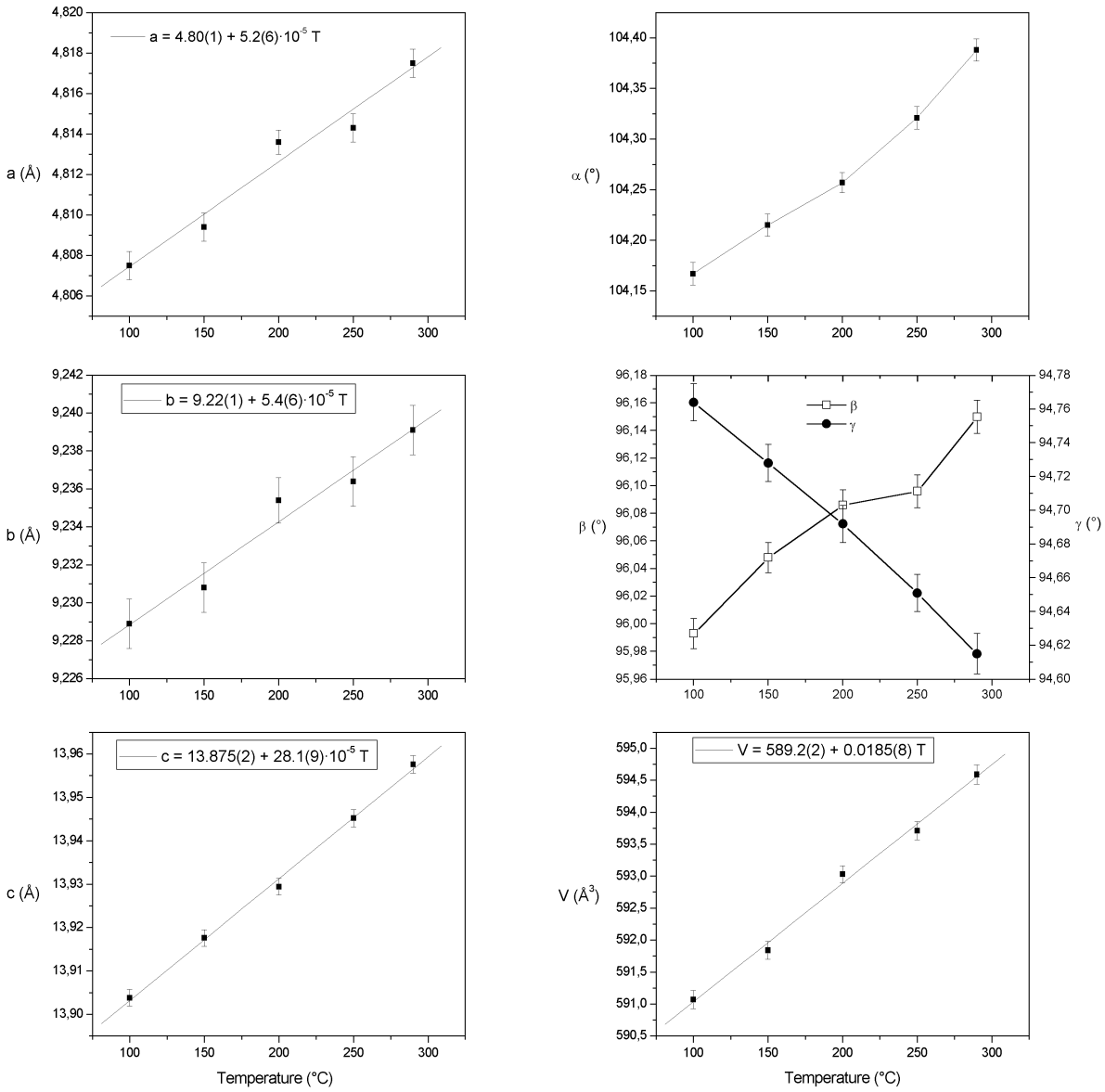

Figure 5.8: Evolution of the unit cell of $Li_6CuB_4O_{10}$ between 100 K and room temperature.

5.3 $Li_6CuB_4O_{10}$ at high temperatures

5.3.1 Differential scanning calorimetry measurements

Our differential scanning calorimetry (DSC) experiments (Fig. 5.9, 5.10, 5.11, 5.12, 5.13 and 5.14) show that, from room temperature up to the melting point at 850 °C, $Li_6CuB_4O_{10}$ undergoes three phase transitions, two reversible at 345 °C and 384 °C, and one possibly irreversible at 668 °C. At 850 °C, it melts incongruently in air and decomposes into two other phases, which are still to be identified.

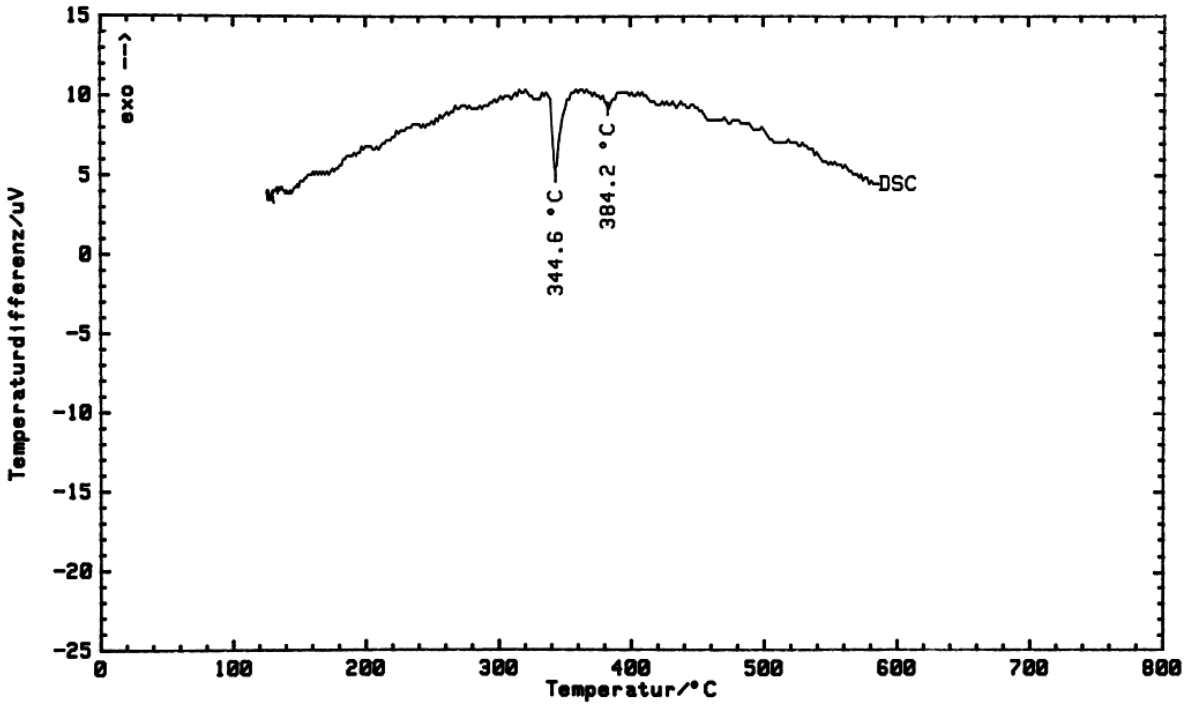

Figure 5.9: $Li_6CuB_4O_{10}$, DSC measurement: Heating from 150 °C up to 580 °C.

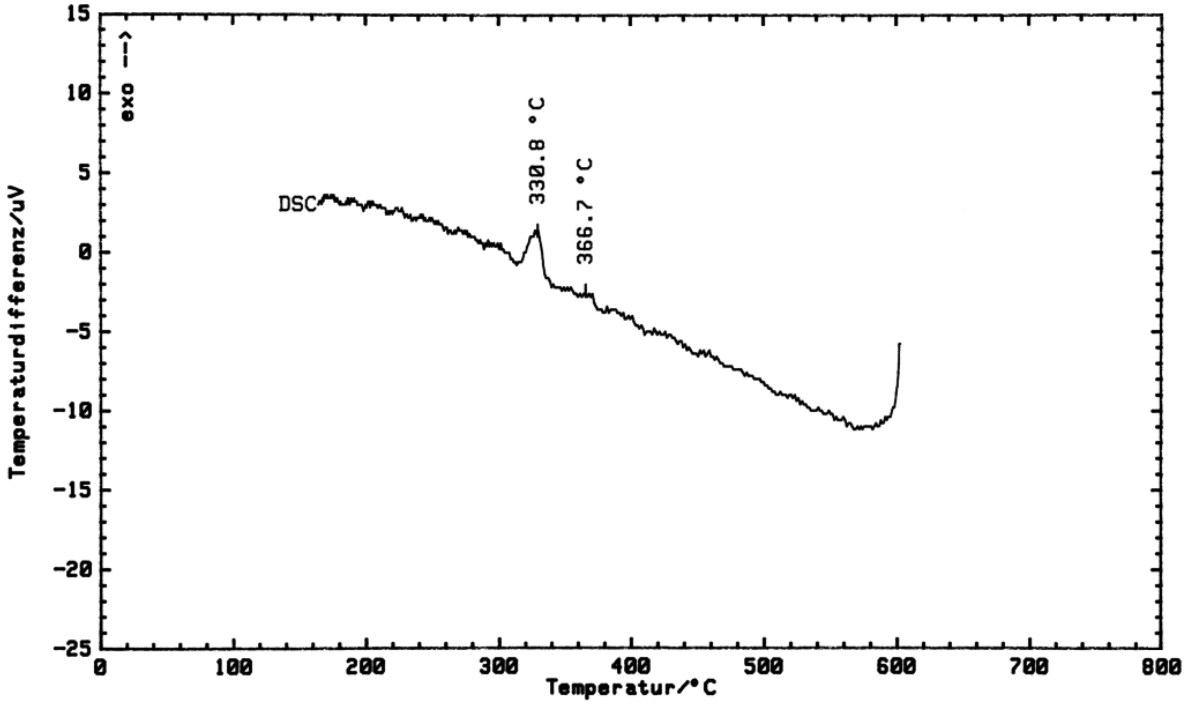

Figure 5.10: $Li_6CuB_4O_{10}$, DSC measurement: Cooling from 580 °C down to 170 °C.

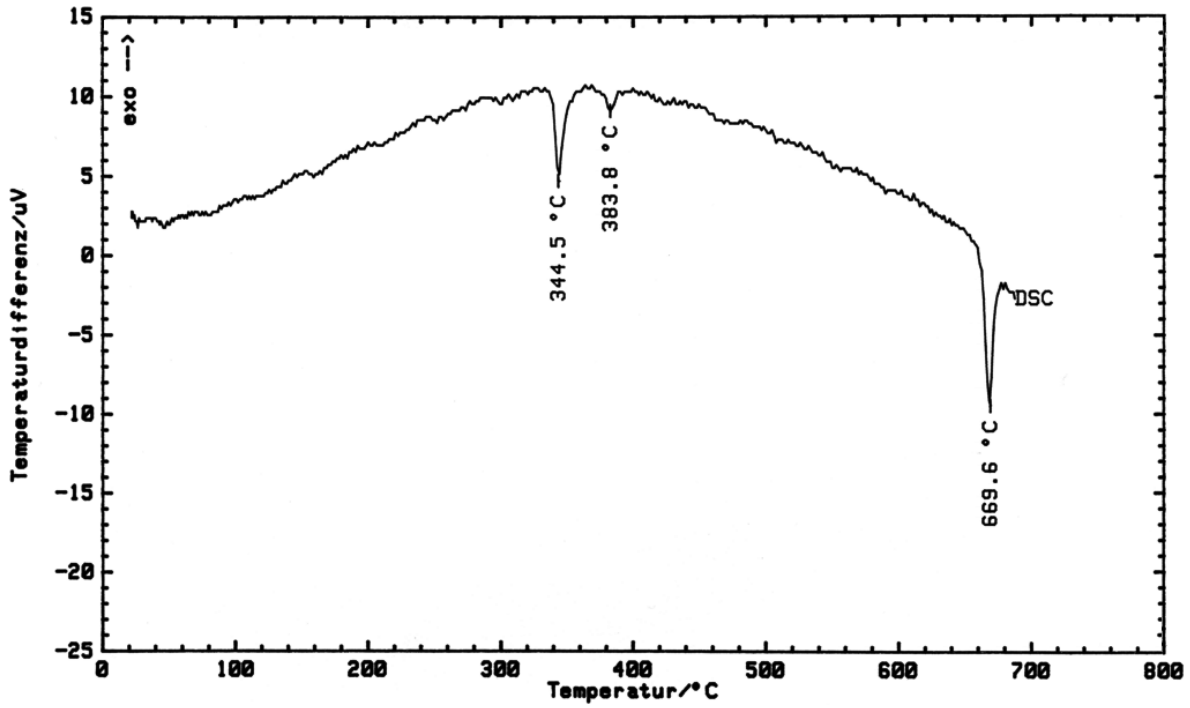

Figure 5.11: $Li_6CuB_4O_{10}$, DSC measurement: Heating from 20 °C up to 700 °C.

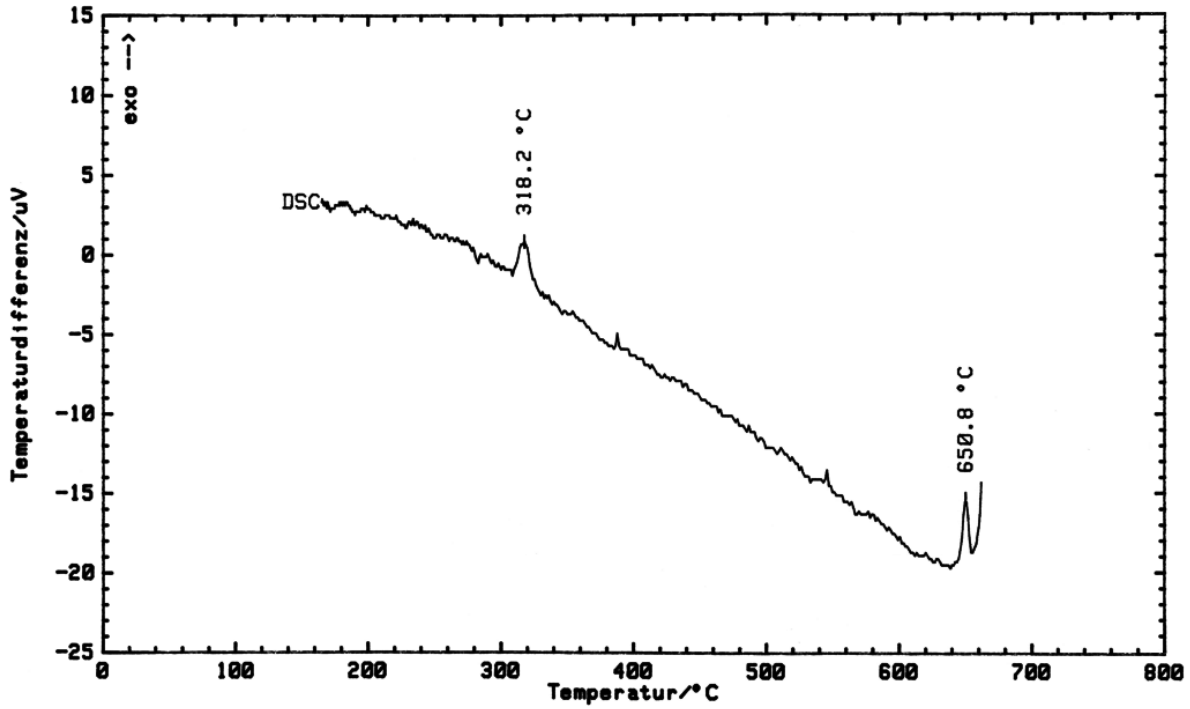

Figure 5.12: $Li_6CuB_4O_{10}$, DSC measurement: Cooling from 700 °C down to 170 °C.

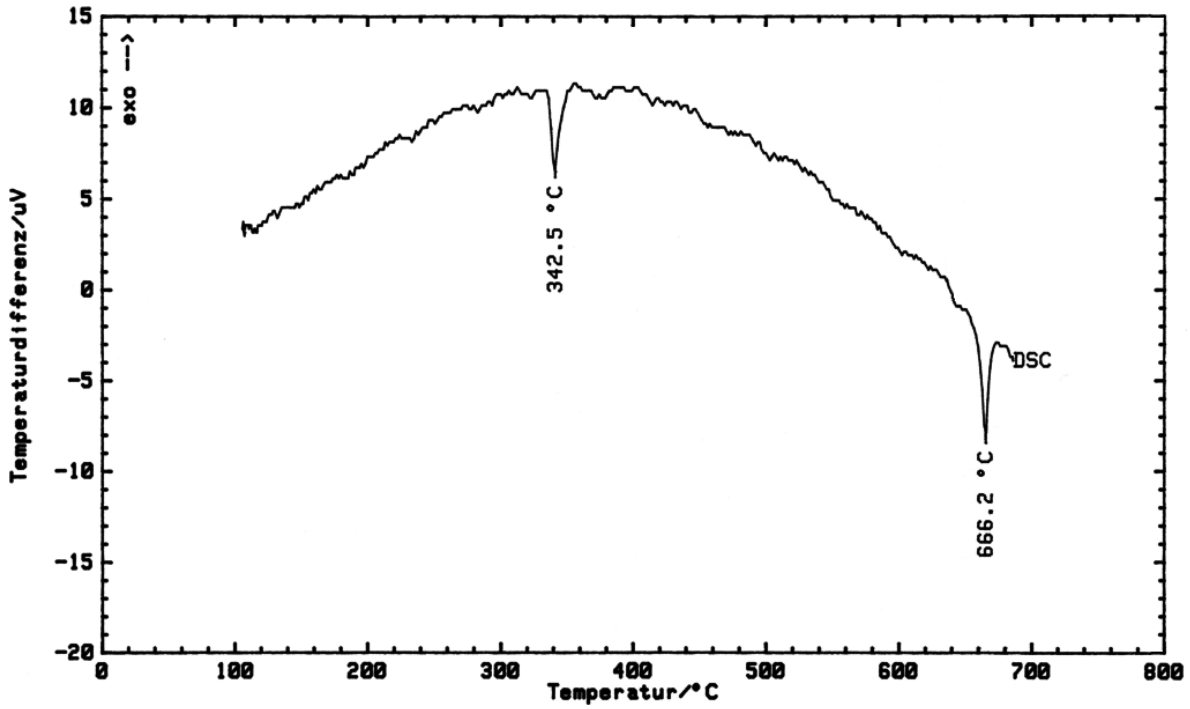

Figure 5.13: $Li_6CuB_4O_{10}$, DSC measurement: Second heating from 100 °C up to 700 °C.

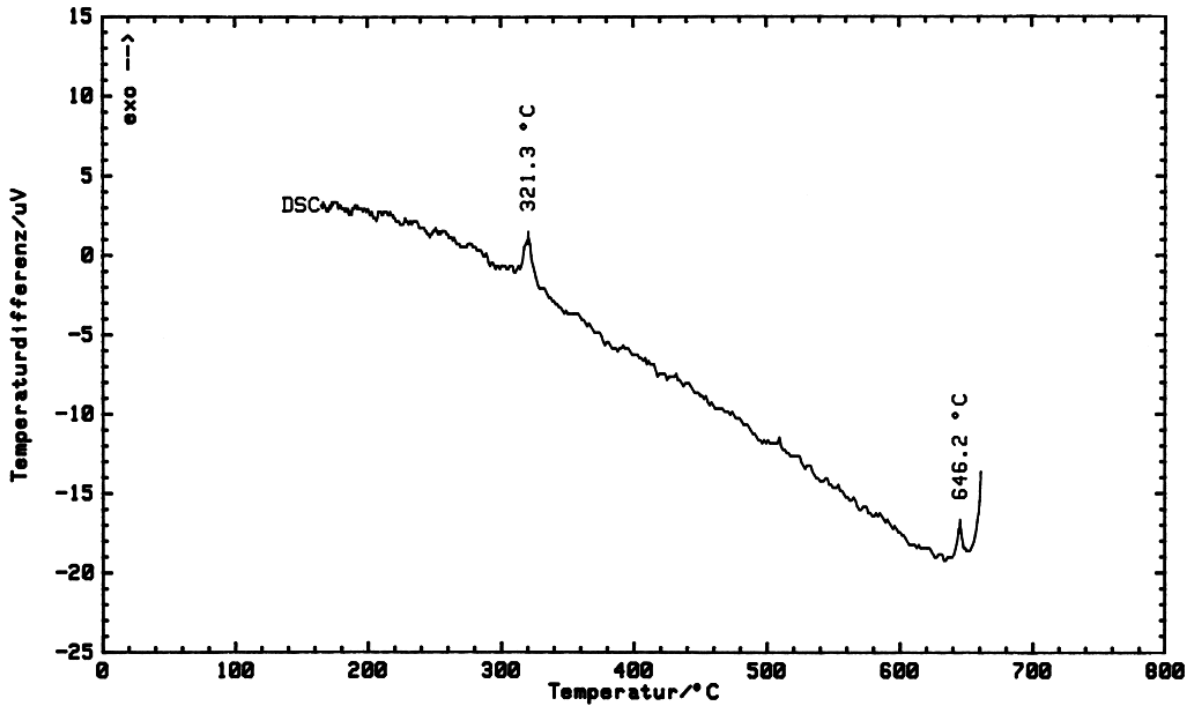

Figure 5.14: $Li_6CuB_4O_{10}$, DSC measurement: Second cooling from 700 °C down to 170 °C.

It is obvious that the phase transitions at 345 °C and 384 °C (Fig. 5.9 and 5.11) are reversible, since they appear on both heating curves at the same temperatures. The phase transition at 384 °C is not easily evidenced because it leads to very weak peaks, especially in the cooling curve (Fig. 5.10), but it was also observed by means of powder X-ray diffraction experiments. The systematic shift in the temperatures of the phase transitions observed between the heating and cooling curves (Fig. 5.9 and 5.10) is a normal phemonenon during DSC measurements.
On the other hand, the third phase transition at 668 °C (Fig. 5.11) would be an irreversible one: Its peak is narrower than the others, and the position of the first phase transition at 345 °C is significantly lowered in temperature on the following cooling curves (Fig. 5.12 and 5.14), so that it could be a transition to yet another phase. However, it still appears close to 345 °C in the heating curve (Fig. 5.13). Because of the weakness of the peak for the second phase transition at 384 °C, we can't state whether it is still present or not in figures 5.12, 5.13 and 5.14.
Powder and single crystal X-ray diffraction experiments are necessary to clarify the nature of those phase transitions.

5.3.2 X-ray powder diffraction

For in-situ lattice parameter determination at high temperatures, step-scan powder diffraction data were collected on a Philips X'Pert diffractometer system (Cu K$\alpha_{1,2}$ radiation, incident and diffracted beam soller slits, diffracted beam graphite monochromator, $\theta - \theta$ geometry), equipped with a Paar HTK-16 high temperature chamber. Powder diffraction diagrams were measured from room temperature up to 700 °C.
A thin film of the sample material, mixed with silicon as an internal standard, was smeared onto the platinum band, thus penetrating the whole sample and giving also rise to diffraction from the Pt band. In this way, platinum could also be used as an internal standard. A linear thermal expansion coefficient of $\alpha = 9.0 \times 10^{-6}\,K^{-1}$ [65] was used for Pt to calculate the lattice parameters of Pt at elevated temperatures. Lattice parameters were refined using Le-Bail whole pattern refinements as implemented in the program FULLPROF [29].

The three phase transitions detected by means of DSC between room temperature and the melting point were also found in the X-ray powder diffraction diagrams (Fig. 5.15, 5.16, 5.17 and 5.18), signified by the disappearance or shift of reflections in a narrow temperature range around the temperatures of the phase transitions.
The temperature evolution of the cell parameters can't be discussed yet: Single crystal diffraction experiments at high temperatures are needed to determine the correct unit cells for the different phases. These results will be presented in [66].

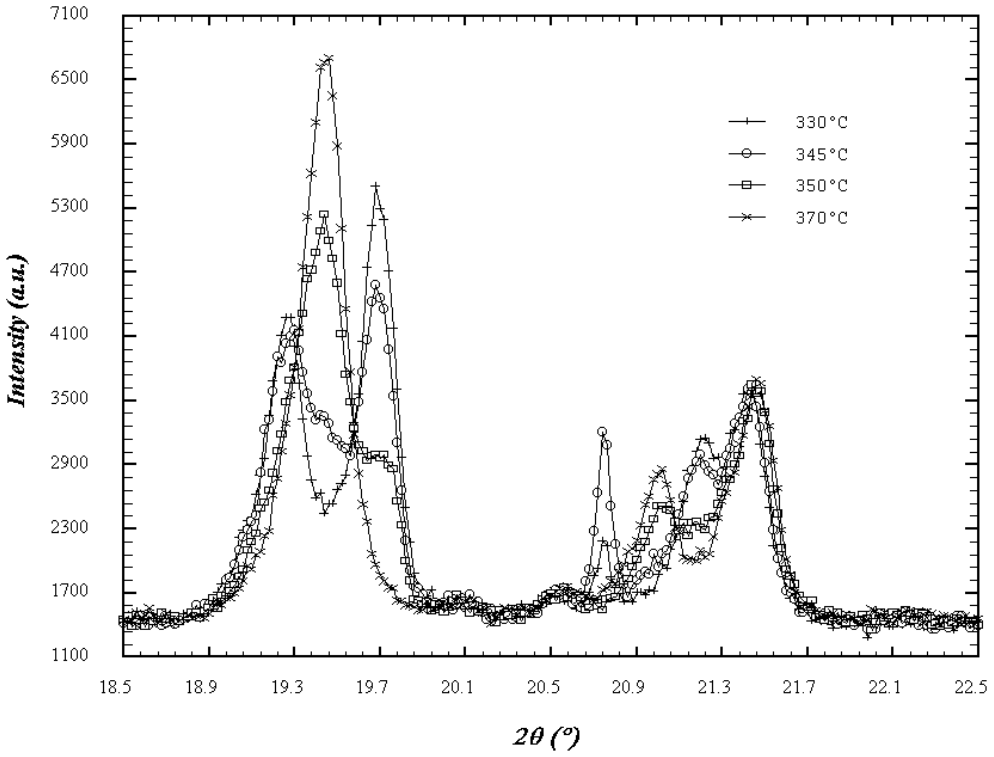

Figure 5.15: The phase transition at 345 °C: Powder diagram for $18.5° < 2\theta < 22.5°$. We have no explanation for the anomaly of the peak at 20.74 °.

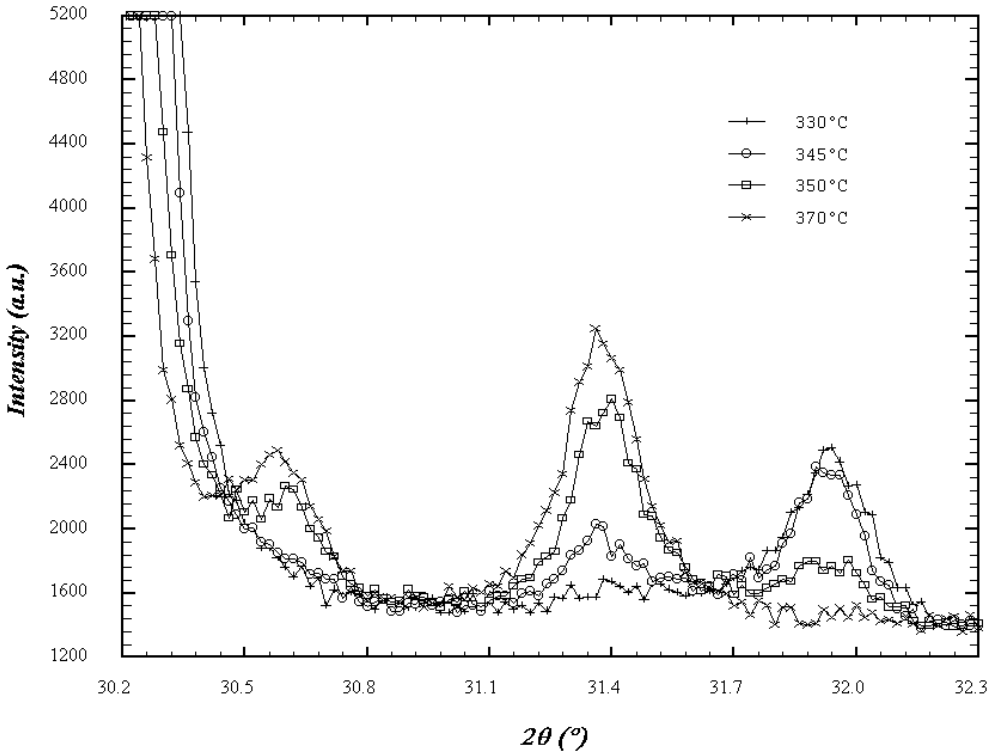

Figure 5.16: The phase transition at 345 °C: Powder diagram for $30.2° < 2\theta < 32.3°$.

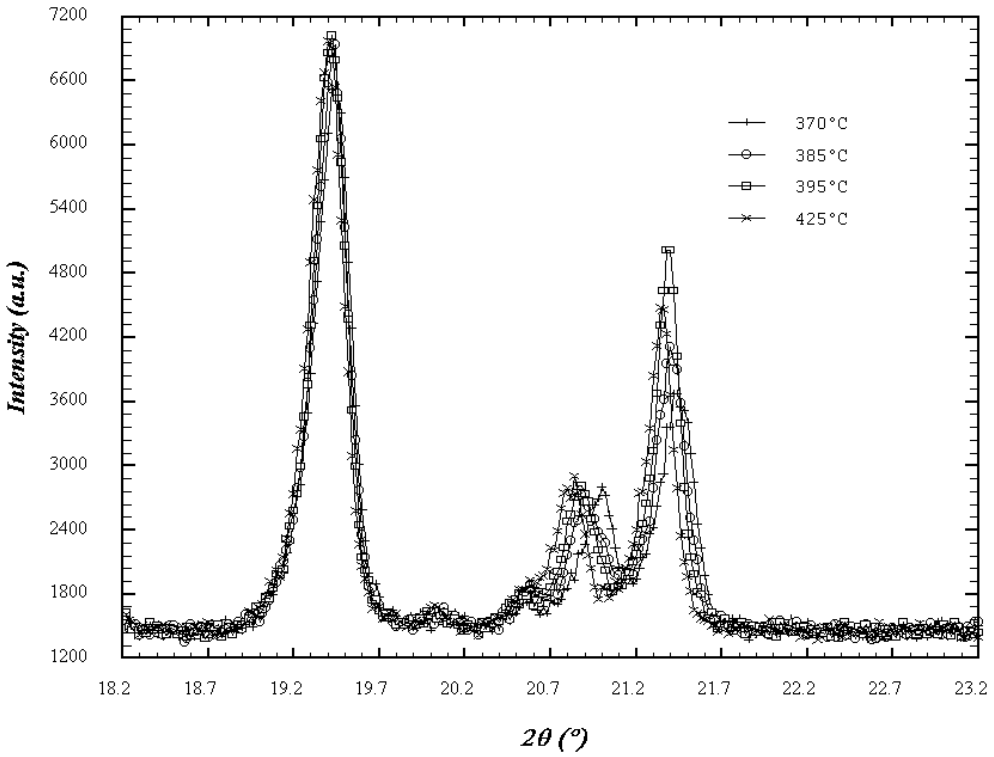

Figure 5.17: The phase transition at 384 °C: Powder diagram for $18.2° < 2\theta < 23.2°$.

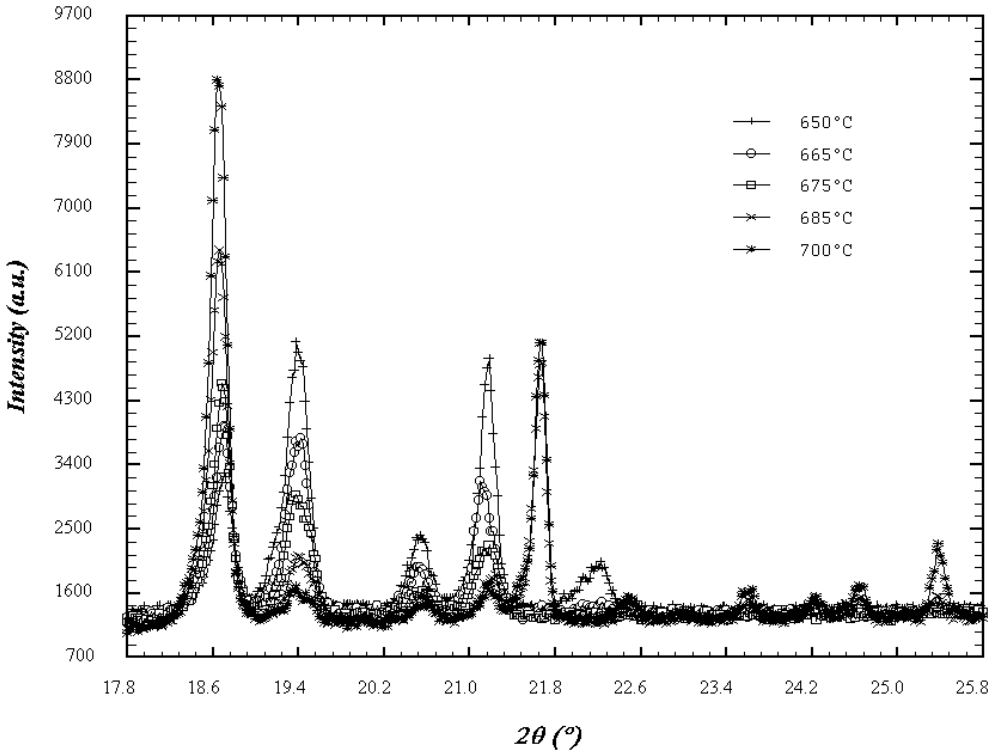

Figure 5.18: The phase transition at 668 °C: Powder diagram for $17.8° < 2\theta < 25.8°$.

5.4 Conclusion

With $Li_6CuB_4O_{10}$, we discovered the first known quaternary compound in the Li - Cu - B - O system. It crystallizes at room temperature in the space group $P\bar{1}$, with the cell parameters $a = 4.858\,(1)$ Å, $b = 9.288\,(2)$ Å, $c = 14.019\,(3)$ Å, $\alpha = 104.36\,(2)\,^\circ$, $\beta = 95.98\,(3)\,^\circ$ and $\gamma = 94.93\,(3)\,^\circ$ (Unit cell volume $V = 605.3\,(5)$ Å^3, $Z = 3$). Its structure consists of CuO_4 distorted squares, surrounded by two B_2O_5 groups and two LiO_4 tetrahedra.
Since the shortest distance between the Cu^{2+} ions ($S = \frac{1}{2}$) is $a = 4.858\,(1)$ Å, the magnetic interactions in the compound are very weak. Measurements of the magnetic susceptibility are planned, in order to determine the properties of $Li_6CuB_4O_{10}$.
DSC measurements combined with high temperature powder X-ray diffraction experiments showed that, from room temperature up to the melting point at 850 °C, $Li_6CuB_4O_{10}$ undergoes three structural phase transitions, two reversible at 345 °C and 384 °C, and one possibly irreversible at 668 °C. Since two thirds of the reflections at room temperature are much weaker than the others, one of these phase transitions might well lead to a structure with an unit cell volume V' equal to one third of the one at room temperature. Our future high temperature single crystal X-ray diffraction measurements will allow us to characterize in details the phase transitions.

Chapter 6

Conclusion

We discovered a second order structural phase transition at $T_s = 395\,K$ in the 2D spin gap system $SrCu_2(BO_3)_2$, from the low temperature space group $I\bar{4}2m$ to the high temperature space group $I4/mcm$. Measurements of the magnetic susceptibility around T_s combined with the investigation of the structural changes upon the phase transition evidenced very weak magnetic interactions between the $Cu_2(BO_3)_2$ - layers, limiting the two-dimensional character of the material.
The substitution of the Sr atoms by Ba or Ca atoms showed very few impacts on the structure and properties of $SrCu_2(BO_3)_2$. Mostly, the influence of the substitution is seen in the change in the c parameter and the disappearence of the plateaux in the magnetization curves. For a better understanding of the system, measurements of the magnetic susceptibility of $Sr_{1-x}M_xCu_2(BO_3)_2$ (M = Ba, Ca) around T_s should be performed on single phase powder samples.

We observed at room temperature the presence of superstructure reflections in the diffraction pattern of the spin gap system $BaCuSi_2O_6$, which was previously described in the tetragonal space groups $I\bar{4}m2$ and $I4/mmm$. These superstructure reflections allowed us to describe the structure of $BaCuSi_2O_6$ more accurately in the space group $I4_1/acd$, with a unit cell four times bigger than the previous one.
However, a neutron diffraction experiment would be necessary, since the simulated ratio between the intensities of the superstructure and main reflections would be significantly larger than for an X-ray diffraction measurement. Our structural model deviates from the early one mainly by the rotation of the oxygen atoms around the 4-fold rotation axis, which explains the weakness of the intensities of the superstructure reflections.
The results from Raman spectroscopy experiments, which were so far interpreted with the models of the average structure, should then be reviewed taking properly into account the superstructure and the corresponding distortions.
At 610 K, $BaCuSi_2O_6$ undergoes a structural phase transition from the low temperature space group $I4_1/acd$ to the high temperature space group $I4/mmm$, with a unit cell volume divided by four. In fact, the structural model in the high temperature phase

is the same as the centrosymmetric model $I4/mmm$ previously proposed for the room temperature structure.

$Li_6CuB_4O_{10}$ crystallizes at room temperature in the space group $P\bar{1}$. Its structure consists of CuO_4 distorted squares, surrounded by two B_2O_5 groups and two LiO_4 tetrahedra.
The compound is expected to show very weak magnetic interactions between the Cu^{2+} ions. Measurements of the magnetic susceptibility are planned, in order to determine the properties of $Li_6CuB_4O_{10}$.
$Li_6CuB_4O_{10}$ undergoes three structural phase transitions, two reversible at 345 °C and 384 °C, and one possibly irreversible at 668 °C. Our future high temperature single crystal X-ray diffraction measurements will allow us to characterize in detail the phase transitions.

Bibliography

[1] Z. Hiroi, M. Azuma, M. Takano, and Y. Bando. "A New Homologous Series $Sr_{n-1}Cu_{n+1}O_{2n}$ Found in the SrO - CuO System Treated under High Pressure". *J. Solid State Chem.*, **95**: 230 – 238, 1991.

[2] Th. Hahn, editor. *International Tables for Crystallography*, volume A, "Space-group symmetry". Kluwer Academic Publishers, fourth, revised edition, 1995.

[3] C. L. Teske and Hk. Müller-Buschbaum. "Zur Kenntnis von Ca_2CuO_3 und $SrCuO_2$". *Zeitschrift für Anorganische und Allgemeine Chemie*, **379**: 234 – 241, 1970.

[4] M. Azuma, Z. Hiroi, M. Takamo, K. Ishida, and Y. Kitaoka. "Observation of a Spin Gap in $SrCu_2O_3$ Comprising Spin-$\frac{1}{2}$ Quasi-1D Two-Leg Ladders". *Phys. Rev. Lett.*, **73** (25): 3463 – 3466, 1994.

[5] K. Sparta, G. Roth, A. Löffert, C. Gross, and W. Aßmus. "Temperature Dependence of the Crystal Structure of $SrCu_2O_3$". In preparation.

[6] T. M. Rice, S. Gopalan, and M. Sigrist. "Superconductivity, Spin Gaps and Luttinger Liquids in a Class of Cuprates". *Europhys. Lett.*, **23** (6): 445 – 449, 1993.

[7] M. Hase, I. Terasaki, and K. Uchinokura. "Observation of the Spin-Peierls Transition in Linear Cu^{2+} (Spin - $\frac{1}{2}$) Chains in an Inorganic Compound $CuGeO_3$". *Phys. Rev. Lett.*, **70** (23): 3651 – 3654, 1993.

[8] J. W. Bray, H. R. Hart Jr., L. V. Interrante, I. S. Jacobs, J. S. Kasper, G. D. Watkins, and S. H. Wee. "Observation of a Spin-Peierls Transition in a Heisenberg Antiferromagnetic Linear-Chain System". *Phys. Rev. Lett.*, **35** (11): 744 – 747, 1975.

[9] S. Huizinga, J. Kommandeur, G. A. Sawatzky, B. T. Thole, K. Kopinga, W. J. M. de Jonge, and J. Roos. "Spin-Peierls Transition in N-methyl-N-ethyl-morpholinium-ditetracyanoquinodimethanide [MEM-$(TCNQ)_2$]". *Phys. Rev. B*, **19** (9): 4723 – 4732, 1979.

[10] J. A. Northby, H. A. Groenendijk, L. J. de Jongh, J. C. Bonner, I. S. Jacobs, and L. V. Interrante. "Field-dependent Differential Susceptibility Studies on Tetrathiafulvalene-$AuS_4C_4(CF_3)_4$: Universal Aspects of the Spin-Peierls Phase Diagram". *Phys. Rev. B*, **25** (5): 3215 – 3225, 1982.

[11] M. Braden, G. Wilkendorf, J. Lorenzana, M. Aïn, G. J. McIntyre, M. Behruzi, G. Heger, G. Dhalenne, and A. Revcolevschi. "Structural Analysis of $CuGeO_3$: Relation between Nuclear Structure and Magnetic Interaction". *Phys. Rev. B*, **54** (2): 1105 – 1116, 1996.

[12] A. Carpy and J. Galy. "Affinement de la Structure Cristalline du Bronze $NaV_2O_5\alpha$' ". *Acta Cryst.*, B **31**(5): 1481 – 1482, 1975.

[13] H. Smolinski, C. Gros, W. Weber, U. Peuchert, G. Roth, M. Weiden, and C. Geibel. "NaV_2O_5 as a Quarter-Filled Ladder Compound". *Phys. Rev. Lett.*, **80** (23): 5164 – 5167, 1998.

[14] M. Isobe and Y. Ueda. "Magnetic Susceptibility of Quasi-One-Dimensional Compound α'-NaV_2O_5 – Possible Spin-Peierls Compound with High Critical Temperature of 34 K". *J. Phys. Soc. Jpn.*, **65** (5): 1178 – 1181, 1996.

[15] Y. Fujii, H. Nakao, T. Yosihama, M. Nishi, K. Nakajima, K. Kakurai, M. Isobe, Y. Ueda, and H. Sawa. "New Inorganic Spin-Peierls Compound NaV_2O_5 Evidenced by X-ray and Neutron Scattering". *J. Phys. Soc. Jpn.*, **66** (2): 326 – 329, 1997.

[16] T. Yosihama, M. Nishi, K. Nakajima, K. Kakurai, N. Takesue, Y. Fujii, M. Isobe, C. Kagami, and Y. Ueda. "Magnetic Excitations in Spin-Peierls Compound NaV_2O_5". *Physica B*, **241 - 243**: 543 – 545, 1997.

[17] M. Köppen, D. Pankert, R. Hauptmann, M. Lang, M. Weiden, C. Geibel, and F. Steglich. "Interference of a First-Order Transition with the Formation of a Spin-Peierls State in α'-NaV_2O_5". *Phys. Rev. B*, **57** (14): 8466 – 8471, 1998.

[18] J. Lüdecke, A. Jobst, S. van Smaalen, E. Morré, C. Geibel, and H.-G. Krane. "Acentric Low-Temperature Superstructure of NaV_2O_5". *Phys. Rev. Lett.*, **82** (18): 3633 – 3636, 1999.

[19] R. W. Smith and D. A. Kezler. "Synthesis, Structure, and Properties of the Orthoborate $SrCu_2(BO_3)_2$". *J. Solid State Chem.*, **93**: 430 – 435, 1991.

[20] H. Kageyama, K. Yoshimura, R. Stern, N. V. Mushnikov, K. Onizuka, M. Kato, K. Kosuge, C. P. Slichter, T. Goto, and Y. Ueda. "Exact Dimer Ground State and Quantized Magnetization Plateaus in the Two-Dimensional Spin System $SrCu_2(BO_3)_2$". *Phys. Rev. B*, **82** (15): 3168 – 3171, 1999.

[21] L. W. Finger, R. M. Hazen, and R. J. Hemley. "$BaCuSi_2O_6$: A New Cyclosilicate with Four-Membered Tetrahedral Rings". *Am. Mineral.*, **74**: 952 – 955, 1989.

[22] Y. Sasago, K. Uchinokura, A. Zheludev, and G. Shirane. "Temperature-Dependent Spin Gap and Singlet Ground State in $BaCuSi_2O_6$". *Phys. Rev. B*, **55** (13): 8357 – 8360, 1997.

[23] H. Kageyama, K. Onizuka, T. Yamauchi, and Y. Ueda. "Crystal Growth of the Two-Dimensional Spin Gap System $SrCu_2(BO_3)_2$". *J. Cryst. Growth*, **206**: 65 – 67, 1999.

[24] J. Janczak and R. Kubiak. "Structure of the Cyclic Barium Copper Silicate $Ba_2Cu_2[Si_4O_{12}]$ at 300 K". *Acta Cryst.*, C **48**(1): 8 – 10, 1992.

[25] E. M. Levin, C. R. Robbins, and H. F. McMurdie. *Phase Diagrams for Ceramists*. The American Ceramic Society, Inc., 1964.

[26] http://www.stoe.com/.

[27] STOE & Cie GmbH, Hilperstr. 10, D-64295 Darmstadt. *STOE IPDS – Software Manual*, December 1997. Version 2.87.

[28] STOE & Cie. X-SHAPE and X-RED: Programs for the optimization of the crystal shape (w.r.t. the merging R-value) and numerical absorption correction, 1996.

[29] Carvajal J. Rodriguez ˙Recent developments of the program fullprof. *CPD Newsletter*, **26**: 12 – 19, 2001.

[30] G. M. Sheldrick, Institüt für Anorganische Chemie der Universität, Tammanstr. 4, D-3400 Göttingen, Germany. *Programs for Crystal Structure Analysis*, 1998. Release 97-2.

[31] M. Meven. *Entwicklung eines hochauflösenden Röntgen-Einkristalldiffraktometers und Strukturuntersuchungen an $La_{2-x}Sr_xCuO_4$ - Einkristallen*. PhD thesis, Institut für Kristallographie der RWTH-Aachen, 2000.

[32] V. Petříček and M. Dušek. *The Crystallographic Computing System JANA2000*. Institute of Physics, Praha, Czech Republic, 2000.

[33] B. S. Shastry and B. Sutherland. *Physica B*, **108**: 1069, 1981.

[34] S. Miyahara and K. Ueda. "Exact Dimer Ground State of the Two Dimensional Heisenberg Spin System $SrCu_2(BO_3)_2$". *Phys. Rev. B*, **82** (18): 3701 – 3704, 1999.

[35] H. Kageyama, K. Onizuka, Y. Ueda, S. Shane, H. Mitamura, T. Goto, K. Yoshimura, and K. Kosuge. "Ba - and Ca - Substitution Effect on the Spin

Gap in $SrCu_2(BO_3)_2$ with the exact dimer ground state". In G. Kido, editor, *"Proceedings of 4th International Symposium on Advanced Physical Fields"*, pages 235 – 237, 1999.

[36] H. Kageyama, K. Onizuka, Y. Ueda, N. V. Mushnikov, T. Goto, K. Yoshimura, and K. Kosuge. "Magnetic Anisotropy of $SrCu_2(BO_3)_2$ with a Two-Dimensional Orthogonal Dimer Lattice". *J. Phys. Soc. Jpn.*, **67** (12): 4304 – 4305, 1998.

[37] K. Sparta, G. J. Redhammer, P. Roussel, G. Heger, G. Roth, P. Lemmens, A. Ionescu, M. Grove, G. Güntherodt, F. Hüning, H. Lueken, H. Kageyama, K. Onizuka, and Y. Ueda. "Structural Phase Transition in the 2D Spin Dimer Compound $SrCu_2(BO_3)_2$". *Eur. Phys. J. B*, **19**: 507 – 516, 2001.

[38] H. Kageyama, K. Onizuka, T. Yamauchi, Y. Ueda, S. Hane, H. Mitamura, T. Goto, K. Yoshimura, and K. Kosuge. "Anomalous Magnetizations in Single Crystalline $SrCu_2(BO_3)_2$". *J. Phys. Soc. Jpn.*, **68** (6): 1821 – 1823, 1999.

[39] S. Miyahara and K. Ueda. "Superstructures at Magnetization Plateaus in $SrCu_2(BO_3)_2$". *Phys. Rev. B*, **61** (5): 3417 – 3424, 2000.

[40] E. Müller-Hartmann and R. Singh. "Exact Demonstration of Magnetization Plateaus and First-Order Dimer-Neel Phase Transitions in a Modified Shastry-Sutherland Model for $SrCu_2(BO_3)_2$". *Phys. Rev. Lett.*, **84**(8): 1808 – 1811, 2000.

[41] S. Miyahara and K. Ueda. "Magnetization Plateau in the Frustrated Spin Ladder". *Physica B*, **281 & 282** : 659 – 660, 2000.

[42] S. Miyahara and K. Ueda. "The Magnetization Plateaus of $SrCu_2(BO_3)_2$". *Physica B*, **281 & 282** : 661 – 662, 2000.

[43] R. M. Wießner, A. Fledderjohann, K.-H. Mütter, and M. Karbach. "Spontaneous Magnetization in Spin-Ladder Systems with Competing Interactions". *Phys. Rev. B*, **60** (9): 6545 – 6551, 1999.

[44] K. Kodama, M. Takigawa, M. Horvatić, C. Berthier, H. Kageyama, Y. Ueda, S. Miyahara, F. Becca, and F. Mila. "Magnetic Superstructure in the Two-Dimensional Quantum Antiferromagnet $SrCu_2(BO_3)_2$". *Science*, **298** : 395 – 399, 2002.

[45] H. Kageyama, K. Onizuka, and Y. Ueda. "Doping Effect on the Spin Gap in $SrCu_2(BO_3)_2$". In *"Proceedings of Moscow International Symposium on Magnetism"*, pages 306 – 309, June 20th - 24th, 1999.

[46] R. Norrestam, S. Carlson, and A. Sjödin. "$Sr_{0.735}Ba_{0.265}Cu_2(BO_3)_2$ and $Sr_{0.661}Ba_{0.339}Cu_2(BO_3)_2$". *Acta Cryst.*, C **50**(12): 1847 – 1849, 1994.

[47] R. Norrestam, S. Carlson, M. Kritikos, and A. Sjödin. "Synthetic, Structural, and Magnetic Studies of Strontium Copper(II) Borates with the Composition $Sr_{1-x}M_xCu_2(BO_3)_2$, M = Ba or Ca". *J. Solid State Chem.*, **113**: 74 – 77, 1994.

[48] A. Altomare, M. C. Burla, M. Camalli, G. L. Cascarano, C. Giacovazzo, A. Guagliardi, A. G. G. Moliterni, G. Polidori, and R. Spagna. "*sir97*: a new tool for crystal structure determination and refinement". *J. Appl. Cryst.*, **32** (1): 115 – 119, 1999.

[49] G. Heger, W. F. Kuhs, and S. Massing. "A Versatile High-Temperature Furnace for Neutron Four-Circle Diffractometers". *Revue Phys. Appl.*, **19** : 735 – 738, 1984.

[50] S. Miyahara and K. Ueda. "Thermodynamic Properties of Three-Dimensional Orthogonal Dimer Model for $SrCu_2(BO_3)_2$". *J. Phys. Soc. Jpn.*, **69** (Suppl. B): 72 – 77, 2000.

[51] F. D. M. Haldane. "Nonlinear Field Theory of Large-Spin Heisenberg Antiferromagnets: Semiclassicaly Quantized Solitons of the One-Dimensional Easy-Axis Néel State". *Phys. Rev. Lett.*, **50** (15): 1153 – 1156, 1983.

[52] P. Lemmens. Private communication.

[53] H. Kageyama, N. V. Mushnikov, M. Yamada, T. Goto, and Y. Ueda. "Quantum Phase Transitions in the Orthogonal Dimer System $SrCu_2(BO_3)_2$", 2002. 23^{rd} International Conference on Low Temperature Physics.

[54] P. Lemmens, M. Grove, M. Fischer, and G. Güntherodt. "Multiple Singlet and Triplet States in the 2D Orthogonal-Dimer Compound $SrCu_2(BO_3)_2$". *Physica B*, **281 - 282**: 656 – 658, 2000.

[55] H. Kageyama. "New Two-Dimensional Spin Gap Material $SrCu_2(BO_3)_2$". *J. Phys. Soc. Jpn.*, **69**, Supp. B: 65 – 71, 2000.

[56] F. Liebau. *Structural Chemistry of Silicates – Structure, Bonding, and Classification.* Springer Verlag Berlin Heidelberg New York Tokyo, 1985.

[57] D. A. McKeown and M. I. Bell. "Four-Membered Silicate Rings: Vibrational Analysis of $BaCuSi_2O_6$ and Implications for Glass Structure". *Phys. Rev. B*, **56** (6): 3114 – 3121, 1997.

[58] J. Janczak and R. Kubiak. "Refinement of the Structure of Barium Copper Silicate $BaCu[Si_4O_{10}]$ at 300 K". *Acta Cryst.*, C **48**(7): 1299 – 1301, 1992.

[59] Th. Hahn. "Silikate - Struktur, Eigenschaften und Technische Nutzung". *Fakultät für Bergbau und Hüttenwesen der RWTH - Aachen, Technische Mitteilungen*, **56** (12): 501 – 509, 1963.

[60] Z. Z. Sheng and A. M. Hermann. "Superconductivity in the Rare-earth-free Tl-Ba-Cu-O System above Liquid-nitrogen Temperature". *Nature*, **332**: 55 – 58, 1988.

[61] E. Prince, G. Donnay, and R. F. Martin. "Neutron Diffraction of an Ordered Orthoclase". *Am. Mineral.*, **58** : 500 – 507, 1973.

[62] R. A. Barrio, F. L. Galeener, E. Martínez, and R. J. Elliott. "Regular Ring Dynamics in AX_2 Tetrahedral Glasses". *Phys. Rev. B*, **48** (21): 15672 – 15689, 1993.

[63] R. D. Shannon and C. T. Prewitt. "Effective Ionic Radii in Oxides and Fluorides". *Acta Cryst.*, B **25** (5): 925 – 946, 1968.

[64] R. Hoppe. "Effective Coordination Numbers (ECoN) and Mean Fictive Ionic Radii (MEFIR).". *Zeitschrift für Kristallographie*, **150**: 23 – 52, 1979.

[65] R. Blachnik, S. Koritnig, D. Steinmeier, A. Wilke, A. Feltz, H. Reuter, and E. Stieber. *Taschenbuch für Chemiker und Physiker*. Springer Verlag, 1998. Band 3, 4. Auflage.

[66] K. Sparta, G. J. Redhammer, and G. Roth. "The New Lithium Copper Borate $Li_6CuB_4O_{10}$". In preparation.

List of publications

Parts of this work were already presented in the following publications:

Papers

- *K. Sparta*, P. Roussel, G. J. Redhammer, G. Heger, G. Roth, A. Iononescu, P. Lemmens, G. Güntherodt, H. Kageyama, K. Onizuka and Y. Ueda
  "Structural Phase Transition in the 2D Spin Dimer Compound $SrCu_2(BO_3)_2$"
  Eur. Phys. J. B, **19** : 507-516, 2001

Talks

- February 21^{th}, 2000
  "$SrCu_2(BO_3)_2$: Observation of a Structural Phase Transition at High Temperature"
  DFG informal meeting, Bayreuth (Germany)

- June 20^{th}, 2000
  "Study of a Crystallographic Phase Transition in the Strontium Copper Borate $SrCu_2(BO_3)_2$"
  Institut für Kristallographie, RWTH-Aachen (Germany)

- December 12^{th}, 2000
  "Evolution en Température de la Structure de $SrCu_2(BO_3)_2$"
  Tables Rondes B, Laboratoire Léon Brillouin, Saclay (France)

- August 26^{th}, 2001
  "Structural Phase Transition in the Quasi-2D Spin Dimer System $SrCu_2(BO_3)_2$: a Substitution Study"
  ECM 20, Kraków (Poland)

- November 29^{th}, 2001 (invited talk)
  "Nouvelle Détermination de la Structure de $BaCuSi_2O_6$"
  Tables Rondes B, Laboratoire Léon Brillouin, Saclay (France)

- February 13^{th}, 2002 (invited talk)
  "Etude Structurale de Matériaux à Propriétés Magnétiques Bidimensionnelles: $SrCu_2(BO_3)_2$ et $BaCuSi_2O_6$"
  Laboratoire de Cristallographie et Modélisation des Matériaux Minéraux et Biologiques, Nancy (France)

- June 3^{rd}, 2003
  "Züchtung und Kristallstrukturanalyse des neuen Lithium-Kupfer-Borates $Li_6CuB_4O_{10}$"
  Institut für Kristallographie, RWTH-Aachen (Germany)

Posters

- August 26^{th} - 27^{th}, 2000
  "Evidence for a Structural Phase Transition in the Quasi-2D Spin Dimer System $SrCu_2(BO_3)_2$"
  K. Sparta, G. J. Redhammer, P. Roussel, G. Roth, G. Heger
  ECM 19, Nancy (France)

- November 6^{th} - 7^{th}, 2000
  "Evidence for a Structural Phase Transition in the Quasi-2D Spin Dimer System $SrCu_2(BO_3)_2$"
  K. Sparta, G. J. Redhammer, P. Roussel, G. Roth, G. Heger
  DFG meeting, Walberberg (Germany)

- March 12^{th} - 15^{th}, 2001
  "Struktureller Phasenübergang im quasi zweidimensionalen $SrCu_2(BO_3)_2$"
  K. Sparta, G. J. Redhammer, G. Roth, G. Heger
  DGK 2001, Bayreuth (Germany)

- March 26^{th}, 2001
  "Substitution Study of the 2D Spin Dimer Compound $SrCu_2(BO_3)_2$"
  K. Y. Choi, P. Lemmens, G. Güntherodt, *K. Sparta*, G. Roth, F. Hüning, H. Lueken, H. Kageyama, K. Onizuka, Y. Ueda
  65. DPG meeting, Hamburg (Germany)

- November 26^{th} - 27^{th}, 2001
  "Neue Vanadate mit niedrigdimensionalen Strukturmotiven"
  K. Sparta, G. Roth
  DFG meeting, Walberberg (Germany)

- March 6^{th} - 7^{th}, 2002
  "Raumtemperaturstruktur des Bariumkupfersilikates $BaCuSi_2O_6$"
  K. Sparta, G. Roth, G. Heger, P. Lemmens, T. Masuda, K. Ochinokura
  DGK 2002, Kiel (Germany)

- August 12^{th} - 15^{th}, 2002
  "Redetermination of the room temperature structure of $BaCuSi_2O_6$"
  K. Sparta, G. Roth, G. Heger, P. Lemmens, T. Masuda, K. Ochinokura
  XIX Congress of the IUCr, Geneva (Switzerland)

- March 10^{th} - 11^{th}, 2003
  "Einkristall-Strukturanalyse der 2-Bein-Spinleiter-Verbindung $SrCu_2O_3$ zwischen 300 K und 100 K"
  K. Sparta, A. Löffert, C. Gross, W. Aßmus, G. Roth
  DFG meeting, Walberberg (Germany)

- March 10^{th} - 11^{th}, 2003
  "$Li_6CuB_4O_{10}$: Ein neues Lithium-Kupfer-Borat mit B_2O_5-Gruppen"
  K. Sparta, G. J. Redhammer, G. Roth
  DGK 2003, Berlin (Germany)

- March 10^{th} - 11^{th}, 2003
  "Einkristall-Strukturanalyse der 2-Bein-Spinleiter-Verbindung $SrCu_2O_3$ zwischen 300 K und 100 K"
  K. Sparta, A. Löffert, C. Gross, W. Aßmus, G. Roth
  DGK 2003, Berlin (Germany)

Acknowledgements

This Ph-D thesis took place at the Institut für Kristallographie of the RWTH-Aachen, as a project of the DFG (German Research Council) research programm n° 1073 "Kollektive Quantenzustände in elektronisch eindimensionalen Übergangsmetallverbindungen".

I thank Prof. Dr. Georg Roth for the many fruitful discussions, and the assistance during the synthesis of samples and the single crystal X-ray diffraction experiments with the Stoe-IPDS diffractometers.

I thank Prof. Dr. Gernot Heger for his useful explanations about neutron diffraction experiments, and for the continuous interest he showed in the progresses of my work.

I am grateful to Prof. Dr. Claude Lecomte for his kind advices and for offering me the possibility to make my Ph-D thesis abroad.

I would like to thank Dr. Christian Scherf for the strenuous support during the measurements on the neutron four-circle diffractometer in Saclay and for his kindness. In relation to this, I thank Alain Cousson for his good advices about the data evaluation and his interest to my work. I also thank Burkhard Annighöfer for his help by experimental problems, particularly for the construction of a vanadium heating device for the four-circle diffractometer.

I thank Dr. Günther Redhammer for his help by the synthesis of $SrCu_2(BO_3)_2$ and $Li_6CuB_4O_{10}$, the powder diffraction measurements and their analysis, and for the nice mood in our common room.

I am grateful to Dr. Martin Meven and Dr. Stefan Mattauch for the high temperature experiments on the X-ray four-circle diffractometer. In relation to this, I thank Franz-Dieter Scherberich and Rolf Becker for the construction of an aluminium heating device. I also thank Dr. Pascal Roussel for the long evenings spent in the lab analysing the diffraction data.

I thank Dr. Horst Schmidt for the assistance during X-ray Laue diffraction experiments.

I thank Dr. Hiroshi Kageyama and Prof. Dr. Yutaka Ueda for the synthesis of the $SrCu_2(BO_3)_2$ samples, and Prof. Dr. Kunimitsu Uchinokura for the $BaCuSi_2O_6$ single crystals.

I am grateful to Dr. Stefan Mattauch, Egon Heidrich and Bernd Bollwerk for the infinite patience they used to solve my so many computer problems.

I thank all the coworkers of the Institut für Kristallographie for their helpfulness and friendliness that contributed to the good success of this work.

I thank the Deutsche Forschungsgemeinschaft for the 40 months of financial support.

Lebenslauf

Karine Sparta

19.11.1976	geboren in Grasse (Frankreich)
1986 - 1991	Besuch des Gymnasium Henri Nans, Aups (Frankreich)
1991 - 1994	Besuch des Gymnasium Jean Moulin, Draguignan (Frankreich)
1994	Baccalauréat série C (Abitur), Fréjus (Frankreich)
1994 - 1998	Studium der Physik Université de Nice Sophia-Antipolis, Nice (Frankreich)
1998 - 1999	DEA Physique et Chimie de la Matière et des Matériaux (Diplom) Université Henri Poincaré, Nancy (Frankreich) *Etude structurale du niobate de barium et de strontium* $Ba_{0.39}Sr_{0.61}Nb_2O_6$
1999 - 2003	Wissenschaftliche Mitarbeiterin Institut für Kristallographie der RWTH Aachen